LABORATORI NAZIONALI DI FRASCATI
SIS – Pubblicazioni

LNF-03/011 (Thesis)
11 Giugno 2003

Università degli Studi di Roma
La Sapienza
Facoltà di Ingegneria

Dottorato di Ricerca in Elettromagnetismo Applicato
e Scienze Elettrofisiche
XV Ciclo

BEAM CONTROL AND MANIPULATION WITH MICROWAVE DEVICES IN PARTICLE ACCELERATORS

Tesi di Dottorato di
David Alesini

Docente guida:
Prof. L. Palumbo

Coordinatore dottorato:
Prof. Giorgio Gerosa

Dicembre 2002

Index

Introduction

The control and the manipulation of the beam can be considered as the main “goals” in the particle accelerators research.
The correct control of the transverse and longitudinal beam sizes and position allows optimising the luminosity performance of the machine (as in colliders) or the light quality (as in synchrotrons).
In the transverse plane, the beam profile is determined by properly setting the currents in the magnets (dipole, quadrupoles, and sextupoles) while, in the longitudinal plane, by the combined effects of the accelerating field gradient, synchrotron radiation emission and dipole magnets configuration.
At high beam currents, however, the wake fields, produced by the interaction of the beam with the vacuum chamber components, interact with the beam itself causing deformation of the longitudinal bunch profile and possible longitudinal and transverse instabilities.
The study of these collective effects is very important in order to preserve the beam quality and to avoid the loss of the beam.
This is done, in general, finding a correct model of the wake fields in the accelerator and analysing the effects of this wake fields on the beam itself.
The first step is achieved by means of analytical treatments, electromagnetic (e.m.) simulations or devices measurements that allow determining the fields produced by the interaction beam-vacuum chamber components. The second one can be obtained by analytical theories or by tracking codes that can simulate the beam motion under the effect of these self-fields.
Microwave structures, installed in the ring to accelerate, deflect or, in general, to manipulate bunches, have to be, therefore, properly characterized and the “unwanted” effects have to be carefully analysed or limited by a proper e.m. design of the components.
In parallel, diagnostics devices installed in the rings allow tuning the machine parameters in order to achieve the better performances. The research of compact and non-perturbative components is, therefore, of a big importance.
The present thesis can be inserted on this context.
In the first chapter, the analytical treatment of the longitudinal beam dynamics in circular accelerators is reported and discussed. A numerical tracking code that allows studying the single-bunch and the multi-bunch collective effects is, also, described.
The second chapter is dedicated to the description of RF devices used in accelerators. It includes the description of the standing wave and travelling wave structures, and the presentation of the e.m. simulations codes and of the bench measurements techniques.
The proper research activity is illustrated in the three last chapters.
In the third one the beam dynamics in the accelerator DAΦNE with a harmonic system is analysed. DAΦNE is a double ring, high luminosity collider working at the energy of the Φ resonance (1.02 GeV in the center of mass). The study and the design

of a high harmonic RF system is mainly motivated by the demand of lifetime improvement and by the increasing of the natural Landau damping mechanism. The beam dynamics in the accelerator has been studied with analytical theories and tracking codes and the design of the device has been done with e.m. simulations codes (MAFIA and HFSS). RF measurements have been, also, made on the constructed device.

In the fourth chapter, the CTF3 RF deflectors project is illustrated. CTF3 (CLIC Test Facility) is the third facility of the project CLIC (Compact Linear Collider) at CERN. The CLIC studies focuses on high-gradient, high frequency acceleration for multi-TeV linear collider. Because conventional RF power sources based on modulators and klystrons are not available at high frequencies, CLIC was based on the novel and promising concept of Two-Beam Acceleration (TBA). The basic idea of the TBA is to properly recombine the bunch train (Drive Beam) generated by a conventional linear accelerator in order to create an high peak current beam with a time spacing between bunches considerably reduced. This bunch structure is realized by a novel technique of bunch recombination, using RF deflectors, which converts a long bunch train, with a large bunch spacing, into a sequence of short trains with a bunch spacing considerably reduced, which is used for the high frequency power production. The design of the deflectors for the Combiner Ring of CTF3 includes both the study of the beam dynamics effects in the ring than the design of the devices. The beam dynamics study has been developed by modelling the wake field in the deflectors and by writing a tracking code that allows studying the multi-passage multi-bunch effects. The design of the deflectors has been done, instead, by the simulation codes MAFIA and HFSS. Measurements results are reported and discussed.

The last chapter illustrates the study of a microwave bunch-position monitor. A large number of bunch length monitors exist either in the time domain than in the frequency domain. In particular the devices that use the microwave spectroscopy are based on the analysis of the beam characteristics in the frequency domain. By this analysis it is possible to obtain the bunch parameters in the time domain such the bunch length or the position inside the vacuum chamber. Different techniques have been proposed to couple the field radiated by the bunch in a transmission line leading the signal to the detection system. The proposed monitor is a resonant small coaxial cavity coupled to the beam pipe through four small slots. If the length of the cavity is properly chosen, the beam power spectrum lines excite resonant modes in the cavity and, probing the field by a small antenna, it is possible to characterize the beam in term of average bunch length and position. In the chapter, the analytical approach based on the Bethe's Theory is reported with the simulations results obtained by MAFIA and HFSS. Measurements made on a prototype are also discussed and compared with the theoretical results.

Chapter 1

Beam dynamics in circular accelerators

A storage ring may be considered as a complex of components that guides the particle beam inside the vacuum chamber.
The motion of a single particle is determined by the external magnetic fields created by the dipole, quadrupole and sextupoles that provide the transverse focusing of the beam, by the RF longitudinal electric field that accelerates the beam, by the synchrotron radiation emitted by the particle in the bending magnets and by the wake fields generated by the interaction between the beam and the vacuum chamber components.
The first paragraph of this chapter introduces the concepts of wake fields and coupling impedances.
The longitudinal equation of motion for a distribution of particles is derived in the second paragraph. The equation of Haissinki, describing the bunch distribution at low current, is also discussed. The single bunch effects in high intensity beam are, then, introduced and a tracking code that allows studying the single bunch dynamics is described.
The multi-bunch beam dynamics is treated in the third paragraph where the macroparticle model is illustrated. A tracking code for the multibunch dynamics study is, also, described. It allows studying the multi-bunch beam dynamics with non-uniform filling patterns including the presence of a bunch-by-bunch feedback system in the ring.
The longitudinal beam dynamics is also affected by a natural damping mechanism called Landau damping that is discussed in the fourth paragraph.
Finally, in the fifth paragraph, the beam lifetime due to the Touschek effect is presented.

1.1 Wake fields and impedances

The beam traveling inside a complicated vacuum chamber induces electromagnetic (e.m.) fields which may affect the dynamics of the beam itself.

The e.m. fields induced by the beam are called wake fields due to the fact that they are left, mainly, behind the traveling charge.
The study of the longitudinal and transverse beam dynamics requires the knowledge of these induced "self-fields" which may limit the performance of the accelerator in term of beam quality and stored current.
The e.m. fields generated by a charge q_1 traveling with a constant velocity $v=\beta c$ on a trajectory parallel to the axis of a vacuum chamber in the structure, can be derived solving the Maxwell equations satisfying proper boundary conditions [1].
The energy lost by a trailing charge q under the effect of these fields can be written in the form[1] (Fig. 1.1):

$$U_z(\underline{r},\underline{r}_1;\tau) = -\int_{structure} F_z(s,\underline{r},s_1,\underline{r}_1;t)ds \qquad \text{with } t=\frac{s_1}{v}+\tau \tag{1.1}$$

where F_z is the longitudinal force on the charge q and τ is the time distance between q_1 and q. The quantity U_z represents the energy lost ($U_z>0$) or gained ($U_z<0$) by the charge q.
The *longitudinal wake function* $w_z(\underline{r},\underline{r}_1,\tau)$ is defined as the energy lost by the trailing charge per unit of both charges q_1 and q:

$$w_z(\underline{r},\underline{r}_1;\tau) = \frac{U_z(\underline{r},\underline{r}_1;\tau)}{qq_1} \tag{1.2}$$

According to the definition (1.2) it is possible to calculate the wake function produced by a bunch distribution by the convolution:

$$W_z(\underline{r},\underline{r}_1;\tau) = \frac{1}{q_1}\int_{-\infty}^{\infty} i_1(\tau')w_z(\underline{r},\underline{r}_1;\tau-\tau')d\tau' \tag{1.3}$$

where $i_1(\tau)$ is the bunch distribution of total charge q_1. Usually W_z is called *longitudinal wake potential*.
The vacuum chamber is formed by a smooth beam pipe with regular cross section (circular, rectangular or elliptic) and by various devices such as RF cavities, kickers and the diagnostic components. The exact solution of the Maxwell equations for the whole structure is impossible to obtain even with the most sophisticated computer codes [2] and, usually, one analyses a component at a time and sum-up the various effects even if this procedure may lead to inexact estimates at high frequencies where interference effects are not negligible.

[1] The charges are considered ultrarelativistic $\beta\cong 1$;

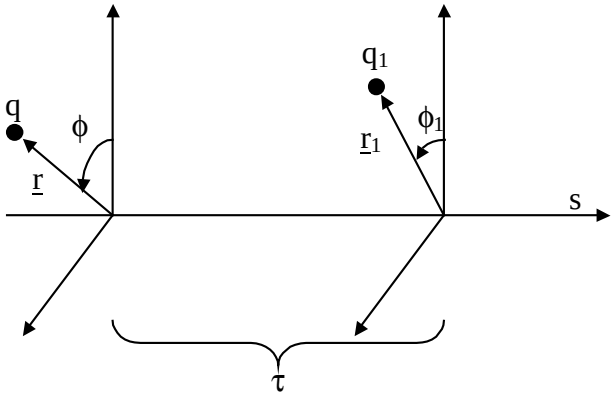

Fig. 1.1: coordinates system used to describe the wake fields.

In the frequency domain the spectrum of the longitudinal wake function is called *longitudinal coupling impedance*:

$$Z_z(\underline{r},\underline{r}_1;\omega)=\int_{-\infty}^{\infty} w_z(\underline{r},\underline{r}_1;\tau)e^{-j\omega\tau}d\tau \tag{1.4}$$

It is measured in Ohm and, historically, it has been introduced in the early studies of the instabilities arising in the ISR at CERN [3].
Vice versa the wake function is given by:

$$w_z(\underline{r},\underline{r}_1;\tau)=\frac{1}{2\pi}\int_{-\infty}^{\infty} Z_z(\underline{r},\underline{r}_1;\omega)e^{j\omega\tau}d\tau \tag{1.5}$$

Similarly the trailing charge q experiences a Lorentz force which has transverse components. The transverse momentum kick is given by:

$$\underline{U}_t(\underline{r},r_1;\tau)=\int_{structure}\underline{F}_t(s,\underline{r},s_1,\underline{r}_1;t)ds \tag{1.6}$$

The *transverse wake function* is defined as:

$$\underline{w}_t(\underline{r},\underline{r}_1;\tau)=\frac{\underline{U}_t(\underline{r},\underline{r}_1;\tau)}{qq_1} \tag{1.7}$$

and the *transverse coupling impedance* is defined as:

$$\underline{Z}_t(\underline{r},\underline{r}_1;\omega)=j\int_{-\infty}^{\infty}\underline{w}_t(\underline{r},\underline{r}_1;\tau)e^{-j\omega\tau}d\tau \tag{1.8}$$

Using simple relations given by the Maxwell's equations it is possible to derive the following equations between the longitudinal and the transverse wakes and impedances:

$$-\frac{1}{v}\frac{\partial}{\partial\tau}\underline{w}_t(\underline{r},\underline{r}_1;\tau)=\nabla_{t,\underline{r}}w_z(\underline{r},\underline{r}_1;\tau) \tag{1.9a}$$

$$\underline{Z}_t(\underline{r},\underline{r}_1;\omega)=\frac{c}{\omega}\nabla_{t,\underline{r}}Z_z(\underline{r},\underline{r}_1;\omega) \tag{1.9b}$$

these relations are often referred to as the *Panofsky-Wenzel theorem* [4].

1.1.1 Cylindrically symmetric structures

So far the case of general boundaries has been considered without restrictions on the transverse position of both charges.
Assuming a structure with cylindrical symmetry the density charge q_1 can be represented as follows [5]:

$$\rho_1=\frac{q_1}{\pi}\frac{\delta(r-r_1)}{r_1}\delta(s-s_1)\sum_{m=0}^{\infty}\frac{1}{1+\delta_{m0}}\cos(m\phi) \tag{1.10}$$

where ϕ_1 of Fig. 1.1 has been supposed equal to 0.
According to the above expression the charge q_1 can be thought as a superposition of charged rings with angular dependence $\cos(m\phi)$. In the presence of cylindrical symmetries the e.m. field created by the distribution (1.10) can be derived as the sum of multipole terms showing the same angular dependence. The resulting wake function will show the following form:

$$w_z(\underline{r},\underline{r}_1;\tau)=\sum_{m=0}^{\infty}w_{z,m}(\underline{r},\underline{r}_1;\tau) \tag{1.11}$$

In the case of ultra-relativistic charges ($\beta\cong1$) it can be shown that the wake function has the following radial dependence [6-8]:

$$w_z(\underline{r},\underline{r}_1;\tau)=\sum_{m=0}^{\infty}r^m r_1^m w_{z,m}(\tau)\cos(m\phi) \tag{1.12}$$

The impedance is then given by:

$$Z_z(\underline{r},\underline{r}_1;\omega)=\sum_{m=0}^{\infty}r^m r_1^m Z_{z,m}(\omega)\cos(m\phi) \tag{1.13}$$

The monopole term (m=0) does not depend on the radial position of both charges and for charges traveling on the axis of the structures is the only non-vanishing term in the summations (1.12)-(1.13).
Similarly the transverse wake can be written as a superposition of multipoles terms of the form [9]:

$$\frac{\partial}{\partial \tau}\underline{w}_{t,m} = -cmr^{m-1}r_1^m w_{z,m}(\tau)\left[\cos(m\phi)\hat{r} - \sin(m\phi)\hat{\phi}\right] \overset{\text{for the dipole term}}{\Rightarrow} \frac{\partial}{\partial \tau}\underline{w}_{t,1} = -cw_{z,1}(\tau)\underline{r}_1 \tag{1.14}$$

and the transverse impedance as a superposition of the terms:

$$\underline{Z}_{t,m} = \frac{c}{\omega}mr^{m-1}r_1^m Z_{z,m}(\omega)\left[\cos(m\phi)\hat{r} - \sin(m\phi)\hat{\phi}\right] \overset{\text{for the dipole term}}{\Rightarrow} \underline{Z}_{t,1} = \frac{c}{\omega}Z_{z,1}(\omega)\underline{r}_1 \tag{1.15}$$

The transverse dipole term m=1 is proportional to the transverse displacement of the leading charge while it does not depend on the transverse position of the trailing one. It is, also, the non-vanishing term if r=0.

1.1.2 Short range wake fields: broad band resonator model

The *short range wake fields* can be defined as the wake fields acting on a distance equal to the bunch length (see par. 1.2.1) while the *long range wake fields* as those acting on a distance larger than the bunch length.
To study the longitudinal single bunch dynamics, it is often possible to consider the effect of the short range wake fields only, neglecting the multi-turn or the coupled bunch interactions generated by the long range wake fields. This implies that, in the frequency domain, the single bunch cannot resolve the details of the sharp resonances and it rather experiences an average effect.
The impedance of an accelerator (that is usually a very complicated function of frequency with many sharp peaks) can be replaced, in this case, by some “broad band model impedance”.
These models are usually characterized by a small number of parameters and they allow analytical evaluation of the stability limits or growth rates of single bunch instabilities.
The first introduced *broad band resonator model* [10] considers an average impedance of the form:

$$Z_z(\omega) = \frac{R_s}{1 + jQ\left(\frac{\omega}{\omega_r} - \frac{\omega_r}{\omega}\right)} \tag{1.16}$$

where the radial dependence has been neglected[2].
Only three parameters, the shunt impedance R_s, the angular resonant frequency ω_r and the quality factor Q, are necessary to describe the impedance frequency behaviour. For long bunches R_s is estimated by averaging the resistive part of the parasitic resonances (see par. 1.1.3), the quality factor is usually taken equal to 1 while the resonant frequency is taken as the cut of frequency of the first monopolar propagating mode of the beam pipe.
These choices are somewhat arbitrary and are satisfactory only for the case of long bunches, when the whole bunch spectrum lies within the beam pipe cut-off.
A *new broad band impedance model* was proposed by S. Heifets [11] as the further development of K. Bane's approach used in the analysis of the SLC damping ring impedance [12,13]. The longitudinal impedance is described phenomenologically by the expansion:

$$Z_z(\omega) = j\omega L(\sigma_z) + R(\sigma_z) + [1 + j\,\mathrm{sgn}(\omega)]\sqrt{|\omega|}B(\sigma_z) + \frac{1 - j\,\mathrm{sgn}(\omega)}{\sqrt{\omega}} Z_c(\sigma_z) \tag{1.17}$$

The first term of the expansion represents a low frequency inductive impedance. This impedance is typical for tapered sections, shielded bellows, vacuum ports and small discontinuities such as slots, shallow cavities in flanges and so on.
The second resistive contribution is given essentially by the cavities in the ring [1].
The third term has a structure of the resistive-wall impedance [1] while the fourth term has the same dependence on ω as the impedance of a cavity with attached tubes at high frequencies [1].
The parameters L, R, B, Z_c of the broad band model can be extracted by computer code results by fitting the numerical wake potential to the above analytical expressions [14].

1.1.3 Long range wake fields: resonant cavities

Cross-section variations in an accelerator vacuum chamber can create resonant cavities. Part of the field excited in the cavities is trapped reflecting back and forth and generating the resonant modes.
The field excited in a cavity by the bunch is the typical example of long range wake field because it can interact with the other bunches of the beam or with the same bunch in different turns.
The classical example of RF cavity is that used to accelerate the beam (see par. 1.3.3 and 2.1). In this case the fundamental mode (usually the first monopolar mode) is used to supply energy to the beam by an external RF generator coupled to the cavity. All

[2] The only monopolar term is considered.

the others modes called *Higher Order Modes* (HOM) are parasitic modes and can cause multibunch instabilities (par. 1.3) and additional parasitic power loss.

Monopole modes

As shown in par. 2.1 the longitudinal coupling impedance of a monopole mode can be approssimated in the form:

$$Z_z(\omega) = \frac{R_s}{1 + jQ\left(\frac{\omega}{\omega_r} - \frac{\omega_r}{\omega}\right)} = \frac{R_s}{1 + jQ\delta} \tag{1.18}$$

The parameters Q and ω_r are the quality factor and the angular resonant frequency of the resonant mode while the parameter R_s is called *shunt impedance*. All three parameters depend on the cavity shape and material.
The wake field corresponding to the impedance (1.18) is given by:

$$w_{z,0}(r, r_1; \tau) = \frac{\omega_r R_s}{Q} e^{-\frac{\omega_r}{2Q}\tau}\left[\cos(\omega'_r \tau) - \frac{\omega_r}{2Q\omega'_r}\cos(\omega'_r \tau)\right] H(\tau) \qquad \text{with } \omega'_r = \omega_r\sqrt{1 - \frac{1}{4Q^2}} \tag{1.19}$$

where $H(\tau)$ is the Heaviside function.
From the above formula it follows that the interaction between the charge and the resonant mode can be schematized by an *RLC* parallel circuit driven by a point-charge current $i_b(\tau)=q_1\delta(\tau)$ representing the bunch, as shown in Fig. 1.2. The longitudinal wake field $w_z(\tau)$ is simply given by $V(\tau)/q_1$.

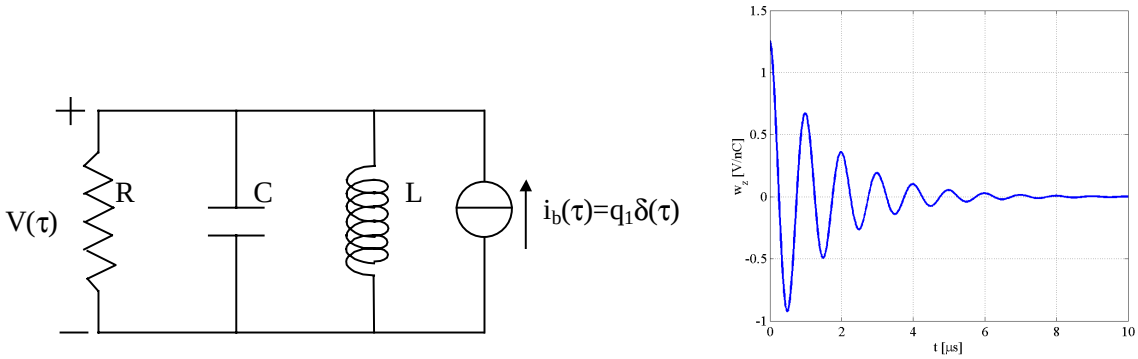

Fig. 1.2: (a) *RLC* circuit that model the interaction between the resonant impedance and the beam; (b) wake function of a resonator with Q=5000, R_s=1 KΩ, f_r=1GHz.

In the figure R_s is the shunt impedance of the resonant mode and L, C are related to the resonant frequency and quality factor trough the well know relations:

$$\omega_r = \sqrt{\frac{1}{LC}}$$

$$Q = \omega_r RC \tag{1.20}$$

Referring to the same circuit, when the bunch interacts with the mode, it losses instantaneously, an amount of energy equal to:

$$U = \frac{q_1^2}{2C} = \frac{\omega_r R_s q_1^2}{2Q} = \frac{w_z(\tau \to 0^+)}{2} q_1^2 \tag{1.21}$$

the last equality is known as the *fundamental theorem of the beam loading* [15]: it states that, if β=1 the energy losses by the particle q_1 (normalized to q_1) is exactly one half the value of the wake function calculated with $\tau \to 0^+$.

Dipolar modes

The longitudinal coupling impedance of a dipolar mode is given by (par. 2.1):

$$Z_{z1}(\omega) = \frac{R_{s1}}{1 + jQ_1\left(\frac{\omega}{\omega_{r1}} - \frac{\omega_{r1}}{\omega}\right)} \frac{rr_1}{b^2} \cos(\phi) \tag{1.22}$$

where the parameters R_{s1}, Q_1, ω_{r1} are, now, referred to the dipolar mode and the distance b is introduced in order to maintain R_{s1} expressed in Ohm.
The transverse coupling impedance corresponding to the same resonant mode is given by:

$$\underline{Z}_t(\omega) = \frac{R_t}{1 + jQ_1\left(\frac{\omega}{\omega_{r1}} - \frac{\omega_{r1}}{\omega}\right)} \underline{r}_1 = \frac{\frac{R_{s1}}{b^2}\frac{c}{\omega}}{1 + jQ_1\left(\frac{\omega}{\omega_{r1}} - \frac{\omega_{r1}}{\omega}\right)} \underline{r}_1 \tag{1.23}$$

The longitudinal and transverse wake field, generated by the interaction with this dipole mode, is given by:

$$w_{z,1}(r, r_1; \tau) = \frac{\omega_{r1} R_{s1}}{Q_1} \frac{rr_1}{b^2} e^{-\frac{\omega_{r1}}{2Q_1}\tau} \left[\cos(\omega'_{r1}\tau) - \frac{\omega_r}{2Q_1\omega'_r}\sin(\omega'_{r1}\tau)\right] H(\tau) \qquad \text{with } \omega'_{r1} = \omega_{r1}\sqrt{1 - \frac{1}{4Q_1^2}} \tag{1.24a}$$

$$\underline{w}_t(r, r_1; \tau) = -\frac{cR_{s1}\omega_r}{\omega'_r\, b^2 Q_1} e^{-\frac{\omega_{r1}}{2Q_1}\tau} \sin(\omega'_{r1}\,\tau) H(\tau) \underline{r}_1$$

(1.24b)

1.2 Single bunch longitudinal beam dynamics

A generic particle of the beam, in a circular accelerator, follows a curvilinear trajectory inside the beam pipe losing energy because of the radiation emitted in the bending magnets (*synchrotron radiation*) and because of the interaction with the devices in the accelerator. This loss of energy is compensated by the RF accelerating field in the cavities installed in the ring.
The *synchronous particle* is defined as the particle that enters in the cavity when the oscillating field has an amplitude that compensates exactly the loss of energy in the ring.
To describe the longitudinal beam dynamics it is convenient to introduce the following quantities:

- L_0: length of the circumference followed by the synchronous particle;
- T_0: revolution period of the synchronous particle;
- E_0: nominal energy of the synchronous particle at the exit of the RF cavity;
- z: longitudinal displacement of a generic particle with respect to the synchronous one at the exit of the RF cavity (if $z>0$ the particle is ahead of the synchronous one);
- Δz: variation of the longitudinal position of a particle in a revolution period ($z(t)$-$z(t$-$T_0)$);
- ε: energy deviation of a generic particle respect to the synchronous one;
- $\Delta\varepsilon$: energy variation in one revolution period ($\varepsilon(t)$-$\varepsilon(t$-$T_0)$);
- α_c: *momentum compaction*: it is the variation of the circumference length with respect to the particle with the nominal energy. It is determined from the fact that the radius of curvature in bending magnets depends on the energy of the particle itself:

$$\alpha_c = \frac{(L_\varepsilon - L_0)/L_0}{\varepsilon / E_0}$$

(1.25)

where L_ε is the circumference length of an off-energy particle.
By the previous definitions it is possible to write the following equation:

$$\Delta z = L_0 - L_\varepsilon = -L_0 \alpha_c \frac{\varepsilon}{E_0}$$

(1.26)

The energy radiated by an off-energy particle can be calculated for small energy deviations as [16,17]:

$$U(\varepsilon) = U_0 + D\varepsilon \tag{1.27}$$

where U_0 is the average radiated energy of a synchronous particle and D (>0) is called *damping factor*.

The electromagnetic radiation occurs in quanta of discrete energy and each time a quantum is emitted the energy of electrons makes a small discontinuous jump that disturbs the trajectory of the particle. This emissions may be considered instantaneous and following a purely random Poisson process [18]. The cumulative effect of many such disturbances in the trajectories introduces a kind of "noise" into the various oscillation modes causing their amplitude to growth until the quantum excitation is, on average, balanced by the damping of the oscillation due to the damping factor D ($\tau_\varepsilon = D/2T_0$ is called *damping time*).

The equation that links the change in energy with the longitudinal position of the particle is then:

$$\Delta\varepsilon = e(V(z) + V'(z)) - [U_0 + D\varepsilon + R(T_0)] \tag{1.28}$$

where $V(z)$ is the accelerating voltage in the RF cavity seen by a particle occupying the position z with respect to the synchronous one, $V'(z)$ is the accelerating voltage due to the wake fields[3] and $R(T_0)$ is the difference between the radiated energy in one turn and its average value.

Dividing the equation by T_0 and substituting the finite differences with a time derivative[4], one obtains the equations that describes the longitudinal dynamics[5]:

$$\begin{cases} \dfrac{dz}{dt} = -c\alpha_c \dfrac{\varepsilon}{E_0} \\ \dfrac{d\varepsilon}{dt} = \dfrac{e(V(z) + V'(z)) - [U_0 + D\varepsilon + R(T_0)]}{T_0} \end{cases} \tag{1.29}$$

The equation of motion becomes:

$$\frac{d^2 z}{dt^2} + \frac{D}{T_0}\frac{dz}{dt} + \frac{c\alpha_c}{E_0 T_0} e[V(z) + V'(z)] - \frac{c\alpha_c}{E_0 T_0}[U_0 + R(T_0)] = 0 \tag{1.30}$$

[3] The hypothesis is that the energy exchange between the particle and the RF cavity (or wake field) are concentrated at the exit of the RF cavity. This is, in general, acceptable since the revolution time is much smaller than the characteristic times of the analyzed phenomena.

[4] This approximation can be considered correct for the same reason discussed in the previous note.

[5] The particle is considered ultra-relativistic.

The motion of a single particle in the phase plane (z,ε) is characterized by two opposite effects: the damping due to the coefficient D that forces the particle to collapse in the center (0,0) and the quantum excitation given by the term $R(T_0)$ that gives the opposite effect.
The equation of motion can be also written using the Hamiltonian formalism [19]. Defining the potential well of the particle as:

$$\varphi(z) = \frac{\alpha_c}{E_0 L_0}\int_0^z \{e[V(z')+V'(z')]-U_0\}dz' \tag{1.31}$$

and the Hamiltonian as:

$$H(z,\varepsilon) = \frac{\alpha_c}{2E_0}\varepsilon^2 + \frac{E_0}{\alpha_c}\varphi(z) \tag{1.32}$$

the equations of motion (1.29) become:

$$\begin{cases} \dfrac{dz}{dt} = -c\dfrac{\partial H}{\partial \varepsilon} \\ \dfrac{d\varepsilon}{dt} = c\dfrac{\partial H}{\partial \varepsilon} - \dfrac{D}{T_0}\varepsilon - \dfrac{R(T_0)}{T_0} \end{cases} \tag{1.33}$$

In case of a pure sinusoidal RF voltage the term $V(z)$ can be written in the form:

$$V(z) = V_{RF}\cos\left(\phi_s - 2\pi\frac{h}{L_0}z\right) \tag{1.34}$$

where h is called *harmonic number* and ϕ_s *synchronous phase* (defined by $\cos(\phi_s)=U_0/eV_{RF}$)
Neglecting the non conservative terms D, V' and $R(T_0)$ the equation of motion becomes:

$$\frac{d^2z}{dt^2} + \frac{c\alpha_c}{E_0T_0}eV_{RF}\cos\left(\phi_s - 2\pi\frac{h}{L_0}z\right) - \frac{c\alpha_c}{E_0T_0}U_0 = 0 \tag{1.35}$$

For small oscillation amplitudes[6] the longitudinal equation of motion can be written in the form:

$$\frac{d^2z}{dt^2} + \underbrace{\frac{\alpha_c 2\pi he}{E_0T_0^2}V_{RF}\sin(\phi_s)}_{\omega_s^2}z = 0 \tag{1.36}$$

[6] Under this condition ($z<<L_0/2\pi h$) $V(z)$ becomes:

$$V_{RF}(z) \cong \frac{U_0}{e} + \frac{2\pi h V_{RF}\sin(\phi_s)}{L_0}z$$

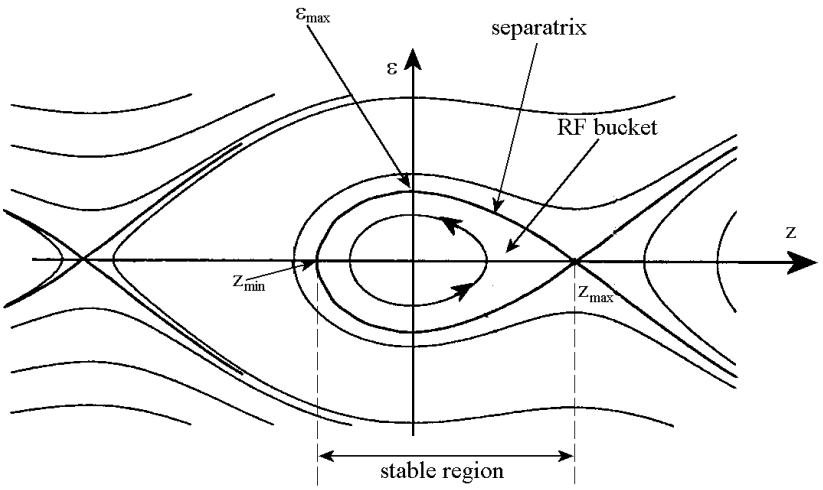

Fig. 1.3: trajectories of the particle in the phase space (z,ε).

Particles orbiting in a circular accelerator perform, therefore, longitudinal oscillations at the frequency $f_s=\omega_s/2\pi$ called *synchrotron frequency* and given by:

$$f_s = f_0\sqrt{\frac{\alpha_c}{2\pi E_0} heV_{RF}\sin(\phi_s)} \tag{1.37}$$

where f_0 is the revolution frequency ($f_0=1/T_0$).
These oscillations correspond to elliptical trajectories in the phase space (z,ε).
For large amplitudes the ellipses are distorted by the non-linearities of the motion but curves are still close on themselves until a certain maximum amplitude (Fig. 1.3). If the maximum amplitude overcomes the range z_{max}-z_{min} the motion becomes unstable and the particle motion assumes the characteristic of libration.
The lines separating the regime of libration from the regime of stable oscillation are called *separatrices* and the area within separatrices is commonly called the *RF bucket*.
The maximum energy deviation of a particle that perform stable oscillation is called *energy acceptance* (or momentum acceptance $\Delta p/p_0|_{max}$) and it is given by [20]:

$$\left.\frac{\varepsilon}{E_0}\right|_{max} = \sqrt{\frac{eV_{RF}}{\pi h\alpha_c E_0}\left[2\cos\phi_s - (\pi - 2\phi_s)\sin\phi_s\right]} \tag{1.38}$$

The energy acceptance plays an important role since it determines the capture efficiency at injection and the Touschek lifetime of stored beams (par. 1.5).

1.2.1 Distribution function and Fokker-Plank equation

To study the collective effects it is necessary to introduce the distribution function of the particles in the phase plane $\Psi(z,\varepsilon;t)$. As usually, the product $\Psi(z,\varepsilon;t)dzd\varepsilon$ is the probability to find one particle in the area $dzd\varepsilon$ of the phase space at the time t.
The *longitudinal distribution function* $\rho(z;t)$ is given by:

$$\rho(z;t) = \int_{-\infty}^{+\infty} \Psi(z,\varepsilon;t)d\varepsilon \tag{1.39}$$

The fraction of the total particles between z and $z+dz$ at the time t is given by $\rho(z;t)dz$.
Similarly the *energy distribution* is given by:

$$\rho_{\varepsilon}(\varepsilon;t) = \int_{-\infty}^{+\infty} \Psi(z,\varepsilon;t)dz \tag{1.40}$$

the *bunch length* and the *energy spread* are defined respectively as:

$$\sigma_z = \sqrt{\int_{-\infty}^{+\infty} \rho(z;t)(z-\bar{z})^2 dz}$$
$$\sigma_{\varepsilon} = \sqrt{\int_{-\infty}^{+\infty} \rho_{\varepsilon}(\varepsilon;t)(\varepsilon-\bar{\varepsilon})^2 d\varepsilon} \tag{1.41}$$

where $\bar{z}$ and $\bar{\varepsilon}$ are the mean values of the distributions (1.39)-(1.40).
The time evolution in the phase space of the distribution function is given by the *Fokker-Plank equation* [21,22]:

$$\frac{\partial\Psi}{\partial t} = -c\frac{\partial H}{\partial z}\frac{\partial\Psi}{\partial\varepsilon} + c\frac{\partial H}{\partial\varepsilon}\frac{\partial\Psi}{\partial z} + \frac{D}{T_0}\left(\frac{\partial\Psi}{\partial\varepsilon}\varepsilon + \Psi\right) + \frac{1}{2}\frac{\partial^2\Psi}{\partial\varepsilon^2}\frac{\left\langle R(T_0)^2\right\rangle}{T_0} \tag{1.42}$$

where $\langle R(T_0)^2\rangle$ represents the standard deviation of the radiated energy.
The first two terms on the right are related to the conservative forces acting on the bunch while the third and the fourth terms represent the radiation term and the effect of the quantum excitation respectively.
Both the coefficient D and the standard deviation $\langle R(T_0)^2\rangle$ can be calculated knowing the characteristics of the magnets in the accelerator [23].
The Fokker Plank equation represents the more general expression to describe the evolution of the distribution function in the phase plane both in the single bunch and in the multi-bunch case. Unfortunately the analitycal solution of this equation doesn't exist and, in order to study the single or the multi-bunch beam dynamics, some assumptions have to be done to simplify the problem.

1.2.2 Stationary distribution: the Haissinski equation

Experimentally when the number of particles is low, the bunch distribution is time independent. Under this condition ($\partial/\partial t=0$) the Fokker-Plank equation becomes solvable and the distribution function is given by [24]:

$$\Psi(z,\varepsilon)=\overline{\Psi}e^{-\frac{D}{\left\langle R(T_0)^2\right\rangle}\varepsilon^2-\frac{2E_0^2D}{\alpha_c^2\left\langle R(T_0)^2\right\rangle}\varphi(z)} \tag{1.43}$$

The equation (1.43) is called the *Haissinki equation* and, integrated over z or ε, allows to find the longitudinal and the energy distribution function respectively:

$$\rho(z)=\overline{\rho}e^{-\frac{2E_0^2D}{\alpha_c^2\left\langle R(T_0)^2\right\rangle}\varphi(z)}=\overline{\rho}e^{-\frac{E_0^2}{\alpha_c^2\sigma_{\varepsilon 0}^2}\varphi(z)} \tag{1.44}$$

$$\rho_\varepsilon(\varepsilon)=\overline{\rho}_\varepsilon e^{-\frac{D}{\left\langle R(T_0)^2\right\rangle}\varepsilon^2}=\overline{\rho}_\varepsilon e^{-\frac{\varepsilon^2}{2\sigma_{\varepsilon 0}^2}} \tag{1.45}$$

It is important to observe that, in the stationary case, the energy distribution function does not depend on the potential well but only on the machine parameters and it has a gaussian profile. On the other hand, the longitudinal distribution depends on the potential well.

At very low bunch current, neglecting the self field and considering a sinusoidal accelerating voltage[7] the longitudinal bunch distribution becomes simply:

$$\rho(z)=\overline{\rho}e^{-\frac{z^2}{2\sigma_{z0}^2}} \tag{1.46}$$

where the σ_{z0} is given by:

$$\sigma_{z0}=\sigma_{\varepsilon 0}\frac{\alpha_c c}{E_0\omega_s} \tag{1.47}$$

If the bunch current increases, however, it is not possible to neglect the self-field and the (1.44) becomes (see Appendix A1.1):

$$\rho(z)=\overline{\rho}e^{-\frac{z^2}{2\sigma_{z0}^2}-\frac{E_0Q}{\alpha_c L_0\sigma_\varepsilon^2}e\int_0^z dz''\int_{-\infty}^{\infty}\rho(z')w_z(z'-z'')dz'} \tag{1.48}$$

where Q is the bunch total charge.

The self-induced e.m. fields cause the so-called *potential well distortion* and deform the original gaussian distribution function.

[7] Linearized near the point z=0.

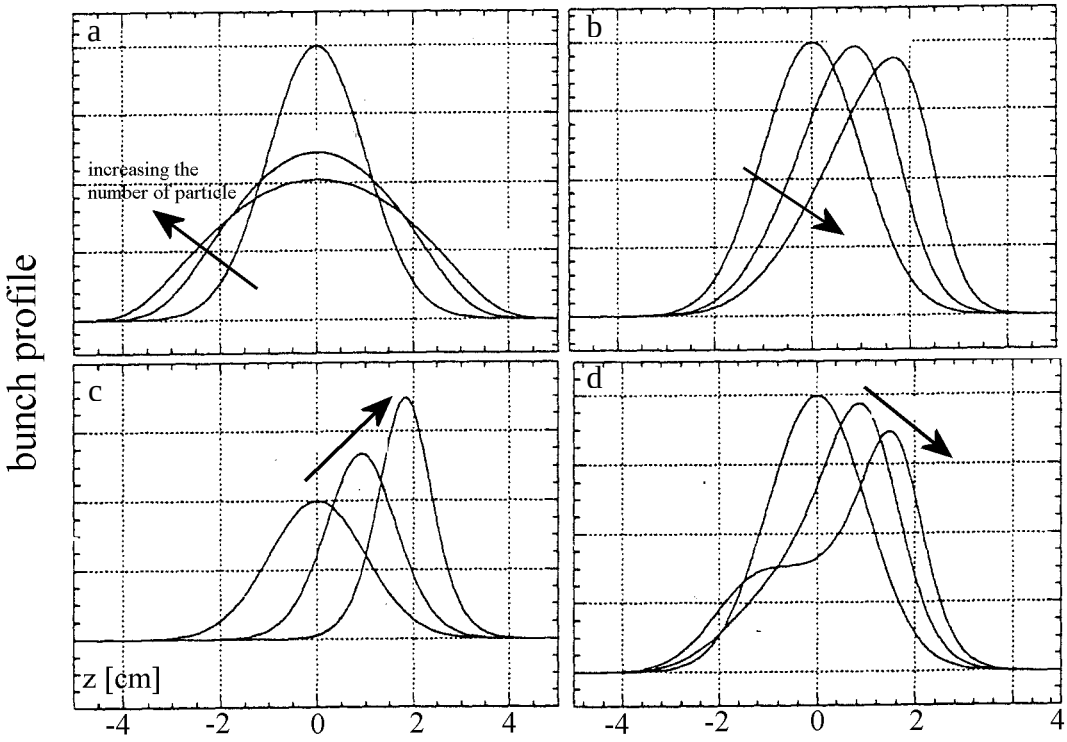

Fig. 1.4: longitudinal bunch distributions as a function of the number of particles for different types of impedance: (a) purely inductive; (b) resistive; (c) purely capacitive; (d) broad band resonator.

The integral equation (1.48) is, in general, numerically resolvable and, knowing the characteristics of the accelerator impedance, it allows finding the longitudinal distribution of the bunch as a function of current [22,25].
Typical longitudinal bunch distributions are shown in Fig. 1.4 as a function of the number of particles and for different types of impedance. A pure inductive wake (Fig. 1.4a) does not give energy losses, the bunch remains therefore symmetric and assumes a parabolic shape. With the other types of wake there is a change in the shape of the longitudinal distribution and, moreover, the bunch center of mass moves in order to compensate the energy losses.
As remarked initially, the equation (1.43) is valid for a stationary bunch. In the synchrotron machines, however, this hypothesis is not satisfied at high bunch density current and other phenomena have to be taken into account to explain the behavior of the bunch distribution.

1.2.3 Perturbative theory and turbulent regime

If the characteristic times of the dangerous instabilities are shorter compared to those of the damping and diffusion phenomena one can neglect, in the Fokker-Plank

equation, the terms related to the diffusion and radiation phenomena obtaining the so called *Vlasov equation*:

$$\frac{\partial \Psi}{\partial t} = -c\frac{\partial H}{\partial z}\frac{\partial \Psi}{\partial \varepsilon} + c\frac{\partial H}{\partial \varepsilon}\frac{\partial \Psi}{\partial z} \tag{1.49}$$

Following the treatment originally proposed by F. Sacherer [26] and successively developed by other authors [27], the time dependent Ψ can be written as a sum of the stationary distribution Ψ_0 and of a coherent perturbation Ψ_1 in the form[8]:

$$\Psi(\hat{z},\phi;t) = \Psi_0 + \underbrace{e^{j\Omega t}\sum_{m=-\infty}^{\infty} R_m(\hat{z})e^{-jm\phi}}_{\Psi_1(\hat{z},\phi;t)} \tag{1.50}$$

where $\hat{z}$ and ϕ are polar coordinates in the phase space (z,ε).
Supposing that the Ψ_1 function is a weak perturbation of the unperturbed distribution Ψ_0 and that the characteristic time of the dangerous instabilities are shorter compared to those of the damping and diffusion phenomena, one can use the Vlasov equation with the expression (1.50) obtaining the following eigenvalue system for the radial function R_m:

$$(\Omega - m\omega_{s0})R_m(\hat{z}) = -j\frac{mceQ}{\hat{z}T_0}\frac{\partial \Psi_0(\hat{z})}{\partial \hat{z}}\sum_{l=-\infty}^{\infty} j^{m-l}\int_{-\infty}^{\infty}\frac{Z(\omega)}{\omega}J_m\left(\frac{\omega}{c}\hat{z}\right)d\omega\int_0^{\infty} R_l(\hat{z}')J_l\left(\frac{\omega}{c}\hat{z}'\right)\hat{z}'\,d\hat{z}' \tag{1.51}$$

where J_m is the Bessel of order m.
In the case of zero current (Q=0) one obtains the following eigenvalue and eigenvectors:

$$\begin{aligned}\Omega^{(m)} &= m\omega_{s0}\\ R_{m'}^{(m)} &= \delta_{mm'}\end{aligned} \tag{1.52}$$

And the possible coherent mode of oscillations can be written in the form:

$$\Psi_{1m}(\hat{z},\phi;t) = e^{jm(\omega_{s0}t-\phi)} \tag{1.53}$$

where each mode is determined by the azimuthal number m.
If the bunch current increases the equations (1.51) should be solved in order to find the coherent modes of oscillation.

[8] In the ($\hat{z}$,ϕ) plane the Ψ_1 function is periodic with respect to ϕ of 2π and it is possible to consider its Fourier expansion obtaining the expression (1.50).

Experimentally, when the single bunch current increases above a certain threshold, the energy spread of the bunch starts growing (contrary to the Haissinski equation). This effect is know as the *microwave instability*, because of the high frequency signals that can be observed in these conditions. The consequent bunch lengthening is very fast and the phenomenon is also called *turbulent* since the high frequency signals often become fluctuating or turbulent. The physical nature of the turbulence is not well understood and several different theories based on the solutions of the eq. (1.51) or based on empirical results, have been developed [28,29].
It is widely believed [27,30,31] that these phenomena are caused by the bunch longitudinal coherent mode coupling. The instability can manifest itself either through the coupling among the azimulthal modes or the radial ones having the same azimuthal number.
Usually the empirical Boussard criterion [32] is used to estimate the threshold for the instability. The discussion of the applicability of the criterion can be found, for example, in [28]. The criterion establishes that above the threshold current given by the relation:

$$\frac{eI_p\left|Z(n)/n\right|}{2\pi\alpha_c\sigma_\varepsilon^2 E_0}\le 1 \tag{1.54}$$

where I_p is the peak current, Z is the broad band impedance and $n=\omega_c/\omega_0$ with $\omega_c=c/\sigma_z$, the bunch "enters" in the turbulent regime.
In the criterion expressed by eq. (1.54) both I_p and $Z(n)/n$ depend on the bunch length, which is proportional to the energy spread. For a gaussian bunch the peak current is given by:

$$I_p=\frac{cQ}{\sqrt{2\pi}\sigma_z} \tag{1.55}$$

In the equation (1.54) the equality shows the threshold value for the bunch charge Q given by:

$$Q_{\max}=\frac{(2\pi)^{5/2}\sigma_{z0}^3}{c^2T_0L_0}E_0^2\frac{hV_{RF}\sin(\phi_s)}{\left|Z(n)/n\right|} \tag{1.56}$$

where σ_{z0} is given by (1.47).
Below this value the Haissinski equation can be solved obtaining a constant value $\sigma_{\varepsilon 0}$ and the bunch length σ_z. Above this value it is possible to estimate a theoretical σ_z by solving the equations (1.54) with the sign "="and (1.44) obtaining [33]:

$$\sigma_z=\left[\frac{c^2QT_0L_0V_{RF}\sin(\phi_s)}{(2\pi)^{5/2}}\left|\frac{Z(n)}{n}\right|\right]^{1/3} \tag{1.57}$$

1.2.4 Single bunch dynamics simulations

The analytical treatment of the single bunch turbulent regime is important in order to understand the physical phenomena in the single bunch dynamics. However, the theoretical estimates of the bunch length and energy spread are valid under certain conditions and, in general, do not include the all effects as the azimuthal and radial mode coupling.
To resolve the problem, as a whole, simulation programs based on finite difference equations have been developed [30,13,34-36].
The motion of N_s macroparticles representing the bunch of total charge Q is described in the longitudinal phase space by the equations:

$$\begin{cases} z_i^n = z_i^{n-1} - L_0 \alpha_c \dfrac{\varepsilon_i^{n-1}}{E_0} \\ \varepsilon_i^n = \varepsilon_i^{n-1} + e\left[V\left(z_i^n\right) + V'\left(z_i^n\right)\right] - U_0 - D\varepsilon_i^{n-1} - \sigma_{\varepsilon 0} R\sqrt{2D} \end{cases} \tag{1.58}$$

where ε_i^n and z_i^n, are the energy and position coordinates of the macroparticle i after n revolutions in the storage ring.
Following the treatment reported in [18], the statistical quantity $R(T_0)$ in the (1.28) has been substituted with the quantity:

$$R\left(T_0\right) = \sigma_{\varepsilon 0} R\sqrt{2D} \tag{1.59}$$

where R is a random number obtained from a normally distributed set with mean 0 and σ=1.
The accelerating voltage is simply given by:

$$V\left(z_i^n\right) = V_{RF} \cos\left(\phi_s - \frac{2\pi h}{L_0} z_i^n\right) \tag{1.60}$$

while the voltage induced by the short range wake fields is given by:

$$V'\left(z_i^n\right) = -\frac{eN_p}{N_s} \sum_{z_j^n > z_i^n}^{j=1,N_s} w_z\left(z_j^n - z_i^n\right) \tag{1.61}$$

where $w_z(z)$ is the machine wake function.
In order to reduce the computing time the macroparticles are distributed in N_{bin} and the induced voltage is calculated as:

$$V'\left(z_i\right) = -\frac{eN_p}{N_s} \sum_{z_j > z_i}^{j=1,N_{bin}} N_b\left(z_j\right) w_z\left(z_j - z_i\right) \tag{1.62}$$

where z_j are the coordinates of the bin centers and $N_b(z_j)$ is the number of macroparticles in the bin with the center at z_j.
The induced voltage at the position of the macroparticles is found by a linear interpolation between the $V'(z_i)$.
The parameters N_s and N_{bin} have to be chosen in order to minimize the computing time avoiding, contemporary, artificial numerical errors.
As an example, the results of the numerical simulations for the DAΦNE main rings are summarized in Fig. 1.5. The main DAΦNE design parameters are shown in Table 1.1 and the wake function[9] as calculated by numerical codes [37] is reported in Fig. 1.6.
In the simulations $3 \cdot 10^5$ macroparticles have been tracked over 4 damping times. The figures shows the σ_z and σ_ε/E_0 as a function of bunch current, calculated for two RF voltages (V_{RF}=100 KV and V_{RF}=250 KV).
The normalized bunch profile with V_{RF}=250 KV obtained by the simulation is reported in Fig. 1.7a. The distribution is wider than a gaussian due to the bunch interaction with the inductive machine impedance and slightly distorted due to the real component of the impedance. The microwave instability threshold is lower and the bunch energy spread is higher for the higher RF voltages, as expected because of the high density current.
In the Fig. 1.7b the σ_z and the σ_ε/E_0 are plotted as a function of the turn number. It is clear that the regime is not a stationary one and both quantities oscillate turn by turn.

Table 1.1: DAΦNE design parameters

Energy (E_0)	510 [MeV]
RF frequency (f_{RF})	368.26 [MHz]
Harmonic number (h)	120
Revolution frequency (f_0)	3.0688 [MHz]
Machine length (L_0)	96,6 [m]
Momentum compaction (α_c)	0.017
Maximum current per bunch (I_{bmax})	44 [mA]
RF Voltage (V_{RF})	100÷250 [KV]
Damping time (τ_D)	17.8 [ms]
Max. beam current (I_{max})	5.2 [A]
Max. number of colliding bunches (N_b)	120
Synchrotron losses (U_0)	9.3 [KeV/turn]
Natural bunch length (σ_{z0})	1.3÷0.8 [cm]

[9] More precisely, the wake function is substituted with the wake potential of a very short bunch (2.5 mm) because the numerical codes can not calculate the e.m. field for a δ-function current distribution.

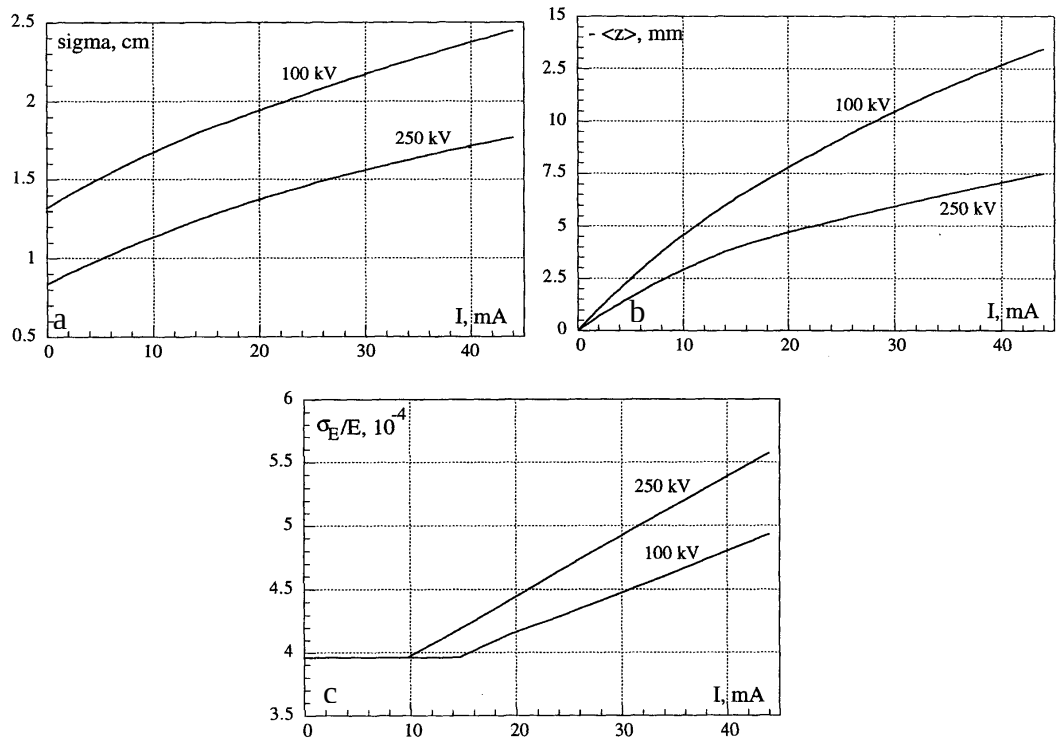

Fig. 1.5: results of the numerical simulations obtained with the single bunch simulation code: (a) rms bunch length; (b) bunch centroid; (c) rms energy spread.

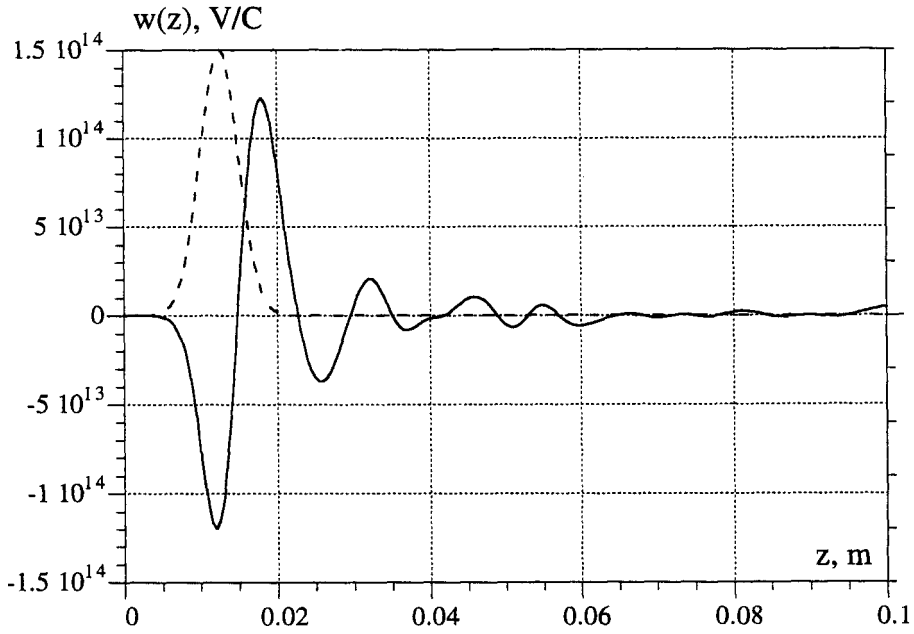

Fig. 1.6: DAΦNE wake potential of a 2.5 mm gaussian bunch.

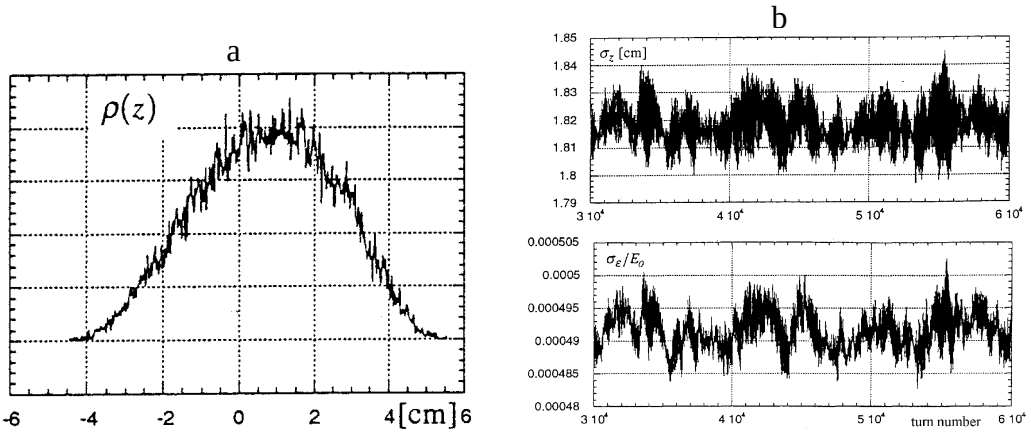

Fig. 1.7: (a) Normalized bunch profile with V_{RF}=250 KV obtained by the simulation code; (b) bunch length and energy spread as a function of the turn number with V_{RF}=250 KV.

1.3 Multi-bunch beam dynamics

Up to now only the effects of the short range wake fields in the single bunch dynamics have been taken into account. They give an increase of the σ_z and can cause microwave instabilities and energy spread growth.
In an accelerator, however, the complete single and multi-bunch beam dynamics is determined by the combined effects of the short and long range wake fields and by the non linear effects of the accelerating field.
It is pratically impossible to do a complete analytical study of the single/multi-bunch beam dynamics for high bunch current and some simplifications have to be done.

1.3.1 Macroparticle model

A simplified model for the study of the coherent effects produced by the long range wake fields is the so called *macroparticle model*. It is based on the assumption to consider each bunch as a macroparticle without internal structure neglecting the intrabunch collective motions. The macroparticles can be modeled as a pure δ-functions (σ_z=0) or as a rigid profile distributions (for example gaussian) with a certain σ_z.

Supposing N_b equispaced δ-macroparticles of charge Q, the equation of motion for each bunch with respect to the "synchronous position" can be written in the form[10]:

$$\frac{d^2 z_n}{dt^2} + \frac{D}{T_0}\frac{dz_n}{dt} + \frac{c\alpha_c}{E_0 T_0} eV_T(z_n) - \frac{c\alpha_c}{E_0 T_0} U_0 = 0 \tag{1.63}$$

Where the quantum fluctuation given by the term $R(T_0)$ has been neglected[11].
The total accelerating voltage $V_T(z_n)$ is given by the RF system and by the long range wake fields by the equation:

$$V_T(z_n) = V_{RF} \cos\left(\phi_s - \frac{2\pi h}{L_0} z_n\right) + V_w^n \tag{1.64}$$

where the synchronous phase ϕ_s does not depend on the considered bunch because the bunches are equispaced and they have the same charge[12]. The total voltage induced by the long range wake fields on the macroparticle n, is given by the sum of the particles contributions in all the previous turns[13]:

$$V_w^n = -\sum_{h=0}^{N_b-1}\sum_{q=0}^{\infty} Q w_z \left\{\left(q - \frac{h}{N_b} + \frac{n}{N_b}\right)L_0 + z_h\left[t - \left(q - \frac{h}{N_b} + \frac{n}{N_b}\right)T_0\right] - z_n(t)\right\} \tag{1.65}$$

Under the condition of small oscillation amplitudes (z_n, $z_h << L_0/N_b$) it is possible to make a linear expansion of the voltages:

$$V_w^n \cong -\sum_{h=0}^{N_b-1}\sum_{q=0}^{\infty} Q\left\{w_z\left[\left(q - \frac{h}{N_b} + \frac{n}{N_b}\right)L_0\right] + \left.\frac{dw_z}{dz}\right|_{\left(q-\frac{h}{N_b}+\frac{n}{N_b}\right)L_0}\left[z_h\left(t - \left(q - \frac{h}{N_b} + \frac{n}{N_b}\right)T_0\right) - z_n(t)\right]\right\} \tag{1.66}$$

$$V_{RF}\cos\left(\phi_s - \frac{2\pi h}{L_0} z_n\right) \cong V_{RF}\cos(\phi_s) + \frac{2\pi h V_{RF}\sin(\phi_s)}{L_0} z_n \tag{1.67}$$

The equation of motion becomes:

$$\frac{d^2 z_n}{dt^2} + \frac{D}{T_0}\frac{dz_n}{dt} + \omega_s^2 z_n = \frac{c\alpha_c e}{E_0 T_0}\sum_{h=0}^{N_b-1}\sum_{q=0}^{\infty} Q\left\{\left.\frac{dw_z}{dz}\right|_{\left(q-\frac{h}{N_b}+\frac{n}{N_b}\right)L_0}\left[z_h\left(t - \left(q - \frac{h}{N_b} + \frac{n}{N_b}\right)T_0\right)\right]\right\} \tag{1.68}$$

[10] $z_i>0$ means that the macroparticle is ahead of the "synchronous position".
[11] The quantum fluctuations in the emission of synchrotron radiation are a single particle motion property and do not affect the multibunch macroparticle motion.
[12] From this point of view the bunches are undistinguishable.
[13] The espression of the wake field can be given as a function of z where $z=c\tau$.

with the *incoherent angular frequency*[14] and *synchronous phases* defined by[15]:

$$\omega_s^2 = \frac{c\alpha_c e}{E_0 T_0}\left\{\frac{2\pi h V_{RF}\sin(\phi_s)}{L_0} + \sum_{h=0}^{N_b-1}\sum_{q=0}^{\infty} Q\frac{dw_z}{dz}\bigg|_{\left(q-\frac{h}{N_b}+\frac{n}{N_b}\right)L_0}\right\} =$$

$$= \frac{c\alpha_c e}{E_0 T_0}\left\{\frac{2\pi h V_{RF}\sin(\phi_s)}{L_0} - \sum_{k=0}^{\infty}\frac{2\pi k N_b}{L_0} 2I\,\mathrm{Im}\left[Z(kN_b\omega_0)\right]\right\} \tag{1.69}$$

$$eV_{RF}\cos(\phi_s) = U_0 + e\sum_{h=0}^{N_b-1}\sum_{q=0}^{\infty} Qw_z\left[\left(q-\frac{h}{N_b}+\frac{n}{N_b}\right)L_0\right] = U_0 + 2I\sum_{k=0}^{\infty}\frac{2\pi k N_b}{L_0}\mathrm{Re}\left[Z(kN_b\omega_0)\right] \tag{1.70}$$

The last equalities in the equations (1.69)-(1.70) are proved in Appendix A1.2.
The N_b equations given by (1.68) represent a system of coupled oscillators.
The solution of the system can be found in the form:

$$z_n(t) = a_n e^{j\Omega t} \tag{1.71}$$

obtaining the following eigenvalue problem (see Appendix A1.3):

$$\left(\Omega^2 - j\frac{D}{T_0}\Omega - \omega_s^2\right)a_n = \sum_{h=0}^{N_b-1} a_h M_{nh}(\Omega) \tag{1.72}$$

where:

$$M_{nh}(\Omega) = j\frac{c\alpha_c e}{E_0 T_0 L_0} Q\sum_{p=-\infty}^{\infty}(p\omega_0 - \Omega)Z^*(p\omega_0 - \Omega)e^{-j2\pi p\left(\frac{n-h}{N_b}\right)} \tag{1.73}$$

The matrix $|M_{nh}(\Omega)|$ is a cyclic matrix [38] and the N_b eigenvalues give the following complex frequencies of oscillation:

$$\Omega_\mu^2 - j\frac{D}{T_0}\Omega_\mu - \omega_s^2 = j\frac{c\alpha_c e}{E_0 T_0 L_0} QN_b\sum_{l=-\infty}^{\infty}\left(p_{l\mu} - \Omega_\mu\right)Z^*\left(p_{l\mu} - \Omega_\mu\right) \tag{1.74}$$

where $p_{l\mu} = (N_b l - \mu)\omega_0$ and μ=0,1,2,…,N_b-1 is the mode number. The corresponding eigenvectors are:

$$a_{n\mu} = a_{0\mu} e^{j\frac{2\pi}{N_b}n\mu} \tag{1.75}$$

[14] ω_s is related to the slope of the total RF voltage: the accelerating one+the voltage induced by the wake fields.
[15] In the summations (1.69-70) the impedance Z does not include the fundamental mode in the main cavity that is already taken into account in the cosine term (in other words, the beam loading in the main cavity is compensated by the external RF generator).

The multibunch modes of oscillation are, therefore, characterized by a proper coherent angular frequency given by $\mathrm{Re}[\Omega_\mu]=\omega_{c\mu}$, by a growth rate given by $\mathrm{Im}[\Omega_\mu]=\alpha_{c\mu}$ and by a proper phase relationship between the amplitudes a_n.
In Fig. 1.8 as an example the modes 0 and π are schematically represented.
Assuming that $D/T_0 << \alpha_{c\mu}$ and that $\alpha^2 << \Omega^2, \omega_s^2$ ([16]) the coherent angular frequency of oscillation and the corresponding growth rate of the mode μ are given by:

$$\omega_{c\mu}^2 = \omega_s^2 \left\{ 1 + \frac{I\alpha_c e}{E_0 T_0 \omega_s^2} \sum_{l=-\infty}^{\infty} \left(p_{l\mu} - \Omega_\mu \right) \mathrm{Im}\left[Z\left[p_{l\mu} - \Omega_\mu \right] \right] \right\} =$$
$$\omega_s^2 \left\{ 1 + \frac{I\alpha_c e}{E_0 T_0 \omega_s^2} \sum_{l=0}^{\infty} \left\{ \begin{array}{l} \left(p_{l\mu} - \Omega_\mu \right) \mathrm{Im}\left[Z\left[p_{l\mu} - \Omega_\mu \right] \right] + \\ + \left(p_{l(-\mu)} + \Omega_\mu \right) \mathrm{Im}\left[Z\left[p_{l(-\mu)} + \Omega_\mu \right] \right] \end{array} \right\} \right\} \qquad (1.76a)$$

$$\alpha_{c\mu} = \frac{I\alpha_c e}{2\omega_{c\mu} E_0 T_0} \sum_{l=0}^{\infty} \left\{ \begin{array}{l} \left(p_{l\mu} - \Omega_\mu \right) \mathrm{Re}\left[Z\left[p_{l\mu} - \Omega_\mu \right] \right] - \\ + \left(p_{l(-\mu)} + \Omega_\mu \right) \mathrm{Re}\left[Z\left[p_{l(-\mu)} + \Omega_\mu \right] \right] \end{array} \right\} \qquad (1.76b)$$

where $I=QN_b/T_0$ is the average beam current.
The imaginary part of the impedance gives, therefore, a shift of the coherent angular frequency of the mode with respect to the incoherent angular frequency ω_s while the real part determines whether the mode is stable ($\alpha>0$) or unstable ($\alpha<0$)[17].

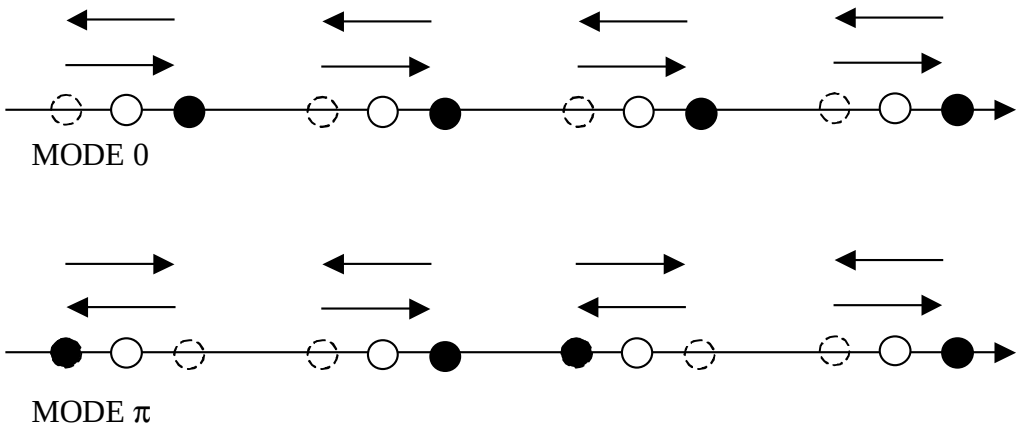

Fig. 1.8: schematic representation of the modes 0 and π.

[16] The dangerous unstable modes satisfy always these conditions.
[17] In the equations (1.76) the coherent frequency of oscillation appears in both sides. In order to evaluate the growth rate and the coherent angular frequency it is necessary to solve the equation numerically or to suppose small coherent angular frequency shift ($\omega_{c\mu} \cong \omega_s$) in order to approximate Ω_μ in the the right side of the equations with ω_s.

The fact that the impedance has to be evaluated at the angular frequencies $\omega_{l\mu}=(N_b l-\mu)\omega_0-\Omega_\mu$ can be intuitively understood looking at the *spectrum of an oscillating beam* given by (see Appendix A1.4):

$$I(\omega)=I\sum_{l=-\infty}^{\infty}\delta(\omega-N_b l\omega_0)-jI\frac{a}{2c}\sum_{l=-\infty}^{\infty}p_{l\mu}\delta(\omega-p_{l\mu}+\Omega_\mu)=$$
$$=I\sum_{l=-\infty}^{\infty}\delta(\omega-N_b l\omega_0)-jI\frac{a}{2c}\sum_{l=0}^{\infty}\left\{p_{l\mu}\delta(\omega-p_{l\mu}+\Omega_\mu)-p_{l(-\mu)}\delta(\omega+p_{l(-\mu)}-\Omega_\mu)\right\} \tag{1.77}$$

In the frequency domain, the interaction between the bunches is generated through the coupling impedance of the accelerator at the frequencies corresponding to the line spectrum of the oscillating bunches. The first summation does not depend on the bunch oscillation amplitude (the corresponding lines are often called *power spectrum lines*) while the second summation gives the so-called *synchrotron sidebands* proportional to the oscillation amplitude.
If the major contribution to the impedance is given by a high Q resonator the formulae can be simplified considering in the summations (1.76) only the spectrum lines near the resonant frequency of the resonator. If, as an example, its resonant frequency is between the angular frequencies $(N_b+1)\omega_0$ and $(N_b+2)\omega_0$ (as shown in Fig. 1.9), the real part of the impedance gives the following growth rates for the modes $\mu=1$, $\mu=2$, $\mu=N_b-1$, $\mu=N_b-2$:

$$\alpha_{c1}=-\frac{I\alpha_c e}{2\omega_{c\mu}E_0T_0}((N_b l+1)\omega_0+\Omega_1)\mathrm{Re}[Z[(N_b l+1)\omega_0+\Omega_1]]$$
$$\alpha_{c2}=-\frac{I\alpha_c e}{2\omega_{c\mu}E_0T_0}((N_b l+2)\omega_0+\Omega_2)\mathrm{Re}[Z[(N_b l+2)\omega_0+\Omega_2]]$$
$$\alpha_{cN_b-1}=\frac{I\alpha_c e}{2\omega_{c\mu}E_0T_0}((N_b l+1)\omega_0-\Omega_{N_b-1})\mathrm{Re}[Z[(N_b l+1)\omega_0-\Omega_{N_b-1}]]$$
$$\alpha_{cN_b-1}=\frac{I\alpha_c e}{2\omega_{c\mu}E_0T_0}((N_b l+2)\omega_0-\Omega_{N_b-2})\mathrm{Re}[Z[(N_b l+2)\omega_0-\Omega_{N_b-2}]] \tag{1.78}$$

The real part of the impedance makes unstable the modes $\mu=1$ and $\mu=2$ and stable the modes $\mu=N_b-1$ and $\mu=N_b-2$.
Following these results it is possible to plot the so called stable and unstable sideband for the multibunch modes as a function of frequency (Fig. 1.10). This intuitive view of the possible coupled bunch instabilities excited by a given impedance is a useful method to evaluate easily the stable or unstable modes for a given impedance.

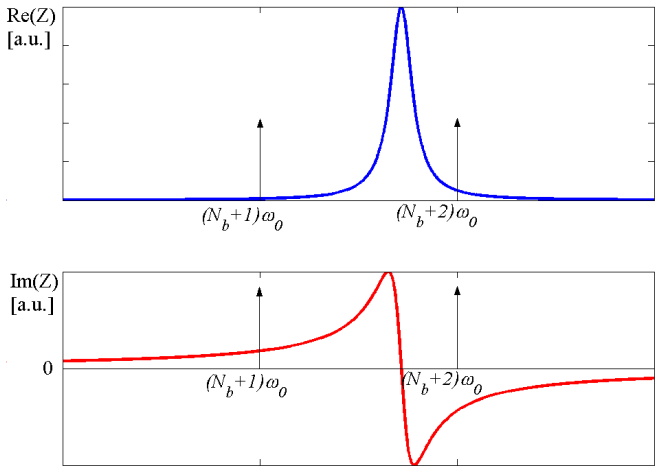

Fig. 1.9: narrow band impedance between $(N_b+1)\omega_0$ and $(N_b+2)\omega_0$.

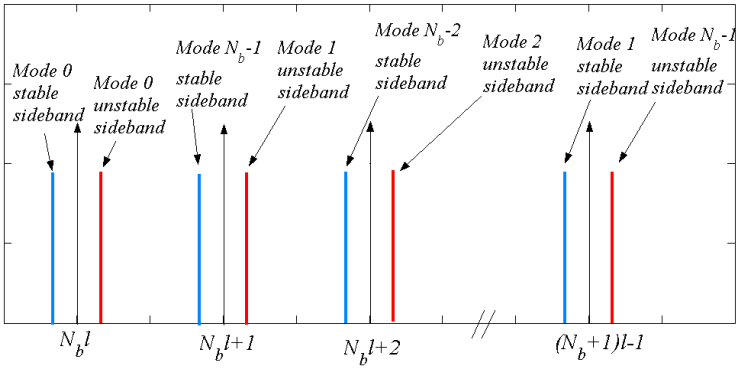

Fig. 1.10: stable and unstable lines of the multibunch modes

In the previous formulae the bunches have been modeled as δ-functions with σ_z=0. Assuming, instead, a gaussian rigid profile for the bunches, the previous formulae have to be modified as follows [41]:

$$\omega_{c\mu}^2 = \omega_s^2\left\{1+\frac{I\alpha_c e}{E_0 T_0 \omega_s^2}\sum_{l=-\infty}^{\infty}\left(p_{l\mu}-\Omega_\mu\right)\mathrm{Im}\left[Z\left(p_{l\mu}-\Omega_\mu\right)\right]e^{-\left[\frac{\left(p_{l\mu}-\Omega_\mu\right)\sigma_z}{c}\right]^2}\right\} =$$

$$\alpha_{c\mu} = \frac{I\alpha_c e}{2\omega_{c\mu}E_0 T_0}\sum_{l=-\infty}^{\infty}\left\{\left(p_{l\mu}-\Omega_\mu\right)\mathrm{Re}\left[Z\left(p_{l\mu}-\Omega_\mu\right)\right]e^{-\left[\frac{\left(p_{l\mu}-\Omega_\mu\right)\sigma_z}{c}\right]^2}\right\} \tag{1.79}$$

$$\omega_s^2 = \frac{c\alpha_c e}{E_0 T_0}\left\{\frac{2\pi h V_{RF}\sin(\phi_s)}{L_0}e^{-\frac{1}{2}\left(\frac{h\omega_0\sigma_z}{c}\right)^2} + \sum_{h=0}^{N_b-1}\sum_{q=0}^{\infty} Q\frac{d<W_z>}{dz}\bigg|_{\left(q-\frac{h}{N_b}+\frac{n}{N_b}\right)L_0}\right\} =$$

$$= \frac{c\alpha_c e}{E_0 T_0}\left\{\frac{2\pi h V_{RF}\sin(\phi_s)}{L_0}e^{-\frac{1}{2}\left(\frac{h\omega_0\sigma_z}{c}\right)^2} - \sum_{k=0}^{\infty}\frac{2\pi k N_b}{L_0}2I\,\mathrm{Im}\left[Z(kN_b\omega_0)\right]e^{-\left(\frac{kN_b\omega_0\sigma_z}{c}\right)^2}\right\}$$

$$eV_{RF}\cos(\phi_s) = U_0 + e\sum_{h=0}^{N_b-1}\sum_{q=0}^{\infty} Q<W_z>\left[\left(q-\frac{h}{N_b}+\frac{n}{N_b}\right)L_0\right] = U_0 + 2I\sum_{k=0}^{\infty}\frac{2\pi k N_b}{L_0}\mathrm{Re}\left[Z(kN_b\omega_0)\right]e^{-\left(\frac{kN_b\omega_0\sigma_z}{c}\right)^2} \tag{1.80}$$

where $<W_z>$ is the wake potential "averaged" over the bunch distribution.
The exponential factors take into account the finite length of the bunches. In fact, in this case, the spectrum of the oscillating bunches is given by:

$$I(\omega) = I\sum_{l=-\infty}^{\infty}\delta(\omega - N_b l\omega_0)e^{-\frac{1}{2}\left(\frac{N_b l\omega_0\sigma_z}{c}\right)^2} - jI\frac{a}{2c}\sum_{l=-\infty}^{\infty}p_{l\mu}\delta(\omega - p_{l\mu} + \Omega_\mu)e^{-\frac{1}{2}\left[\frac{(p_{l\mu}-\Omega_\mu)\sigma_z}{c}\right]^2} \tag{1.81}$$

1.3.2 Perturbative theory

The macroparticle model considers bunches as macroparticles without internal structure. The multibunch coherent effects in the distribution function can be treated starting from the Vlasov equation and following the perturbative treatment as done for the single bunch effects.
Assuming N_b equal spaced gaussian bunches and supposing that the time dependent wake fields do not modify the stationary distribution Ψ_0, one obtains the following complex coherent angular frequencies [26,27]:

$$\Omega_{m\mu} - m\omega_s = -jI\frac{\alpha mec^2}{\omega_s E_0 2\pi\sigma_z^2}\sum_{l=-\infty}^{\infty}\frac{Z(p_{l\mu}-\Omega_{m\mu})}{p_{l\mu}-\Omega_{m\mu}}e^{-\left[\frac{(p_{l\mu}-\Omega_{m\mu})\sigma_z}{c}\right]^2}I_m\left[\left(\frac{(p_{l\mu}-\Omega_{m\mu})\sigma_z}{c}\right)^2\right] \tag{1.82}$$

where I_m is the modified Bessel function. The modes are, now, characterized by two indices: the azimuthal one m (m=1,2,3,…), and that related to the coupled bunch motion μ.
As in the case of the macroparticle model, the imaginary part of $\Omega_{m\mu}$, if positive, indicates a possible unstable mode.

As evident from (1.82), for the first azimuthal mode m=1 (called dipolar mode of oscillation) the equation gives the same result of the macroparticle model in the case of small coherent frequency shift[18].
From the eq. (1.82) and from the properties of the Bessel functions the more dangerous azimuthal modes, for a given impedance, are those related to low values of m.

1.3.3 Beam-accelerating cavity interaction: beam loading

The accelerating field is provided to the beam by an external RF generator that excites an oscillating longitudinal electric field in the RF cavity (par. 2.1). The beam itself, nevertheless, excites a longitudinal electric field in the RF cavity that has to be properly compensated by the external RF generator and by the tuning system[19].
The general model to describe the interaction between the beam and the RF system is plotted in Fig. 1.11 [40]. In the figure the RLC circuit models the resonant cavity, the transformer models the coupler between the external generator I_g and the cavity and the current generator I models the beam.
The bunches can be considered as current pulses sampling the total accelerating voltage V_{RF} (given by the external RF generator and by the beam current itself) at the synchronous phases ϕ_s. In order to maintain the total accelerating voltage equal to V_{RF} with a reasonable amount of reflected power, the extra negative voltage generated by the beam has to be properly compensated.
The Fourier components I_p of a train of equally spaced non oscillating gaussian bunches are related to the beam current $I(t)$ by the relation[20]:

$$I(t) = \bar{I} + \sum_{p=1}^{\infty} \tilde{I}_p \cos(pN_b\omega_0 t) \tag{1.83}$$

where $\bar{I}$ is the average beam current and $\tilde{I}_p$ is given by:

$$\tilde{I}_p = 2I_p = 2\bar{I}e^{-\frac{1}{2}\left(\frac{pN_b\omega_0\sigma_z}{c}\right)^2} \tag{1.84}$$

[18] In this case $\Omega_{m\mu}$ in the right side of the equation (1.74) can be approximated by $m\omega_s$ and in the left side $\Omega^2-\omega_s^2 \cong 2(\Omega-\omega_s)\omega_s^2$. Moreover, $I_1(x)$ in the eq. (1.82) can be, in general, approssimated with x/2 since, in general, x<<1.
[19] As illustrated in par. 2.1 the tuning of the resonant frequency of a cavity is realized with devices (tuners) that slightly modify the volume of the cavity changing its resonant frequency.
[20] The Fourier components of a train of non-oscillating bunches are double the real part of the δ-function amplitudes of the beam spectrum (1.77) considered for ω>0.

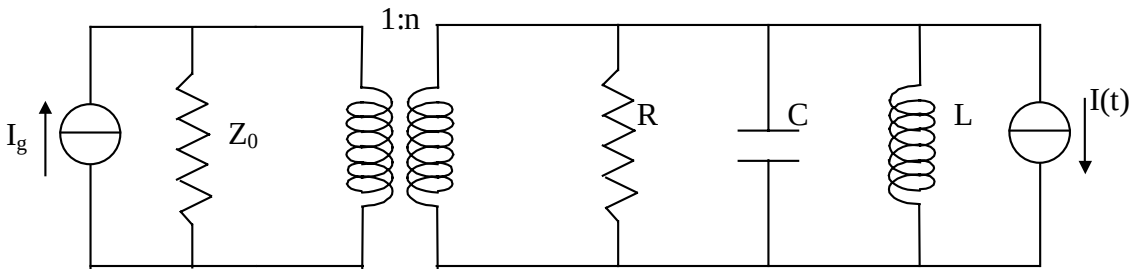

Fig. 1.11: equivalent circuit to describe the interaction between the beam and the RF system.

Analyzing the circuit of Fig. 1.11 at the RF harmonic, the beam is equivalent to an extra admittance loading the RF system and given by:

$$\frac{1}{Z_{beam}} = \frac{2I_p e^{-j\phi_s}}{V_{RF}} = \frac{2I_p \cos(\phi_s)}{V_{RF}} - j\frac{2I_p \sin(\phi_s)}{V_{RF}} \tag{1.85}$$

The beam loads the RF system as an extra resistance in parallel to an extra inductance which are both inversely proportional to the beam current.
The resistive part of the beam equivalent impedance describes the energy transfer from the RF source to the beam and gives a condition to optimize the coupling coefficient β (par. 2.1) for the best matching generator-loaded cavity:

$$\beta_{opt} = 1 + \frac{2RI_p \cos(\phi_s)}{V_{RF}} \tag{1.86}$$

The inductive part tends, on the other hand, to shift the resonant frequency of the cavity+beam system, and, beyond some current threshold, the system is too largely detuned that the RF generator can not sustain the required accelerating field anymore.
To avoid that, a tuning system automatically changes the resonant frequency of the cavity shifting it toward lower values to compensate the positive beam equivalent inductance.
The complex admittance of the loaded cavity as seen by the RF generator is given by:

$$\frac{1}{Z_{cav+beam}} = \left[\frac{1 + jQ_0\delta}{R} + \frac{2I_p \cos(\phi_s)}{V_{RF}} - j\frac{2I_p \sin(\phi_s)}{V_{RF}}\right] n^2 \tag{1.87}$$

The compensation of the beam reactance, if the cavity starts from perfect tune at zero current (δ_0=0), is simply given by:

$$Q_0\delta = \frac{R2I_p \sin(\phi_s)}{V_{RF}} \tag{1.88}$$

If, instead, the cavity starts from a non zero detune at zero current ($\delta_0 \neq 0$) the expression becomes[21]:

$$Q_0\delta = \frac{R2I_p \sin(\phi_s)}{V_{RF}} + Q_0\delta_0\left(1+\frac{R2I_p \cos(\phi_s)}{(1+\beta)V_{RF}}\right) \tag{1.89}$$

The cavity detuning, therefore, increases linearly with $\bar{I}$ and is inversely proportional to V_{RF}.

As an example the resonant frequency of the DAΦNE cavity is reported in Fig. 1.12 for two different accelerating voltages and initial detuning.

The impedance of the cavity interacts, also, with the two sidebands of the mode 0. The coherent angular frequency and the growth rate of the mode 0 are then given by:

$$\omega_{c0}^2 = \omega_s^2\left\{1+\frac{I\alpha_c e}{E_0 T_0 \omega_s^2}\{(h\omega_0-\Omega_0)\mathrm{Im}[Z(h\omega_0-\Omega_0)]+(h\omega_0+\Omega_0)\mathrm{Im}[Z(h\omega_0+\Omega_0)]\}\right\} \tag{1.90a}$$

$$\alpha_{c0} = \frac{I\alpha_c e}{2\omega_{c\mu}E_0 T_0}\{(h\omega_0-\Omega_0)\mathrm{Re}[Z(h\omega_0-\Omega_0)]-(h\omega_0+\Omega_0)\mathrm{Re}[Z(h\omega_0+\Omega_0)]\} \tag{1.90b}$$

The resonant frequency of the cavity ω_r is below $\omega_{RF}=h\omega_0$ and the mode 0 is, therefore, stable while its coherent angular frequency decreases accordingly to (1.90a).

[21] In order to compensate the beam inductance it is enough to put:

$$Q_0\delta = \frac{R2I_p \sin(\phi_s)}{V_{RF}} + Q_0\delta_0$$

However, the tuning system changes the tuner position in order to maintain constant the difference between the phase of the generator incident wave and the cavity voltage. This gives the equation (1.89).

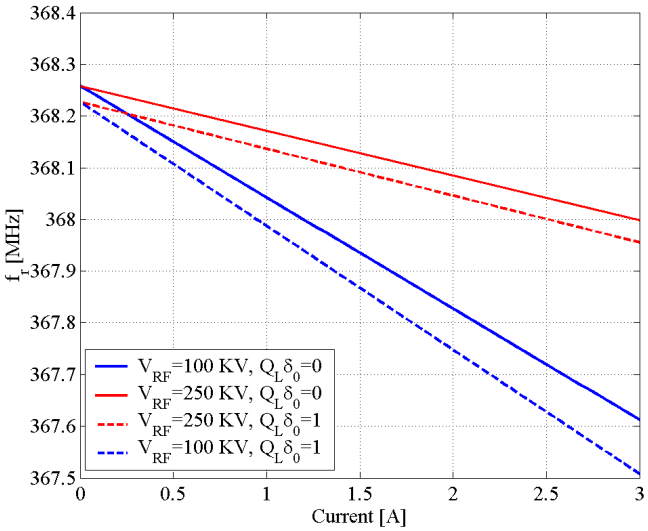

Fig. 1.12: resonant frequency of the DAΦNE cavity as a function of current.

1.3.4 Simulations of the multi-bunch longitudinal beam dynamics

As pointed out in the par. 1.3.1-1.3.2 the analytical study of the longitudinal beam dynamics of a beam interacting with an impedance can be performed only in the case of small oscillation amplitudes of equispaced and equal bunches. A complete analytical treatment of the beam dynamics in the presence of a bunch-by-bunch feedback system (that controls the longitudinal coupled bunch instabilities) and/or in the presence of bunches with different charge is, practically, impossible.
Simulation codes, that execute a tracking of the bunch longitudinal oscillations, allow to study the multibunch beam dynamics including the effects of the feedback system, HOMs interaction and synchrotron radiation damping.
In the code developed for the longitudinal beam dynamics study in DAΦNE [41], each bunch is modeled as a single macroparticle of a given charge. Under this condition it is possible to simulate only the "rigid" dipole oscillations that are, however, the most dangerous for the beam stability (par. 1.3.2).
The quantities necessary to describe the motion of the bunch n are the energy deviation ε_n with respect to the nominal energy E_0 and the phase deviation $\Delta\phi_n$ taken with respect to the synchronous one ($\Delta\phi_n=\varphi_{sn}-2\pi hz_n/L_0$).
The algorithm can be divided into three main parts:

a) propagation around the ring;
b) interaction with the accelerating mode in the RF cavity and with the impedances due trapped modes in the devices of the ring;
c) interaction with the feedback system.

Propagation around the ring

In the propagation around the ring, each bunch losses energy because of the synchrotron radiation (U_{rad}) and because of the interaction with the ring impedance (U_{imp}).
Following the treatment of par. 1.2 the energy deviation and the phase deviation at the exit of the ring are related to the input quantities by the equations:

$$\begin{cases} (\Delta\varphi_n)_{out} = (\Delta\varphi_n)_{inp} + \dfrac{2\pi h\alpha_c}{E_0}(\varepsilon_n)_{inp} \\ (\varepsilon_n)_{out} = (\varepsilon_n)_{inp} - \left(U_0 + D(\varepsilon_n)_{inp}\right) - U_{imp} \end{cases} \tag{1.91}$$

Interaction with the accelerating mode and HOMs

Both the interactions with the fundamental mode in the RF cavity and with the HOMs (in the cavity or in other devices of the ring) are modeled with lumped element circuits in the same point of the ring[22].
The variables $v_m(t)$ and $i_m(t)$ (voltage and current in the inductance respectively) execute free oscillations between the passage of two bunches and can be represented in the form [42]:

$$\begin{pmatrix} v_m(t) \\ i_m(t) \end{pmatrix} = e^{-\frac{\omega_{rm}}{2Q}t} \begin{pmatrix} \cos(\omega'_{rm}\,t) - \dfrac{\omega_{rm}}{2Q_m\omega'_{rm}}\sin(\omega'_{rm}\,t) & -\dfrac{\omega_{rm}R_m}{Q_m\omega'_{rm}}\sin(\omega'_{rm}\,t) \\ \dfrac{\omega_{rm}Q_m}{R_m\omega'_{rm}}\sin(\omega'_{rm}\,t) & \cos(\omega'_{rm}\,t) + \dfrac{\omega_{rm}}{2Q_m\omega'_{rm}}\sin(\omega'_{rm}\,t) \end{pmatrix} \begin{pmatrix} v_m(t_0) \\ i_m(t_0) \end{pmatrix} \tag{1.92}$$

where $v_m(t_0)$, $i_m(t_0)$ are the starting conditions and the quantities ω_{rm}, ω'_{rm}, Q_m and R_m are related to the mode m and have been defined in the par. 1.1.3.
When a bunch of charge Q_{bn} crosses the impedance it is sufficient to add the quantity:

$$\Delta V_m = -\frac{\omega_{rm}R_m}{Q_m}Q_{bn} \tag{1.93}$$

to $v_m(t)$ and to continue the propagation.
The phase and energy deviations after the interaction with the RF cavity and HOMs are, therefore, given by:

[22] The change in the longitudinal position in one turn along the ring is a negligible effect and all the impedances can be concentrated in the same point.

$$\begin{cases} (\Delta\varphi_n)_{out} = (\Delta\varphi_n)_{inp} \\ (\varepsilon_n)_{out} = (\varepsilon_n)_{inp} + eV_{RF}\cos(\Delta\varphi_n)_{inp} + \sum_m v_m(t_n) + \frac{1}{2}\sum_m \Delta V_m \end{cases} \tag{1.94}$$

where the interaction with the fundamental mode cavity impedance has been included in the summations and the last term is the energy lost by the bunch and stored in the HOMs as the fundamental theorem of the beam loading states (see eq. (1.21)).

Interaction with the feedback system

Because of the high current stored in modern storage rings like DAΦNE, coupled bunch instabilities driven by the HOMs in the accelerating cavity or in other devices of the ring, have fast rise times.
A powerful longitudinal feedback [43,44] is necessary to damp the dipole oscillations and, in the simulation code, this device is properly included.
The system installed in DAΦNE is a bunch by bunch time domain feedback also adopted in other factories [45]. The system provides the correction energy to each bunch at every turn by means of a longitudinal kick. The phase error signal, detected by a longitudinal pick-up, is digitized and processed with a DSP digital filter which computes the correction signal K_n by the algorithm:

$$K_n = G\sum_{i=1}^{N} c_i \Delta\varphi_{n-i} \tag{1.95}$$

The filter coefficients c_i are computed in order to provide the -90° shift necessary to convert the phase error into the energy correction and G is the DSP gain.
The DSP output is amplified and sent through a digital-analog converter to a kicker amplifier. In the simulations code developed for DAΦNE, the input file concerning the feedback allows to change the system configuration varying the gain of the different devices, the number of coefficients and the maximum kicker voltage.
In Fig. 1.13 it is shown a typical frequency response of the whole feedback chain.
The whole system provides, in general, the -90° degree shift for a certain frequency of the signal $\Delta\phi_n$. This frequency should correspond to the oscillation frequency of the unstable modes that, in case of small coherent frequency shift, corresponds to the incoherent synchrotron frequency. If the coherent frequency shifts induced by the impedances (in some modes) are not negligible the whole system has to be optimized in order to provide the optimum energy correction at the correct frequency.

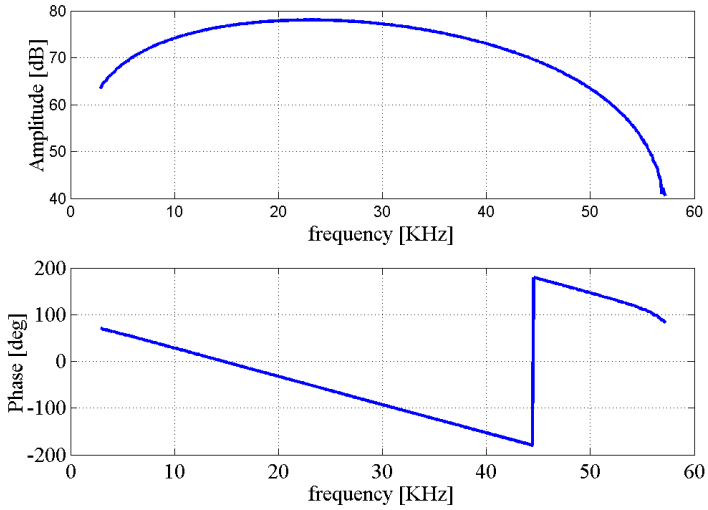

Fig 1.13: typical frequency response of the DAΦNE feedback chain.

1.4 Landau damping

As discussed in the previous paragraphs there is a large number of collective instability mechanisms acting on a high intensity beams.
Up to now the only considered damping mechanism is the natural damping induced by the radiation emission.
A strong effort, in the RF cavities design, is done to optimize the cavity shapes or to apply different HOM damping techniques in order to reduce the growth rates of the possible instabilities [48-53]. Comparing, however, the characteristic rise time of the possible coupled bunch instabilities (induced for example, by HOMs in the RF cavity) with the natural damping time, one discovers that there are, in general, some possible unstable modes [37].
Digital bunch-by-bunch feedback system installed in the modern storage rings can fight the dipole (and with some limitations also the quadrupole) coupled bunch longitudinal instabilities.
However, another "natural" damping mechanism, that can fight the single and the multi-bunch instabilities, exists: the *Landau damping*.
It works when, in a system of oscillators, there is a certain spread in the natural oscillations frequencies. This spread in the bunch is induced, in the case of longitudinal beam dynamics, by the non-linearities of the acceleration voltage.
The intuitive physical origin of this mechanism is discussed, for example, in [5]. When a periodical external force (in the case of an accelerator, as example, the force induced by a resonant mode) excites the oscillators system (the particles in the bunch)

what one expects is that the medium oscillations amplitude grows with time. By calculations, on the contrary, the whole system remains stable. This is because the stored energy is not distributed more or less uniformly in the particles but is selectively stored in particles with continuously narrowing range of frequencies around the frequency of the driving force.
These intuitive considerations can be more precisely applied to the beam dynamics [54]. Following the treatment reported in [22,55] it is possible to obtain the system of eigenvalue equations for the radial functions R_m in the form:

$$\left[\Omega_{m\mu} - m\omega(\hat{z})\right]R_m(\hat{z}) = -jI\frac{2\pi mec}{T_0}\frac{1}{\hat{z}}\frac{\partial\Psi_0}{\partial\hat{z}}\sum_{l=-\infty}^{\infty}\frac{Z\left(p_{l\mu}-\Omega_{m\mu}\right)}{p_{l\mu}-\Omega_{m\mu}}J_m\left[\frac{\left(p_{l\mu}-\Omega_{m\mu}\right)\hat{z}}{c}\right]\sigma_l\left(p_{l\mu}-\Omega_{m\mu}\right) \tag{1.96}$$

where

$$\sigma_l(\omega) = \int_0^{\infty} R_l(\hat{z})J_l\left(\frac{\omega}{c}\hat{z}\right)\hat{z}d\hat{z} \tag{1.97}$$

Considering a coherent motion driven by a narrow band resonant impedance, one obtains the following relation for Ω:

$$Z\left[-\left(N_b p+\mu\right)\omega_0 - \Omega\right] = -j\frac{\left(N_b p+\mu\right)\omega_0}{mceI}\frac{1}{G(\Omega)} \tag{1.98}$$

where $G(\Omega)$ is given by:

$$G_m(\Omega) = \int_0^{\infty}\frac{\partial\Psi_0}{\partial\hat{z}}J_m^2\left[\frac{\left(N_b p+\mu\right)\omega_0}{c}\hat{z}\right]\frac{1}{\Omega - m\omega(\hat{z})}d\hat{z} \tag{1.99}$$

The stability limit is found imposing $\mathrm{Im}(\Omega)\rightarrow 0^{-}$ and finding in the plane [Re(Z),Im(Z)] a theoretical stable region.
A typical stability diagram for the dipole mode, using the DAΦNE design parameters, is shown in Fig. 1.14 considering the non linearities induced by the RF voltage. In the same plot it is shown the stability limit if one introduces a third harmonic RF system to lengthen the bunches (see Chapter 3). The strong non-linearities induced by the harmonic voltage give a strong enhancement of the Landau damping [56].

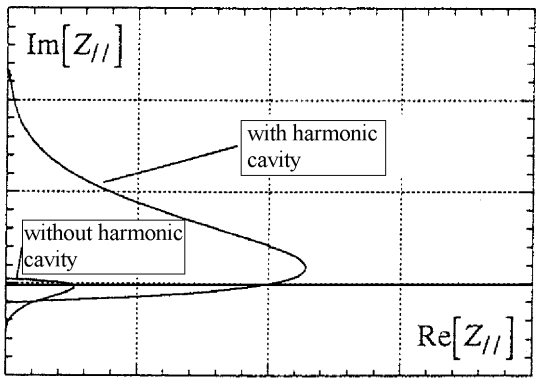

Fig 1.14: typical stability limit diagram using the DAΦNE design parameters with and without a harmonic cavity.

1.5 Beam lifetime due to Touschek scattering

The beam lifetime is usually defined as the time the beam intensity decays to a certain fraction of its initial value (half or 1/e). The effects that cause the reduction of the current in a circular accelerator can be summarized as follow [57]:

a) Effect of noise on quantum emission;
b) Scattering by residual gas in the beam pipe;
c) Multiple traversal of resonances;
d) Beam-beam effects;
e) Scattering between particles inside the bunch (Touschek scattering);

The lifetime given by all these effects is related to the final aperture available for the particle motion.

Transverse plane

Aperture limitation in the transverse plane does not necessarily mean a physical limitation but also the limitation due to the *dynamic aperture* [58]. Normally, in fact, non linear magnetic fields in the accelerator cause a limitation of the maximum transverse oscillation amplitudes. The dynamic aperture of the machine defines a certain stable region in the transverse phase space where these oscillations are stable. Also in the case of dynamic aperture limitations the particle are lost at the physical aperture, but non-linear effects blow up the transverse motion (betatron motion) and limit the “stable” initial amplitudes to values far below the *physical aperture*.

Longitudinal plane

In the longitudinal plane the particles are lost either at the RF energy acceptance limit or at the momentum acceptance of the dynamic aperture. The first effect is the limit of self focusing for the longitudinal motion described in par. 1.2. The second effect is given to the fact that for non synchronous particle (off-energy) the dynamic or physical[23] aperture can be strongly reduced if compared to the synchronous one [59].
A detailed description of the first four effects can be found, for example, in [57].
For low energy and high current machines like DAΦNE the dominant effect is the Touschek one.
Particles inside a bunch perform transverse betatron oscillations around the closed orbit. Due to a scattering effect two particles can transform their transverse momenta into longitudinal momenta. If the new longitudinal momenta of the two particles are outside the momentum acceptance of the machine[24], the particle is lost[25]. This effect was first recognized by Bruno Touschek at the ADA storage ring of Frascati [60].
The resulting beam decay rate is proportional to the number of particles in the bunch. The beam current, therefore, decays exponentially and for a gaussian particle distribution the decay time is given by [61]:

$$\frac{1}{\tau} = \frac{\sqrt{\pi} r_0^2 c N_p}{\gamma^3 \sigma'_x \, p_{acc}^2 (4\pi)^{3/2} \sigma_z \sigma_x \sigma_y} C(u_{\min}) \tag{1.100}$$

where:

r_0 is the classical electron radius[26];
c is the velocity of light;
$\gamma = E_0/m_e c^2$ is the energy of the particles in unit of rest mass (m_e is the electron mass);
N_p is the number of particles in the bunch;
σ'_x is the standard deviation of the angular divergence of the beam[27];
σ_x and σ_y are the standard deviations of the transverse dimensions;
σ_z is the bunch length;

[23] Off-energy particles perform transverse oscillation around the so-called dispersion orbit. This orbit depends on the energy deviation and is different from the on-energy (or ideal) orbit.
[24] It is the minimum between the RF momentum acceptance and the momentum acceptance due to the transverse aperture, either physical or dynamic.
[25] In principle the two particles performing synchrotron oscillations can collide head on, in such a way that they transfer their longitudinal momentum into transverse momentum. This collision process is,therefore, insignificant in particle accelerators because the longitudinal motion includes not enough momentum to increase the betatron oscillations amplitude significantly. On the other hand, transverse oscillations of particles include large momenta and a transfer into longitudinal momenta can lead to a loss of both particles.
[26] $r_0 = e^2/m_e c^2$
[27] The angular divergence of the beam and the transverse dimensions σ_x, σ_y are functions of the point s along the machine and can be determined knowing the magnet configuration of the accelerator (also called *lattice*).

$p_{acc}=\Delta p_{acc}/p_0$ is the limiting momentum acceptance of the machine. It is the minimum between the RF acceptance and the momentum acceptance due to the transverse aperture, either physical or dynamic.
$C(u_{min})$ is given by:

$$C(u_{\min}) = u_{\min} \int_{u_{\min}}^{\infty} \frac{1}{u^2}\left[\frac{u}{u_{\min}} - 1 - \frac{1}{2}\ln\left(\frac{u}{u_{\min}}\right)\right] e^{-u} du \tag{1.101}$$

with $u_{min}=(\Delta p_{acc}/\gamma\sigma'_x)^2$.

Since (as pointed out in the note 27) σ'_x, σ_x, σ_y are functions of the longitudinal point s along the ring, τ in the equation (1.100) is a function of the longitudinal position. The total lifetime is given by [59]:

$$\frac{1}{\tau} = \frac{\oint_{ring} 1/\tau(s) ds}{L_0} \tag{1.102}$$

If the energy acceptance of the machine is the RF acceptance ($\Delta p_{acc}=\Delta p_{RF}$), the Touschek lifetime can be written as:

$$\frac{1}{\tau} = \frac{\sqrt{\pi} r_0^2 c N p_0^2}{\gamma^3 \sigma_x' (4\pi)^{3/2} \sigma_x \sigma_y} \underbrace{\frac{1}{\sigma_z \Delta p_{RF}^2} C\left(\left(\frac{\Delta p_{RF}}{\gamma \sigma_x'}\right)^2\right)}_{A(V_{RF})} \tag{1.103}$$

where the quantities that depend on the RF voltage are included in the term $A(V_{RF})$.
The plot of the quantity A as a function of V_{RF} is shown in Fig. 1.18 using the DAΦNE machine parameters. An increase of the V_{RF} gives an increase of the Touschek lifetime.

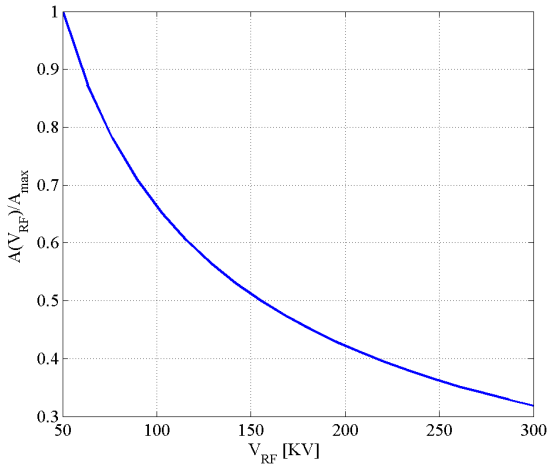

Fig 1.18: plot of the quantity $A(V_{RF})$ as a function of V_{RF} using the DAΦNE machine parameters

Appendices to Chapter 1

Appendix A1.1: Haissinski equation with the wake fields contribution

If the wake fields cannot be neglected, the total accelerating voltage is given by (see eq. (1.3)):

$$V_T(z) = V_{RF}\cos\left(\phi_s - 2\pi h\frac{z}{L_0}\right) - Q\int_{-\infty}^{\infty}\rho(z')w_z(z'-z)dz' \tag{1.A1.1}$$

Considering the linear expansion of the total accelerating voltage one obtains the following expression of the potential well:

$$\varphi(z) = \frac{1}{2}\frac{\omega_s^2}{c^2}z^2 - \frac{\alpha_c eQ}{E_0 L_0}\int_0^z dz''\int_{-\infty}^{\infty}\rho(z')w_z(z'-z'')dz' \tag{2.A1.1}$$

Inserting this expression in (1.44) one obtains the equation (1.48).

Appendix A1.2: Incoherent synchrotron frequency and synchrotron phase in the macroparticle model.

Considering that z=cτ in the equation (1.5), one obtains:

$$\left.\frac{dw_z}{dz}\right|_{\left(q-\frac{h}{N_b}+\frac{n}{N_b}\right)L_0} = j\frac{1}{2\pi c}\int_{-\infty}^{\infty}\omega Z(\omega)e^{j\omega T_0\left(q-\frac{h}{N_b}+\frac{n}{N_b}\right)}d\omega \tag{1.A1.2}$$

summing over q between -∞ and +∞ ([28]) and remembering that:

$$\sum_{q=-\infty}^{+\infty}e^{j\omega T_0 q} = \frac{2\pi}{T_0}\sum_{p=-\infty}^{+\infty}\delta\left(\omega+\frac{2\pi p}{T_0}\right) \tag{2.A1.2}$$

[28] The summation in (1.69) can be performed between -∞ and +∞ because the wake function is equal to zero for negative z.

one obtains:

$$\sum_{q=-\infty}^{+\infty} \left.\frac{dw_z}{dz}\right|_{\left(q-\frac{h}{N_b}+\frac{n}{N_b}\right)L_0} = -j\sum_{p=-\infty}^{\infty} \frac{2\pi p}{cT_0^2} Z\left(-\frac{2\pi p}{T_0}\right) e^{-j2\pi p\left(-\frac{h}{N_b}+\frac{n}{N_b}\right)} \underset{Z(-\omega)=Z(\omega)^*}{=}$$

$$= -j\sum_{p=-\infty}^{\infty} \frac{2\pi p}{cT_0^2} Z\left(\frac{2\pi p}{T_0}\right)^* e^{-j2\pi p\left(-\frac{h}{N_b}+\frac{n}{N_b}\right)} \tag{3.A1.2}$$

since:

$$\sum_{h=0}^{N_b-1} e^{j2\pi p\left(\frac{h}{N_b}\right)} = \begin{cases} 0 & \mathrm{p} \neq \mathrm{kN_b} \\ N_b & \mathrm{p} = \mathrm{kN_b} \end{cases}$$

and $e^{-j2\pi kn} = 1$, it is easy to obtain that:

$$Q\sum_{h=0}^{N_b-1}\sum_{q=-\infty}^{+\infty} \left.\frac{dw_z}{dz}\right|_{\left(q-\frac{h}{N_b}+\frac{n}{N_b}\right)L_0} = -j\sum_{k=-\infty}^{\infty} \frac{Q2\pi kN_b}{cT_0^2} Z\left(\frac{2\pi kN_b}{T_0}\right)^* =$$

$$= -j\sum_{k=0}^{\infty} \frac{Q2\pi kN_b}{cT_0^2}\left[Z\left(\frac{2\pi kN_b}{T_0}\right)^* - Z\left(\frac{2\pi kN_b}{T_0}\right)\right] = -2I\sum_{k=0}^{\infty} \frac{2\pi kN_b}{L_0} \mathrm{Im}\left[Z\left(\frac{2\pi kN_b}{T_0}\right)\right] \tag{4.A1.2}$$

similarly:

$$Q\sum_{h=0}^{N_b-1}\sum_{q=-\infty}^{+\infty} w_z\left(q-\frac{h}{N_b}+\frac{n}{N_b}\right) = 2I\sum_{k=0}^{\infty} \frac{2\pi kN_b}{L_0} \mathrm{Re}\left[Z(\omega_0 kN_b)\right] \tag{5.A1.2}$$

Appendix A1.3: System of eigenvalue equations obtained with the macroparticle model

Substituting the solution (1.71) in the equation (1.68) one obtains:

$$\left(\Omega^2 - j\frac{D}{T_0}\Omega - \omega_s^2\right) a_n = -\frac{c\alpha_c e}{E_0 T_0} Q\sum_{h=0}^{N_b-1}\sum_{q=-\infty}^{\infty} \left.\frac{dw_z}{dz}\right|_{\left(q-\frac{h}{N_b}+\frac{n}{N_b}\right)L_0} a_h e^{-j\Omega T_0\left(q-\frac{h}{N_b}+\frac{n}{N_b}\right)} \tag{1.A1.3}$$

Similarly to what done in the previous Appendix it follows that:

$$\left.\frac{dw_z}{dz}\right|_{\left(q-\frac{h}{N_b}+\frac{n}{N_b}\right)L_0} = j\frac{1}{2\pi c}\int_{-\infty}^{\infty}\omega Z(\omega)e^{j\omega T_0\left(q-\frac{h}{N_b}+\frac{n}{N_b}\right)}d\omega \tag{2.A1.3}$$

multiplying both members for $e^{-j\Omega T_0\left(q-\frac{h}{N_b}+\frac{n}{N_b}\right)}$ and summing for q=-∞,∞ one obtains:

$$\sum_{q=-\infty}^{\infty}\left.\frac{dw_z}{dz}\right|_{\left(q-\frac{h}{N_b}+\frac{n}{N_b}\right)L_0} e^{-j\Omega T_0\left(q-\frac{h}{N_b}+\frac{n}{N_b}\right)} = j\frac{1}{2\pi c}\int_{-\infty}^{\infty}\omega Z(\omega)e^{j(\omega-\Omega)T_0\left(-\frac{h}{N_b}+\frac{n}{N_b}\right)}\sum_{q=-\infty}^{\infty}e^{j(\omega-\Omega)T_0 q}d\omega \tag{3.A1.3}$$

since:

$$\sum_{q=-\infty}^{+\infty}e^{j(\omega-\Omega)T_0 q} = \frac{2\pi}{T_0}\sum_{p=-\infty}^{+\infty}\delta\left(\omega-\Omega+\frac{2\pi p}{T_0}\right) \tag{4.A1.3}$$

it follows that:

$$\sum_{q=-\infty}^{\infty}\left.\frac{dw_z}{dz}\right|_{\left(q-\frac{h}{N_b}+\frac{n}{N_b}\right)L_0} e^{-j\Omega T_0\left(q-\frac{h}{N_b}+\frac{n}{N_b}\right)} = j\frac{1}{2\pi cc}\frac{2\pi}{T_0}\sum_{p=-\infty}^{\infty}(-p\omega_0+\Omega)Z(-p\omega_0+\Omega)e^{-j2\pi p\left(-\frac{h}{N_b}+\frac{n}{N_b}\right)} =$$

$$= -j\frac{1}{L_0}\sum_{p=-\infty}^{\infty}(p\omega_0-\Omega)Z^*(p\omega_0-\Omega)e^{-j2\pi p\left(-\frac{h}{N_b}+\frac{n}{N_b}\right)} \tag{5.A1.3}$$

substituting in (1.A3) one obtains the equations (1.72)-(1.73).

Appendix A1.4: Spectrum of an oscillating train of bunches

The current of a train of oscillating bunches is given by:

$$I(t) = Q\sum_{k=-\infty}^{\infty}\sum_{h=0}^{N_b}\delta\left(t-kT_0-\frac{h}{N_b}T_0-\frac{z_{\mu h}}{c}\right) \tag{1.A1.4}$$

where:

$$z_{\mu h} = a\cos\left(\Omega_\mu t+\phi_{\mu h}\right)$$

the phases $\phi_{\mu h}$ are equal to:

$$\phi_{\mu h} = \frac{2\pi}{N_b} h\mu \tag{2.A1.4}$$

remembering that:

$$\sum_{k=-\infty}^{+\infty} \delta(u - kT_0) = \frac{1}{T_0} \sum_{q=-\infty}^{+\infty} e^{jq\omega_0 u} \tag{3.A1.4}$$

and that:

$$e^{-ja\cos(\omega t+\varphi)} = \sum_{m=-\infty}^{\infty} j^{-m} J_m(a) e^{-jm(\omega t+\varphi)} \tag{4.A1.4}$$

it follows:

$$I(t) = I \sum_{l=-\infty}^{\infty} \sum_{m=-\infty}^{\infty} j^{-m} J_m\left[(N_b l - m\mu)\frac{\omega_0 a}{c}\right] e^{j\left[(N_b l - m\mu)\omega_0 - m\Omega_\mu\right]t}$$

The Fourier transform of this signal is given by:

$$I(\omega) = I \sum_{l=-\infty}^{\infty} \sum_{m=-\infty}^{\infty} j^{-m} J_m\left[(N_b l - m\mu)\frac{\omega_0 a}{c}\right] \delta\left[(N_b l - m\mu)\omega_0 - m\Omega_\mu - \omega\right] \tag{5.A1.4}$$

if one considers small oscillation amplitudes:

$$a << \frac{L_0}{2\pi(N_b l - m\mu)} \tag{6.A1.4}$$

and remember that $J_0(x<<1) \cong 1$ $J_1(x<<1) \cong x/2$, one obtains the equation (1.77).
The equation (1.A1.4), in the case of a finite bunch length, has to be convolved with a Gaussian distribution. In the frequency domain this implies that the spectrum (1.77) has to be multiplied by the exponential form factor as shown in the equation (1.81).

Chapter 2

RF structures for linear and circular accelerators

Particles acceleration in modern circular and linear accelerators is performed by external RF generators coupled to the beam by proper e.m. structures.
These structures can be standing wave (sw) or traveling wave (tw).
In the first case the longitudinal electric field of the resonant mode in the cavity provides the correct energy kick to the bunch at each passage through the cavity.
In the second case the e.m. field travels in the structure, synchronous with the bunch and the energy gain is distributed along the device.
A huge literature on cavities and tw structures design exists depending on the accelerator applications, beam energy, kind of particles (electrons, protons, ions,…), amount of energy to provide to the beam and so on.
The intention of this chapter is to introduce the basic concepts on sw and tw structures (first two paragraphs) and the simulation codes for e.m structure design (third paragraph). The last paragraph is dedicated to describe the most common measurement techniques for normal conducting devices.

2.1 RF Cavities

A cavity is a volume of space enclosed by metallic walls, except for some holes which couple the cavity to the outer space. The resonant modes in a cavity can be obtained by solving the Maxwell equations with the proper boundary conditions at the electric walls.
The complete theory of resonant cavities is developed, for example, in [62].
The e.m. field, in a closed cavity and in the frequency domain, can be represented as a superposition of two kind of modes, the solenoidal ones and the irrotational ones, in the form:

$$\underline{E} = \sum_n a_n \underline{E}_{(sol)n} + \sum_m b_m \underline{E}_{(irr)m} \tag{2.1}$$

where the solenoidal and irrotational modes satisfy respectively the conditions:

$$\begin{cases} \nabla \times \underline{E}_{(sol)n} \neq 0 \\ \nabla \cdot \underline{E}_{(sol)n} = 0 \end{cases} \qquad \begin{cases} \nabla \times \underline{E}_{(irr)m} = 0 \\ \nabla \cdot \underline{E}_{(irr)m} \neq 0 \end{cases} \tag{2.2}$$

and $\underline{E}_p$ and $\underline{H}_p$ are the phasor of the electric and magnetic field, respectively, whose amplitudes are normalized in order to have a certain amount of energy stored in the cavity.
Different $\underline{E}_p$ (or $\underline{H}_p$) modes are, furthermore, orthogonal over the cavity volume (V), it means that:

$$\begin{cases} \int_{cavity} \underline{E}_l \cdot \underline{E}_k^* dV = 0 \\ \int_{cavity} \underline{H}_l \cdot \underline{H}_k^* dV = 0 \end{cases} \qquad l \neq k \tag{2.3}$$

If a cavity is excited by an electric current ($\underline{J}$) inside the volume, at a frequency near the resonant frequency of the n^{th} solenoidal mode[29] the phasor of the electric field is given by:

$$\underline{E}(\omega) = -\frac{1}{1 + jQ_n\left(\frac{\omega}{\omega_{rn}} - \frac{\omega_{rn}}{\omega}\right)} \frac{\underline{E}_n \int_{cavity} \underline{J} \cdot \underline{E}_n^* dV}{2P_n} \tag{2.4}$$

where ω is the frequency of the excitation $\underline{J}$, ω_{rn} is the resonant frequency of the mode and Q_n is the quality factor defined as:

$$Q_n = \omega_{rn} \frac{W_n}{P_n} \tag{2.5}$$

where P_n and W_n represent the average dissipated power on the cavity walls and the average stored energy in the cavity, they are given respectively by:

$$P_n = \frac{1}{2} \int_{\substack{cavity \\ walls}} \sqrt{\frac{\omega_{rn}\mu_c}{2\sigma_c}} \left|\underline{H}_n\right|^2 dS \tag{2.6}$$

$$W_n = \frac{1}{2} \int_{\substack{cavity \\ volume}} \varepsilon_{cav} \left|\underline{E}_n\right|^2 dV = \frac{1}{2} \int_{\substack{cavity \\ volume}} \mu_{cav} \left|\underline{H}_n\right|^2 dV \tag{2.7}$$

[29] Both the irrotational and the solenoidal modes are excited by the electric current. The resonant terms are only the solenoidal one and they give the biggest contribution to the total field in the cavity [63].

where σ_c, μ_c are the conductivity and magnetic permittivity of the cavity walls and ε_{cav}, μ_{cav} are electric and the magnetic permittivities of the material inside the cavity.

2.1.1 Beam coupling impedance of a cavity

If the cavity is excited by a charged particle beam of velocity v whose Fourier component at the frequency ω is given by[30]:

$$\tilde{I}_b(\omega) = \hat{I}_b e^{-j\frac{\omega}{v}z} \tag{2.8}$$

the excited electric field is given by[31]:

$$\underline{E}(\omega) = -\frac{1}{1 + jQ_n\left(\frac{\omega}{\omega_{rn}} - \frac{\omega_{rn}}{\omega}\right)} \frac{\underline{E}_n \hat{I}_b \int E_{nz}^* e^{-j\frac{\omega}{v}z} dz}{2P_n} \tag{2.9}$$

The complex amplitude of the effective accelerating voltage experienced by the particle is:

$$V_z = \int E_z e^{j\frac{\omega}{v}z} dz \tag{2.10}$$

By definition, the longitudinal impedance seen by the beam is then given by:

$$Z(\omega) = -\frac{V_z}{\hat{I}_b} = \frac{1}{1 + jQ_n\left(\frac{\omega}{\omega_{rn}} - \frac{\omega_{rn}}{\omega}\right)} \frac{\left|\int E_{zn} e^{j\frac{\omega}{v}z} dz\right|^2}{2P_n} = \frac{R}{1 + jQ_n\left(\frac{\omega}{\omega_{rn}} - \frac{\omega_{rn}}{\omega}\right)} \tag{2.11}$$

R is defined as the *longitudinal shunt resistance* of the cavity at its n^{th} resonant frequency and it is usually taken on the cavity axis. The equation (2.11) shows that, in the vicinity of a resonance, the cavity behaves as a parallel resonant circuit driven by the current generator representing the beam (Fig. 1.2).
The shunt resistance can be also written in the form:

[30] ω is supposed near the resonant frequency of the n^{th} solenoidal mode in the cavity.
[31] $\underline{E}$ in (2.9) depends on the transverse coordinates of the particle, which, in general, vary during the cavity traversal. For the sake of simplicity the integral is taken at fixed transverse coordinates.

$$R = \frac{\left|\int E_{zn} dz\right|^2}{2P_n} \underbrace{\frac{\left|\int E_{zn} e^{j\frac{\omega}{v}z} dz\right|^2}{\left|\int E_{zn} dz\right|^2}}_{T^2}$$

(2.12)

the quantity T is called *transit time factor* and it takes into account the fact that, due to the finite velocity of the particles, the resonant field changes its amplitude during the traversal of the cavity.
The ratio *R/Q* given by:

$$\frac{R}{Q_n} = \frac{\left|\int E_{zn} e^{j\frac{\omega}{v}z} dz\right|^2}{2W_n \omega_n}$$

(2.13)

is a quantity that depends only on the cavity geometry.
In a similar way the transverse impedance in one direction, calculated on the cavity axis, can be derived by the formula:

$$Z_\perp(\omega) = \frac{1}{k} \frac{1}{1 + jQ_n\left(\frac{\omega}{\omega_{rn}} - \frac{\omega_{rn}}{\omega}\right)} \frac{\left|\int \nabla_\perp E_{zn}\big|_{r=0} e^{j\frac{\omega}{v}z} dz\right|^2}{2P_n} = \frac{R_t}{1 + jQ_n\left(\frac{\omega}{\omega_{rn}} - \frac{\omega_{rn}}{\omega}\right)}$$

(2.14a)

R_t is the *transverse shunt resistance* of the mode.
In case of cylindrical symmetry and for the dipole modes one has (1.12) $\nabla_\perp E_{zn} \cong E_{zn}|_{r=b}/b$ where b<<transverse radius of the beam pipe. It is, therefore, possible to write:

$$Z_\perp(\omega) = \frac{c}{\omega b^2} \frac{1}{1 + jQ_n\left(\frac{\omega}{\omega_{rn}} - \frac{\omega_{rn}}{\omega}\right)} \frac{\left|\int E_{zn}(b) e^{j\frac{\omega}{v}z} dz\right|^2}{2P_n} = \frac{c}{\omega b^2} \frac{R_{1n}}{1 + jQ_n\left(\frac{\omega}{\omega_{rn}} - \frac{\omega_{rn}}{\omega}\right)}$$

(2.14b)

where the integral is performed on a path parallel to the axis of the beam pipe and at a distance b.
In general the resonant frequency of the cavity has to be properly tuned in the final constructed device in order to compensate the mechanical errors or, as seen in par. 1.3.3, in order to compensate the beam loading effects. This is, in general, done by means of metallic cylinders (*tuners*) that slightly deform the cavity volume changing its resonant frequency.

2.1.2 Coupling to cavities

The most straight-forward methods to excites resonant fields in a cavity are:

a) introduction of a conducting antenna, driven by an external RF circuit, oriented in the direction of the electric field lines of the mode to be excited;
b) introduction of a conducting loop with the plane normal to the magnetic field lines;
c) introduction of a hole or iris between the cavity and a waveguide;
d) introduction of a charged particle beam whose current lines are oriented in the direction of the electric field lines.

The last case has been discussed in the previous section where the coupling impedance and the equivalent circuit of the beam cavity interaction have been introduced.
In the first three cases, instead, in the vicinity of a resonance the whole system can be represented with an equivalent lumped element circuit as plotted in Fig. 2.1 [63].
In the circuit the elements R, L, C represent the cavity mode, the jX models the reactive effect of the modes far from resonance, the transformer of turn ratio 1:n models the coupling between the cavity mode and the waveguide (or transmission line).
The system cavity-coupler-RF source is a new resonant system with quality factor Q_L given by:

$$Q_L = \frac{\omega_r W}{\underbrace{P_{cav} + P_{ext}}_{P_T}} \tag{2.15}$$

where ω_r is the resonant frequency of the cavity, W is the average stored energy and P_T is the total average power dissipation given by the power dissipated in the walls of the cavity (P_{cav}) plus the power dissipated externally in the load Z_0 (P_{ext}).

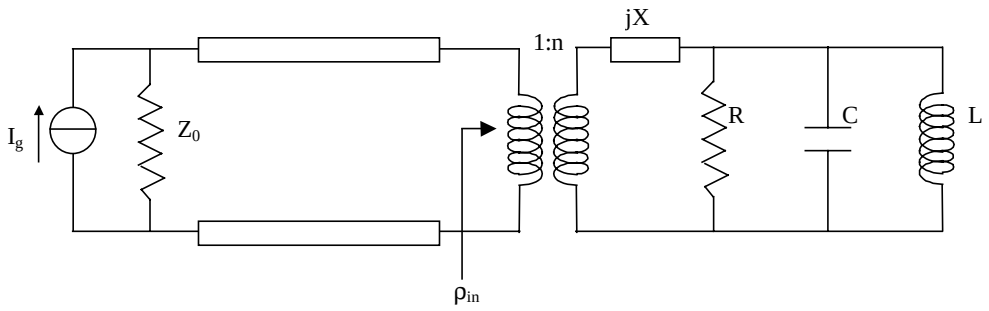

Fig 2.1: equivalent lumped element circuit of the system cavity-coupler-RF source.

Defining the *external quality factor* Q_E as:

$$Q_E = \frac{\omega_r W}{P_{ext}} \tag{2.16}$$

the *loaded quality factor* (Q_L) is given by the relation:

$$\frac{1}{Q_L} = \frac{1}{Q_0} + \frac{1}{Q_E} \tag{2.17}$$

where Q_0 is the *unloaded quality* factor.
If one defines the *coupling coefficient* β as:

$$\beta = \frac{P_{ext}}{P_{cav}} = \frac{Q_0}{Q_E} = \frac{R}{n^2 Z_0} \tag{2.18}$$

Q_L is given by:

$$Q_L = \frac{Q_0}{1+\beta} \tag{2.19}$$

With a simple calculation it is possible to find the absolute value of the reflection coefficient measured at the input port of the coupler:

$$|\rho_{in}| = \sqrt{\frac{\left(\frac{\beta-1}{\beta+1}\right)^2 + (Q_L\delta)^2}{1+(Q_L\delta)^2}} \tag{2.21}$$

Measuring $|\rho_{in}|$ as a function of frequency it is, then, possible to completely characterize the resonator in term of β, Q_0 and ω_r.
In the case of two couplers the transmission coefficient S_{21} is given by [53]:

$$S_{21} = \frac{\frac{2\beta}{1+2\beta}}{1+j\frac{Q_0\delta}{1+2\beta}} \tag{2.22}$$

By measuring the $|S_{21}|$ it is possible to completely characterize the resonant mode.
The quantity:

$$\tau = \frac{2Q_L}{\omega_0} \tag{2.23}$$

represents the time constant to reach the steady state regime when a harmonic excitation is turned on (or the time constant decay when a harmonic voltage is turned off) [64]. For that reason the quantity (2.23) is called the *filling time of the cavity*.
The design of a cavity is aimed, in general, at obtaining a certain shunt resistance (longitudinal or transverse if the cavity is used to deflect the beam) and a proper quality factor for the resonant mode of interest. Contemporary the design is aimed to minimize the shunt impedance of the higher order mode that can give rise of instabilities.
This is done by using e.m. simulation codes that allow studying the optimum shape and the coupler characteristics in order to achieve the design goals (par. 2.3).
Measurements and calibrations made on prototypes allow validating and, eventually correcting, the final dimensions of the device.

2.2 Tw structures

In a tw structure the e.m. field propagates synchronously with particles and the acceleration (or deflection) is provided continuously along the whole device.
To obtain the synchronism between the wave and the bunches, the phase velocity of the propagating e.m. field has to be equal to the particles velocity.
It is well know that, however, the phase velocity of a wave in a uniform waveguide is always larger than the speed of light so that an e.m. field propagating along a uniform guide could never be synchronous with any charged particles even if ultra-relativistic.
On the contrary, periodic structures can support waves with phase velocity much less than the velocity of light.
The generic electromagnetic properties of such type of structures can be understood looking at the *Floquet's theorem*. It states that, in a given periodic waveguide, the fields in two sections, distant D (where D is the period) are equal within a complex constant. Consequently, the field in a periodic structure is described by a solution of the form:

$$\begin{cases} \underline{E}(q_1, q_2, z) = e^{-j\beta z}\, \underline{E}_p(q_1, q_2, z) \\ \underline{H}(q_1, q_2, z) = e^{-j\beta z}\, \underline{H}_p(q_1, q_2, z) \end{cases} \tag{2.24}$$

where $\underline{E}_p$ and $\underline{H}_p$ are periodic functions of z with period D, and q_1, q_2 are the transverse coordinates in a plane normal to z.
The function $\underline{E}_p$ can be expanded into an infinite Fourier series giving the following form of the propagating field:

$$\underline{E}(q_1, q_2, z) = \sum_{n=-\infty}^{\infty} \underline{E}_{pn}(q_1, q_2)\, e^{\underbrace{-j\left(\beta + \frac{2\pi n}{D}\right)}_{\beta_n} z} \tag{2.25}$$

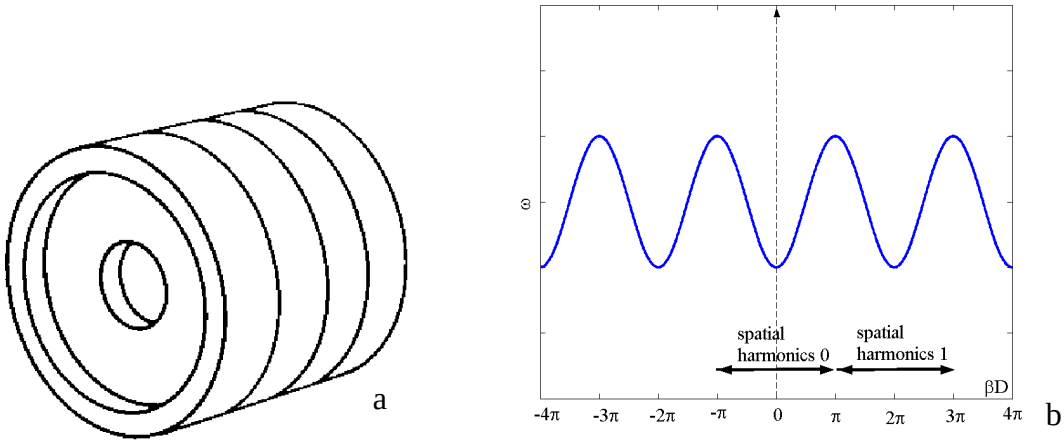

Fig 2.2: (a) typical tw accelerating structure; (b) typical dispersion curve.

Each term in the expansion is called *spatial harmonics* and has a propagating constant β_n with the following *phase* (v_{ph}) and *group velocities* (v_g):

$$\begin{cases} v_{ph} = \dfrac{\omega}{\beta_n} = \dfrac{\omega}{\beta + \dfrac{2\pi n}{D}} \\ v_g = \dfrac{d\omega}{d\beta_n} = \dfrac{d\omega}{d\beta} \end{cases} \tag{2.26}$$

The group velocity is the same for all the harmonics and represents the velocity of the power flowing in the structure [65].
Typical accelerating structures are disk loaded waveguides (Fig. 2.2a) with the dispersion curve similar to that illustrated in Fig. 2.2b. The curve is periodic in β with period $2\pi/D$ and each period is related to a spatial harmonics.
As usually happens, the zero order harmonics is synchronous with the particle beam while the other space harmonics do not perturb the motion of the beam as they pass through the bunch and produce no net effect.
The most relevant design parameters for a tw accelerating structure[32] are [66]:

a) *shunt impedance per unit length* defined as:

$$r_0 = \frac{E_{0z}^2}{dP/dz} \tag{2.27}$$

[32] Similar parameters can be defined for deflecting structures.

where E_{0z} is the amplitude of the electric field of the spatial harmonic having the same phase velocity of the bunches and *dP/dz* is the RF power dissipated per unit length. A high value of shunt impedance per unit length is desiderable since it means that a high accelerating filed can be obtained with a given expenditure of RF power per unit length.

b) the *factor of merit Q* defined as:

$$Q = \omega \frac{w}{dP/dz} \tag{2.28}$$

where w is the energy stored per unit length.

c) Ratio r_0/Q: it may be obtained from the equations (2.27-2.28):

$$\frac{r_0}{Q} = \frac{E_{0z}^2}{\omega w} \tag{2.29}$$

similarly to the standing wave cavities this parameter depend only on the geometry of the cells.

d) *Group velocity*: defined in (2.26) is another important parameter for three reasons:

1) the filling time, i.e., the time required to fill the accelerator with RF energy, depends upon the group velocity and it is given by:

$$\tau = \frac{L}{v_g} \tag{2.30}$$

where L is the device length.
A high value of the group velocity is preferred from the viewpoints of minimizing the time the RF pulse must be on.

2) The power flowing in the structure and the energy stored per unit length of the structure are related through the group velocity as follow:

$$w = \frac{P}{v_g} \tag{2.31}$$

since w is proportional to E^2_{0z} it is clear that a low value of v_g is preferred from the viewpoint of obtaining maximum accelerating fields for a given power flow.

3) In general decreasing v_g results in an increase in r_0 and r_0/Q. Therefore, a low value of v_g is preferred from the viewpoint of obtaining high values of r_0 and r_0/Q.

e) *Frequency*. Almost all the basic accelerator parameters have frequency dependence. The choice of frequency is, therefore, one of the first and most important tasks when undertaking the design of a new accelerator.
In particular, since[33]:

$$r_0 \propto \omega^{1/2} \tag{2.32}$$

from the point of view of conserving power, the operating frequency should be chosen to be as high as practicable. However, since the RF power from the available single sources drops off more rapidly with frequency than r_0 increases with frequency, it is not likely that extremely high frequencies will be advantageous. Low frequencies are preferred, moreover, because the dimensions of the structure scales as ω^{-1} and too small irises can intercept the beam. Finally, the required tolerances of fabrication are more difficult to provide for small structures.

The tw structures are fed through couplers similar to those shown in Fig. 2.3. In order to completely transmit the power from the coupler to the structure, the first cell dimensions must be properly chosen to have zero reflection coefficient at the input coupler itself.

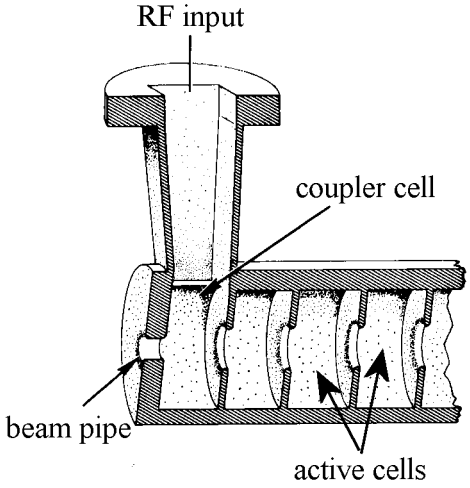

Fig 2.3: typical couplers in tw structures.

2.3 E.M. simulation codes

Optimization of the cavity shape in both the sw and tw structures is of great importance in the design procedure since for efficient operation, the shunt impedance

[33] The realtion (2.32) can be derived by simple considerations on the frequency dependence of the quantities in (2.27).

of the accelerating mode has to provide the required voltage across the structure using a minimum input power. The power dissipation and surface field distribution need to be known so that proper provision can be made for cooling the cavity and avoiding excessively high surface fields which could result in multipactoring (or quenching of supercunducting structures).
In parallel, the detailed knowledge of all the e.m. modes supported by the cavity are necessary to allow their suppression by designing dedicated damping system or by changing the characteristics of the higher order mode themselves.
For most practical cavities, however, the geometry is sufficiently complicated that analytical solutions for the electromagnetic field distributions and for the characteristics of the modes supported by the structure do not exist.
The simulations codes enable, therefore, rapid calculation and optimization of the e.m. field of RF structures with arbitrary shapes.
Numerical methods for determining e.m. fields are generally based on the discretization of the region of interest into discrete elements.
The local equations, boundary conditions and driving function for each mesh element are, then, formulated and the whole set of equations are solved simultaneously.
Different methods of volume discretization and field approximation have been developed both in the frequency and in the time domain.
MAFIA and HFSS are two of the most commonly used e.m. simulation codes.

MAFIA

The first code, MAFIA [67] (MAxwell Finite Integration Algoritm) is based on the Finite Integration Technique (FIT).
The FIT was originally developed for frequency domain applications [68,69] and was extended to static and transient field computation from the need for solving many different problems in the design of large scale accelerators [70].
The entire volume is discritized in cubic cells and the values of the E-field and H-field are considered at the edges of the cubes or at the center of the faces (Fig. 2.4).
Doing this, a double grid is considered in the discretised volume and the Maxwell's equations written in the integral form are translated into the grid space as a set of matrix equations [71] (the Maxwell's Grid Equations-MGE).
Following this approach the differential operators such as the divergence or the curl are identified with topological matrices having analytical and algebraic properties that ensure accurate numerical results and enable an algebraical self-testing of the numerical results.
The methods can be applied both in the time domain and in the frequency domain.

In the first case the solution can be performed iteratively starting from certain initial conditions and following the behavior of the field at each time step. This method can be used both for wake field and for Scattering parameters calculation[34].

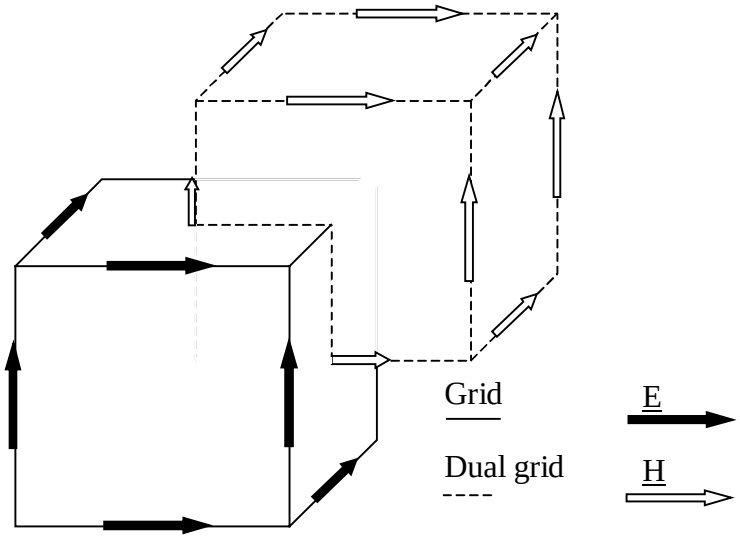

Fig. 2.4: volume discretization technique in the FIT.

In the second case it is necessary to resolve a system by the inversion of a matrix and it can be applied for eigenmodes calculations or frequency domain response. In general the numerical resolution of the system requires an amount of CPU memory that grows exponentially (or polinomially) with the number of unknowns (number of cells) while in the iterative method the memory requirement grows linearly with the number of cells.
An example of discretised sphere is shown in Fig. 2.5a.

HFSS

The second code HFSS [72] (High Frequency Structure Simulator) employs, instead, the Finite Element Method (FEM) to generate the e.m. field solution.
In the FEM technique the full problem space is divided into small regions and the field in each sub-region is represented by a local function.
In HFSS the geometry is automatically divided into a mesh of tetrahedra.
At each vertex, HFSS stores the components of the field that are tangential to the three edges of the tetrahedron itself.
In addition, the system can store the component of the vector field at the midpoint of selected edges that is tangential to a face and normal to the edge.

[34] In this second case it is enough to perform a Fourier transform of the signals in time and calculate the complex ratios between the incident and reflected (or trasmitted) waves.

The value of the vector quantities (E or H) at points inside each tetrahedron is interpolated from these nodal values.
By representing field quantities in this way, the system can transform Maxwell's equations into matrix equations that are solved using traditional numerical methods.
In this case, as in the frequency domain solver of MAFIA, the memory requirement grows exponentially (or polinomially) with the number of tetrahedra and there is, in general, a trade-off between the size of the mesh, the desired level of accuracy and the amount of available computing resources.
To produce the optimal mesh, HFSS uses an iterative process in which the mesh is automatically refined in critical regions where the variation of the field is higher (adaptive solution). When the selected S-parameters converge within a desired limit, the system breaks out of the loop.
As an example a meshed sphere is reported in Fig. 2.5b.

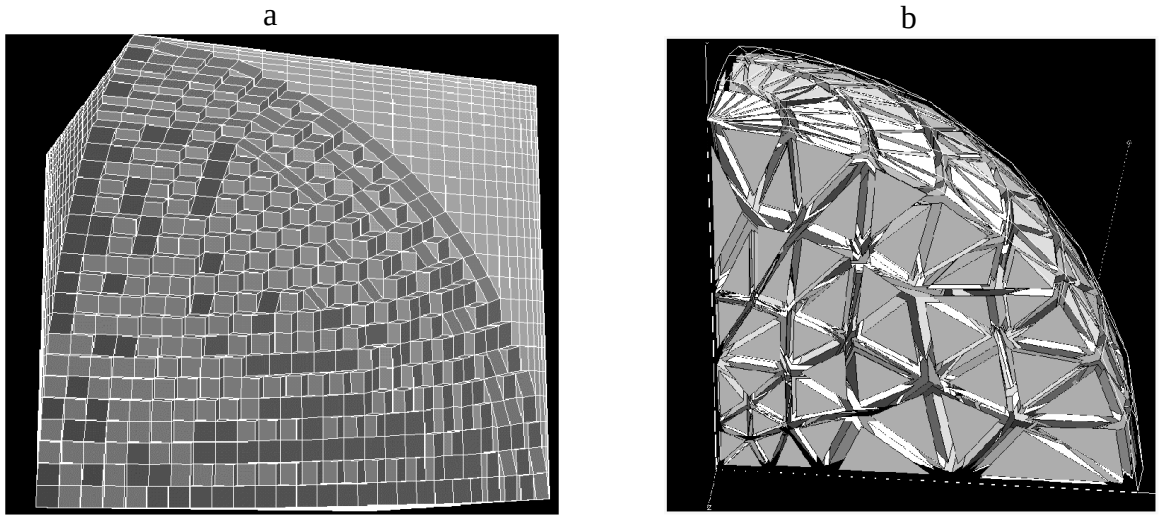

Fig 2.5: example of discretized sphere: (a) MAFIA; (b) HFSS.

2.4 Bench measurements on RF structures

The bench measurements can be performed in both the sw and tw structures and can be done using a Vector Network Analyser (VNA).

2.4.1 Resonant frequency

The resonant frequency of a sw structure can be measured by the $|S_{21}|$ (or $|S_{11}|$) from two antennas, coupled to the field (see formula 2.22 (or (2.21)).
In sw structures this measurement can be performed, for example, in order to characterize the fundamental mode and the higher order modes in a resonant cavity in terms of Q factor and frequencies.
In tw structures the resonant frequency of each cell (properly short-circuited) can be measured, before the soldering procedure, finding possible mechanical errors or imperfections. Also the dispersion curve of the whole structure can be sampled in N+2

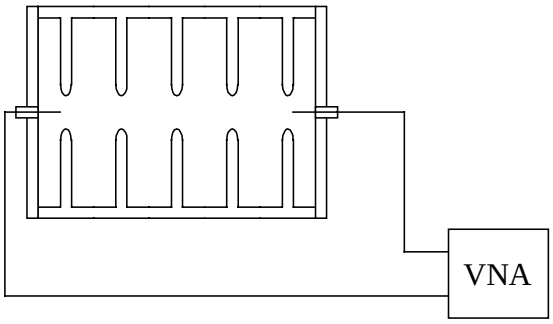

Fig 2.6: measurement set-up to sample the dispersion curve of a tw structure.

points assembling N plus 2 half cells and measuring the resonant frequency of the assemble structure as shown in Fig. 2.6.
The N cells plus 2 half cells resonate, in fact, at the N+2 angular frequencies (n=0,1,…,N+1) given by[35] [73]:

$$\omega_n = f\left(\frac{\pi}{D(N+1)}n\right) \tag{2.33}$$

where $\omega=f(\beta)$ is the dispersion function in the (β,ω) plane and D is the period.
The formula (2.33) shows that the dispersion curve of the infinite tw structure is exactly sampled in N+2 points.

2.4.2 Longitudinal and transverse beam coupling impedance

The standard way to do bench measurements of the beam coupling impedance is the coaxial wire method [74-80].
The technique assumes that:

a) a bunch of an ultra-relativistic beam has a very similar e.m. field distribution to a short pulse on a coaxial line [1];
b) the coupling impedance seen by the beam is equal to the impedance seen by the TEM mode in the coaxial waveguide.

The sketch of the measurement setup and the equivalent circuit are shown in Fig. 2.7. In the figure the networks A and B allow to match the characteristic impedance of the VNA (usually 50 Ohm) with the characteristic impedance of the coaxial waveguide (Z_c).
The matching can be realized, in general, with a resistive network Fig. 2.8a or with tapers Fig. 2.8b. Due to parasitic effects (inductance and capacitor) in the resistors, the

[35] These frequencies can be simply obtained considering a sum of a forward ($e^{-j\beta(\omega)z}$) and reflected ($e^{j\beta(\omega)z}$) wave and imposing the boundary conditions at z=0 and z=L.

first method is adopted in the case of low frequency impedance measurements (usually up to 1-2 GHz) while the second method allows measuring impedances at high frequencies depending on the ratio between the taper length and the initial and final diameters.
The exact relation between the measured S-parameter, S_{21DUT} ([36]), and the unknown impedance Z is given by:

$$Z = 2Z_c \frac{1 - S_{21}}{S_{21}} \tag{2.34}$$

where Z_c is the characteristic impedance of the coaxial waveguide.
In practical bench measurements the measured S_{21DUT} is compared with a reference S_{21REF} that is obtained measuring the S-parameter of a coaxial waveguide without the DUT ([37]):

$$Z = 2Z_c \frac{1 - \frac{S_{21DUT}}{S_{21REF}}}{\frac{S_{21DUT}}{S_{21REF}}} \tag{2.35}$$

This normalization procedure can be useful if the matching network introduces some errors in the measurement itself.
The characteristic of the e.m. field are perturbed by the presence of the wire. First of all the wire lowers the Q of high Q DUTs like cavities and usually detunes the resonance frequency. The wire, moreover, changes the boundary conditions of the whole structure and permits exchange of e.m. energy between the DUT and the VNA for frequencies below the waveguide cut-off.

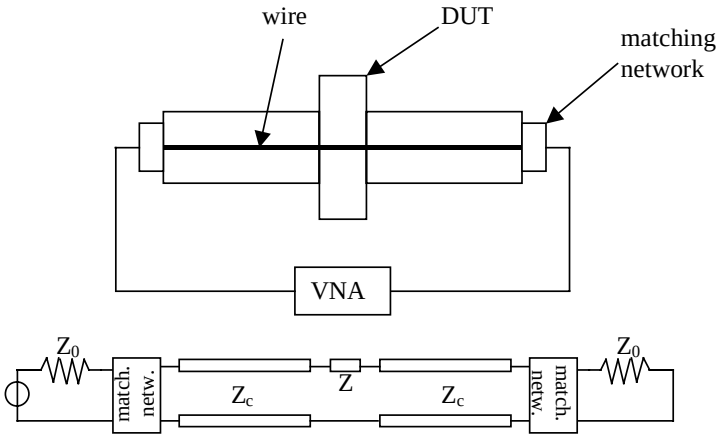

Fig 2.7: sketch of the wire method used to measure the beam longitudinal coupling impedance.

[36] DUT-Device Under Test.
[37] The formula is known as the Hahn-Pedersen formula.

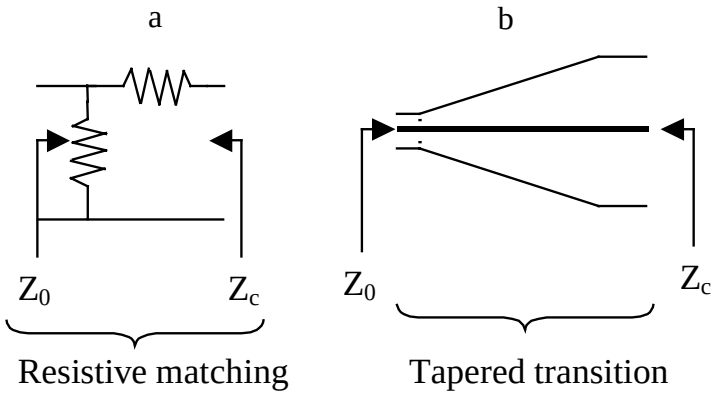

Fig 2.8: typical matching networks.

Experimentally, however, comparing the measured R/Q of know resonant structures with that obtained by analytical or numerical calculations, one obtains errors of few percent if the length of the cavity is small compared with the beam-pipe diameter and the wire radius is much smaller than the beam pipe radius.
Unfortunately, a general analytical theory that allows validating the method does not exist and the way to proceed is to simultaneously compare the measurements results with other type of measurements (as those illustrated in par. 2.4.4) or simulations [53,81].
The method can be also applied in order to evaluate transverse impedances.
The standard technique is to stretch two parallel wires across the DUT. The two wires can support both an odd and an even mode and for the transverse impedance measurement only the first has to be excited. For this purpose one uses a 180° hybrid transition that excites the odd mode and suppresses the even one.
In this case the formula to evaluate the transverse impedance is simply given by [82]:

$$Z = \frac{c}{\omega b^2} Z_{c(odd)} \frac{1 - \frac{S_{21DUT}}{S_{21REF}}}{\frac{S_{21DUT}}{S_{21REF}}} \tag{2.36}$$

where b is the distance between the wires and $Z_{c(odd)}$ is the characteristic impedance of the odd mode. The formula is directly derived from the eq. (1.15) that relates the longitudinal and the transverse impedance of a transverse mode.
Similar considerations, than in the longitudinal case, can be done on the validity of the method.

2.4.3 Beam transfer impedance

The beam transfer impedance is defined as a ratio between the voltage signal $V_{dev}(\omega)$ detected trough a device coupled to the beam and the Fourier series component $\tilde{I}(\omega)$ of the beam:

$$Z_{transf}(\omega) = \frac{V_{dev}(\omega)}{\tilde{I}(\omega)} \tag{2.37}$$

Following considerations similar to those done in the previous paragraph, the beam current can be substituted with the current flowing on a wire (Fig. 2.9a).
Referring to the circuit shown in Fig. 2.9b, if the perturbation induced by the device coupled to the beam is negligible ($|S_{12dev}| \cong 1 \Leftrightarrow |S_{11dev}| \cong 0$) and the reflection coefficients of the matching network are almost equal to zero, the absolute value of the transfer impedance can be easily evaluated measuring the scattering parameters S_{31TOT} and S_{21TOT} and applying the formula (Appendix A2.1):

$$\left|Z_{transf}(\omega)\right| = \frac{\left|S_{31TOT}\right|}{\sqrt{\left|S_{21TOT}\right|}} \sqrt{Z_c Z_0} \tag{2.38}$$

where Z_c is the characteristic impedance of the coaxial waveguide and Z_0 is the characteristic impedance of the network analyzer.

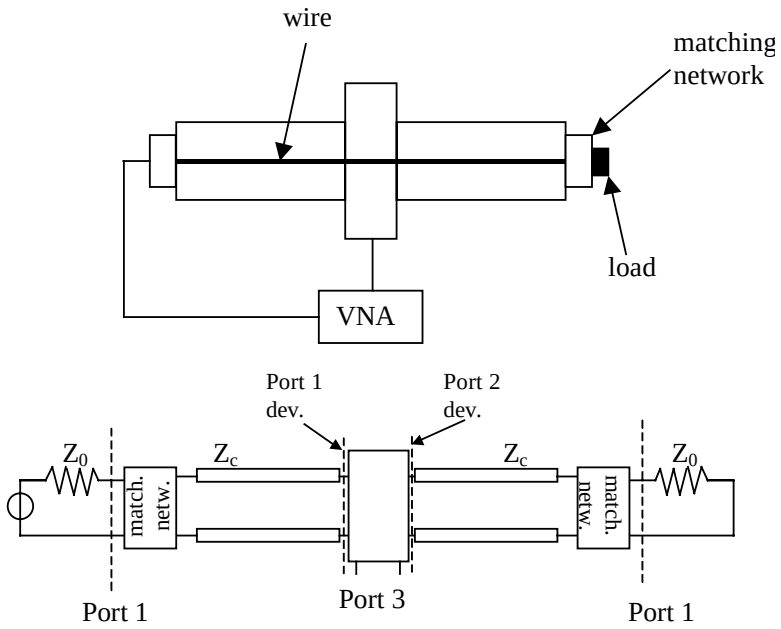

Fig 2.9: (a) sketch of the beam transfer impedance measurement setup;
(b) equivalent circuit.

2.4.4 Field mapping by perturbation method

The field in the cavity can be sampled by introducing a perturbing object along the beam pipe and observing the change in resonant frequency [83,84]. Fig. 2.10 shows the typical set up for the measurement.
For the case of a small sphere of radius r, if the unperturbed field may be considered uniform over a region larger than the bead, the relative frequency variation is given by:

$$\frac{\Delta\omega_r}{\omega_r} = -\frac{\pi r^3}{W}\left(\varepsilon_0 \frac{\varepsilon_r - 1}{\varepsilon_r + 1} E_0^2 + \mu_0 \frac{\mu_r - 1}{\mu_r + 1} H_0^2\right) \tag{2.39}$$

where W is the total stored energy in the cavity and E_0, H_0 are the fields at the bead position.
For a dielectric (μ_r=1) or metal ($\mu_r \to 0$, $\varepsilon_r \to \infty$) bead the equation (2.39) becomes:

$$\frac{\Delta\omega_r}{\omega_r} = -\frac{\pi r^3}{W}\left(\varepsilon_0 \frac{\varepsilon_r - 1}{\varepsilon_r + 1} E_0^2\right)$$
$$\frac{\Delta\omega_r}{\omega_r} = -\frac{\pi r^3}{W}\left(\mu_0 \frac{\mu_r - 1}{\mu_r + 1} H_0^2\right) \tag{2.40}$$

Shaped beads such as needles or disks can be used to enhance the perturbation and give directional sensitivity [84].
To determine the direction of the field components is particularly important when dealing with the higher modes of a complex cavity shape where the measured mode frequency will not be a sure identifier of the dominant field direction.
By a map of the longitudinal electric field it is possible to calculate the longitudinal and transverse coupling impedances with the formulae (2.12)-(2.14).

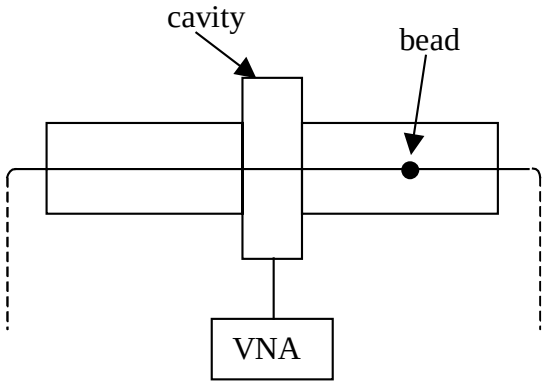

Fig 2.10: sketch of the bead pull measurement set-up.

2.4.5 Phase advance per cell for tw structures

In the case of tw structures, the process of tuning is intended to adjust the phase advance of every cell to the design since random and systematic errors can remain after the device machining and fabrication.
Random errors are usually corrected by deformation of the cell walls or by the use of tuning plugs. Systematic errors, instead, can be corrected by adjustment of the operating temperature or driving frequency[38].
Contemporary, the matching of the input coupler is done by adjusting the dimensions of the coupler cell to insure a low reflection coefficient at the input and output of the structure.
The problem is that the two processes are not independent.
The schematic measurement set-up for the cells tuning procedure is shown in Fig. 2.11. The dephasing per cell is measured by using a movable plunger in order to reflect the traveling wave. By measuring the phase of the reflection coefficient at the input coupler as a function of the short position it is possible to determine whether the n^{th} cell is correctly tuned.
The difficulty is that, if the coupler cell is not well matched, the phase of the reflection coefficient depends on the internal coupler reflections and it is not possible to distinguish the two effects.
By changing the e.m. properties of the coupler with the matching section it is possible to cancel this uncertainty and to correctly tune the cells. Different ideas have been explored for this purpose [66]. The basic strategy is to use Smith chart plots of the reflection coefficient as a function of different plunger positions and to correct the mismatch of the coupler by changing the reactive matching section in order to cancel these reflection contributions.

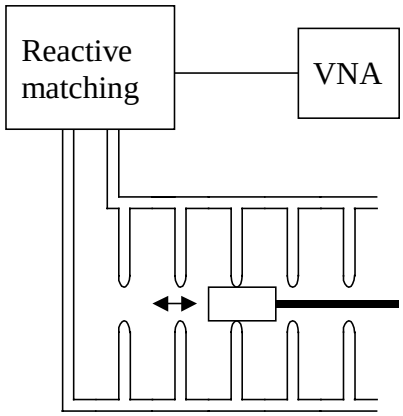

Fig 2.11: sketch of the phase advance per cell measurement set-up.

[38] The first method allows changing slightly the dispersion curve of the structure while the second method the operating mode.

Appendices to Chapter 2

Appendix A2.1: Beam transfer impedance calculation

The circuit of Fig. 2.9 is reported more in detail in Fig. 1.A2.1 where the line impedances have been put equal to 1 (this is always possible re-defining the currents and voltages [65]).
Supposing that the perturbation induced by the device is negligible it follows that $a_2' \cong b_1'$ and that $b_2' \cong a_1'$ and that the device can be substituted with a transmission line of negligible length.
The total incident and reflected waves at the ports 1 and 2 can be found considering the superposition of two different excitations as shown in Fig, 2.A2.1.
In the case of "odd" and "even" excitation one obtains respectively:

$$\begin{cases} a_{1o} = \dfrac{V}{4} \\ b_{1o} = \left(S_{11} - \dfrac{S_{12}^2 e^{-j\alpha}}{1 - S_{22} e^{-j\alpha}} \right) \dfrac{V}{4} \\ a_{1o}'' = -\dfrac{V}{4} \\ b_{1o}'' = -\left(S_{11} - \dfrac{S_{12}^2 e^{-j\alpha}}{1 - S_{22} e^{-j\alpha}} \right) \dfrac{V}{4} \\ a_{2o} = -\dfrac{S_{12} e^{-j\alpha}}{1 + S_{22} e^{-j\alpha}} \dfrac{V}{4} \\ b_{2o} = \dfrac{S_{12}}{1 + S_{22} e^{-j\alpha}} \dfrac{V}{4} \end{cases} \qquad \begin{cases} a_{1e} = \dfrac{V}{4} \\ b_{1e} = \left(S_{11} + \dfrac{S_{12}^2 e^{-j\alpha}}{1 - S_{22} e^{-j\alpha}} \right) \dfrac{V}{4} \\ a_{1e}'' = \dfrac{V}{4} \\ b_{1e}'' = \left(S_{11} + \dfrac{S_{12}^2 e^{-j\alpha}}{1 - S_{22} e^{-j\alpha}} \right) \dfrac{V}{4} \\ a_{2e} = \dfrac{S_{12} e^{-j\alpha}}{1 - S_{22} e^{-j\alpha}} \dfrac{V}{4} \\ b_{2e} = \dfrac{S_{12}}{1 - S_{22} e^{-j\alpha}} \dfrac{V}{4} \end{cases} \tag{1.A2.1}$$

where $\alpha = \beta L$ and $|S_{ij}|$ is the scattering matrix of the matching networks.
The total incident and reflected waves are given by:

$$\begin{cases} a_1 = \dfrac{V}{2} \\ b_1 = \left(S_{11} + \dfrac{S_{22} S_{12}^2 e^{-j2\alpha}}{1 - S_{22}^2 e^{-j2\alpha}} \right) \dfrac{V}{2} \\ a_1'' = 0 \\ b_1'' = \dfrac{S_{12}^2 e^{-j\alpha}}{1 - S_{22}^2 e^{-j2\alpha}} \dfrac{V}{2} \\ a_2 = \dfrac{S_{12} S_{22} e^{-j2\alpha}}{1 - S_{22}^2 e^{-j2\alpha}} \dfrac{V}{2} \\ b_2 = \dfrac{S_{12}}{1 - S_{22}^2 e^{-j2\alpha}} \dfrac{V}{2} \end{cases} \tag{2.A2.1}$$

The total reflection coefficient at the input port 1 is then given by:

$$S_{11TOT} = \frac{b_1}{a_1} = S_{11} + \frac{S_{12}^2 S_{22} e^{-j2\alpha}}{1 - S_{22}^2 e^{-j2\alpha}} \tag{3.A2.1}$$

and the total transmission coefficient between the port 1 and 2 is given by

$$S_{21TOT} = \frac{b_1''}{a_1} = \frac{S_{12}^2 e^{-j\alpha}}{1 - S_{22}^2 e^{-j2\alpha}} \tag{4.A2.1}$$

The ratio between the incident wave at the input port 1 and the traveling wave in the coaxial waveguide is given by:

$$\frac{b_2}{a_1} = \frac{S_{12}}{1 - S_{22}^2 e^{-j2\alpha}} \tag{5.A2.1}$$

Considering the equations (4.A2.1) and (5.A2.1), if $|S_{22}|^2 \cong 0$ the ratio between the power incident at the port 1 and the power flowing in the coaxial waveguide is given by:

$$\frac{P_{coax}}{P_{inc}} \cong \left| S_{12} \right|^2 \cong \left| S_{12TOT} \right| \tag{6.A2.1}$$

If S_{31TOT} is the total transmission coefficient between the input port 1 and the port 3 it follows that:

$$\frac{P_3}{P_{inc}} = \left| S_{13TOT} \right|^2 \Rightarrow \frac{P_3}{P_{coax} / \left| S_{12TOT} \right|} = \left| S_{13TOT} \right|^2 \Rightarrow \frac{1}{2} \frac{\left| \tilde{V}_{dev} \right|^2}{Z_0} = \frac{\left| S_{13TOT} \right|^2}{\left| S_{12TOT} \right|} \frac{1}{2} Z_c \left| \tilde{I} \right|^2 \tag{7.A2.1}$$

from this expression it follows directly the equation (2.38)

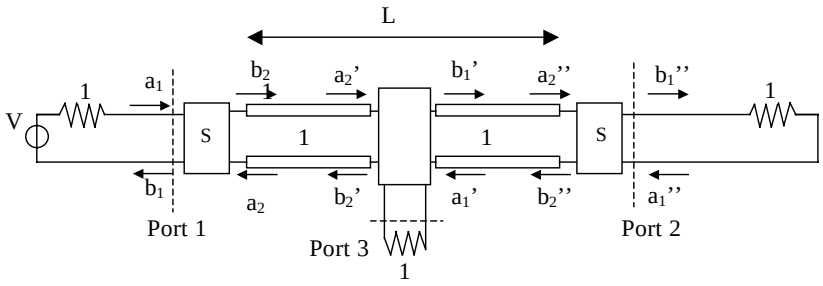

Fig. 1.A2.1

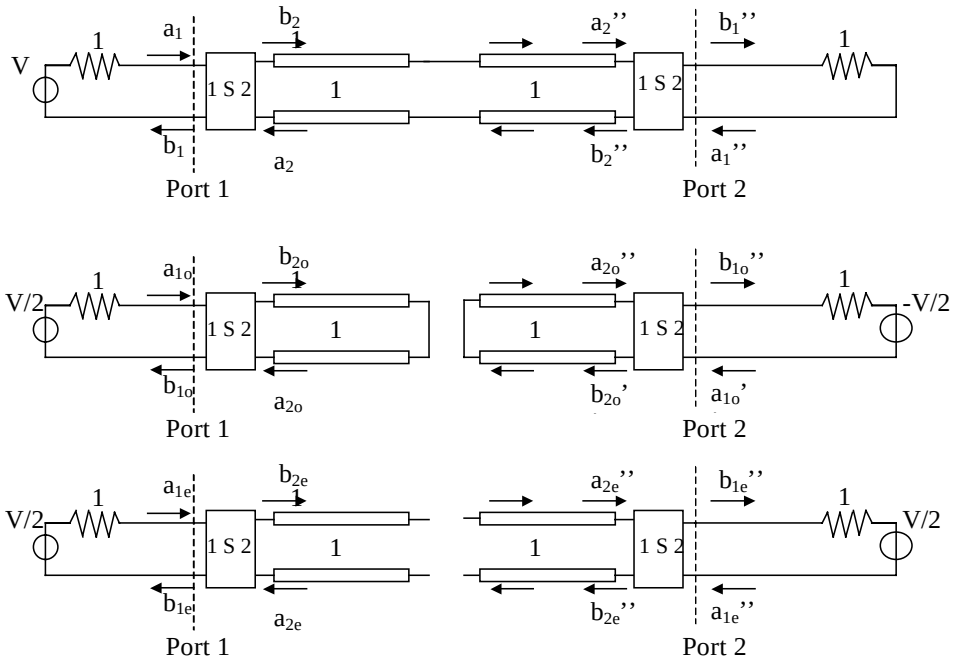

Fig. 2.A2.1

Chapter 3

Control of bunch length with a high harmonic cavity in DAΦNE

The Frascati Φ-factory DAΦNE is a double ring, high luminosity collider working at the energy of the Φ meson resonance (1.02 GeV in the center of mass).
The sketch of the factory is shown in Fig. 3.1. In the two rings electrons and positrons travel in opposite directions and collide in the two interaction points IP1 and IP2.
The most relevant DAΦNE design and present parameters are summarized in Tables 1.1-3.1.
The study and the design of a high harmonic RF system is mainly motivated by the demand of lifetime improvement for storage rings with lifetime limited by the Touschek effect such as low energy machines. In such case, the implementation of the hardware providing an RF harmonic extra-voltage to the beam is aimed at reducing the RF slope at the bunch center to lengthen it and to maintain, contemporary, a high energy acceptance.
There is also another reason for tacking into consideration RF harmonic systems. The non-linearities introduced by the harmonic voltage tend to weaken the possible coherent instabilities through the Landau damping mechanism (par. 1.4) and may be therefore beneficial for both the single and the coupled-bunch beam dynamics [56, 85].
However, the introduction of a harmonic cavity also perturbs other aspects of the longitudinal dynamics affecting the overall machine performances.
The first paragraph of this chapter is dedicated to the study of the beam dynamics with the RF harmonic system in the lengthening regime. It includes both the multi and the single bunch effects and the lifetime calculations.
In the second paragraph the harmonic cavity design is discussed while the last paragraph is dedicated to illustrate and discuss the measurement results.

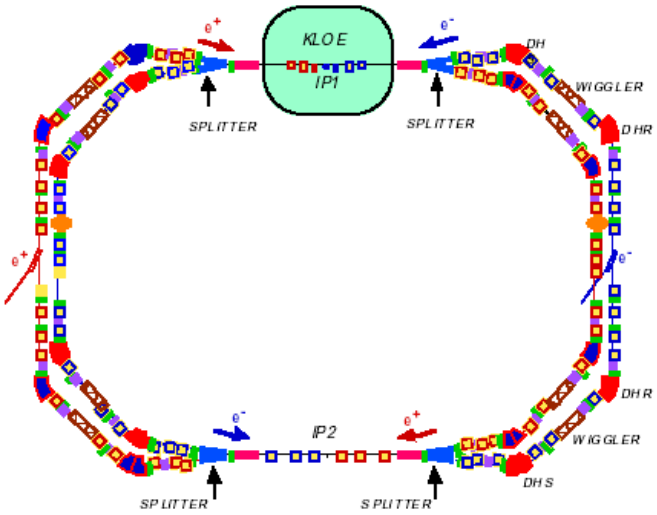

Fig 3.1: sketch of the Frascati Φ-factory DAΦNE.

3.1 Beam dynamics in DAΦNE with the harmonic cavity

The Touschek effect is especially harmful in DAΦNE because of the low beam energy and high bunch charge density necessary to get the required luminosity per bunch (par. 1.5). The effect results in production of beam induced background in the detector [86] and in the necessity of frequent beam injections due to low beam lifetime [87].
The situation should be improved using a harmonic RF system [88].
It consists in the addition of a second RF voltage to the main one at the frequency nf_{RF} in order to reduce the RF slope at the bunch center. Doing this it is also possible to increase the main RF voltage maintaining an acceptable value of the bunch length. The combined effects of the lengthened bunch and the increase of the energy acceptance increase the lifetime of the machine.
In the case of DAΦNE n has been chosen equal to 3 after a complete investigation over various possible harmonics as a good trade-off between efficiency and compactness requirements.
The required harmonic voltage can be obtained by powering the cavity with an external RF source (active option) or by letting the beam current interact with the harmonic cavity fundamental mode impedance (passive option[39]).
In the case of the DAΦNE rings the passive option has been chosen since it is far less complicated and expensive compared with the active one and since a very moderate harmonic voltage is required to obtain a reasonable bunch length. Furthermore it does not present major drawbacks from the beam dynamics point of view and the quite high stored multi-bunch current in operation allows sustaining the required harmonic voltage without difficulties.

[39] In this case the required power to sustain the harmonic voltage is given by the RF main system through the beam.

Table 3.1: present DAΦNE operation parameters

Energy (E_0)	510 [MeV]
RF frequency (f_{RF})	368.29 [MHz]
Harmonic number (h)	120
Revolution frequency (f_0)	3.0688 [MHz]
Momentum compaction (α_c)	0.025÷0.035
Max. beam current (I_{max})	~1.3 [A]
Number of colliding bunches (N_b)	47÷51 over 60 or 100÷105 over 120 ([40])
Max. current per bunch (I_{bmax})	~26 [mA] with 47-51 bunches over 60 ~13 [mA] with 100-105 bunches over 120
RF voltage (V_{RF})	100÷120 [KV]
Bunch spacing (T_b)	5.43 [ns] (=2/f_{RF}) with 47-51 bunches over 60 2.71 [ns] (=1/f_{RF}) with 100-105 bunches over 120
Synchrotron losses (U_0)	9.3 [KeV/turn]
Impedance losses (U_{imp})	~2.5 [KeV/turn] (I_b≅20mA, e^- ring) ~4.5 [KeV/turn] (I_b≅20mA, e^+ ring)
Natural bunch length (σ_{z0})	1.4÷1.6 [cm] (V_{RF}=120KV)
Bunch length (σ_z)	~2.4 [cm] (e^+ and I_b≅20mA, V_{RF}≅120KV) ~2.8 [cm] (e^- and I_b≅20mA, V_{RF}≅120KV)
Vertical β-function at the IP (β^*_y)	~3 [cm]
RF acceptance (ε_{RF}/E0)	~0.55% (with V_{RF}≅120KV)
Beam lifetime (τ)	~1000÷2000 [s]

As pointed out in par. 1.2.4 the bunch length in DAΦNE depends on the bunch current and the lengthening process due to the wake fields can be well simulated by the single bunch tracking code.

[40] The first option has been adopted for the collisions in the first interaction point with the experiment KLOE [87], while the second one for the collisions in the second interaction point with the experiment DEAR. When the bunches collide in one interaction point they are vertically separated in the other region.

The present DAΦNE operation parameters are summarized in Table 3.1. The RF voltage is equal to ≈120 KV and the bunch length at typical operating conditions is 2.4 cm and 2.8 cm in the e^+ and e^- ring, respectively[41].
In the future the current per bunch could increase from 20-25 mA to 30-35 mA, in order to increase the machine luminosity (see note 43). Single bunch measurements already performed on the two rings at the present operational RF voltage show that the bunch length at 35 mA is about 2.8 and 3.3 cm in the e^+ and e^- ring respectively [89]. These values are already at the limit allowed by the present value of the vertical β-function at the interaction point. This means that, with the present machine set-up, there is no chance of lengthening further the bunch without affecting the machine luminosity[42].
The only possible strategy to improve the lifetime using a harmonic voltage is based, therefore, on the RF acceptance increase, which can be obtained increasing the peak voltage of the main RF system. In this case the harmonic voltage is used to reduce the total RF slope at the bunch center in order to keep the bunch length near the hourglass limit.
The choice of the harmonic frequency and of the harmonic system parameters has been aimed to match the previous considerations and to satisfy the beam dynamics requirements (as discussed in the following). After a complete investigation over the 2nd the 3rd and the 4th harmonic frequencies the 3rd harmonic has been chosen as the working frequency of the DAΦNE harmonic cavity as a good trade-off between efficiency and compactness requirements.
The DAΦNE 3rd harmonic system parameters are reported in Table 3.2 ([43]).
The cavity has to be considered as a resonant impedance powered by the beam $3f_{RF}$ spectrum line. The shunt impedance of the cavity has been chosen quite low (R_H=480 KΩ) in order to weaken the coherent effects induced by the beam. On the other hand, this will ask for some extra power to the main RF system that is not an issue in the DAΦNE case[44].

---

[41] The difference in the e^- ring is due to the higer broad-band impedance because of the presence of the ion clearing electrodes. The model of the DAΦNE short range wake field does not includes, for the moment, this contribution to the wake and, therefore, predicts with good accuracy the lengthening of the e^+ ring.

[42] The luminosity of a collider is the number of reaction events produced per unit reaction cross section. The most simple formula that gives the luminosity of a collider is [90]:

$$L = N_b f_0 \frac{N_p^+ N_p^-}{4\pi\sigma_x^*\sigma_y^*}$$

where $N_p^{\pm}$ is the number of particles per bunch for each beam, N_b is the number of bunches in each beam, f_0 is the revolution frequency, σ^*_x and σ^*_y are the r.m.s transverse dimensions of the beam at the interaction point. The transverse dimensions of the beam near the collision point (s=0) are given by the equation:

$$\sigma(s) \propto \beta^* + \frac{s^2}{\beta^*}$$

where the β-function at the IP β^* is related to the magnet configuration of the machine. In order not to loose luminosity due to of the so-called hourglass effect [91] the bunch length has to be less than β^*.

[43] The parameters Q_{0H} and R_H related to the harmonic cavity are those of the constructed device (par. 3.2).

[44] The average power dissipated in the harmonic cavity is $P_H=V_{RFH}^2/2R_H$. A lower R_H gives more dissipation.

Table 3.2: DAΦNE 3rd harmonic system parameters

Main RF voltage (V_{RF})	200 [KV]
Main cavity shunt impedance (R)	1.9 [MΩ]
Main cavity Q-factor (Q_0)	31500
Main cavity input coupling factor (β)	~4.6
Detuning of the main cavity at I=0 ($Q_L\delta_0$)	1.2
RF harmonic frequency (f_{RFH}=3 f_{RF})	1104.87 [MHz]
RF harmonic voltage (V_{RFH})	56 [KV]
Harmonic cavity shunt impedance (R_H)	0.48 [MΩ]
Harmonic cavity Q-factor (Q_{0H})	18500
Natural bunch length (σ_{z0})	~2.5 [cm]
Bunch length in the lengthening regime (σ_z)	~2.9 [cm] with I_b=17 mA ~3.1 [cm] with I_b=34 mA
Momentum compaction (α_c)	0.034
RF acceptance ε_{RF}/E_0	~0.7%

In order to get the required voltage with the proper phase at any operation value of the beam current, the harmonic cavity has to be properly tuned between the revolution harmonics $3h\omega_0$ and $(3h+1)\omega_0$. Referring to the equivalent circuit of the beam cavity interaction (Fig. 1.2), the cavity detuning is given by the following equation:

$$Q_{0H}\delta_H = -\sqrt{\left(\frac{\left|\tilde{I}_{3h}\right|R_H}{\left|V_{RFH}\right|}\right)^2 - 1} \tag{3.1}$$

where $\tilde{I}_{3h}$ is the 3h line of the beam Fourier series (eq. (1.83)), and $\delta_H=3h\omega_0/\omega_{RFH}-\omega_{RFH}/3h\omega_0$.

Tuning the cavity above the 3*h* revolution harmonic provides the right phasing with respect to the main RF voltage to lengthen the bunches. In fact, considering the harmonic voltage equal to 56 KV, and a typical operating current I=1 A, the absolute value of the $Q_{0H}\delta_H$ is larger than 10, this mean that the impedance of the harmonic

cavity sampled at the 3rd harmonic frequency is mainly imaginary and produces a harmonic voltage that is almost completely out of phase with respect to the beam.
A plot of the main and harmonic voltages and their sum, together with the resulting potential well is shown in Fig. 3.2 at I=1.6 A.

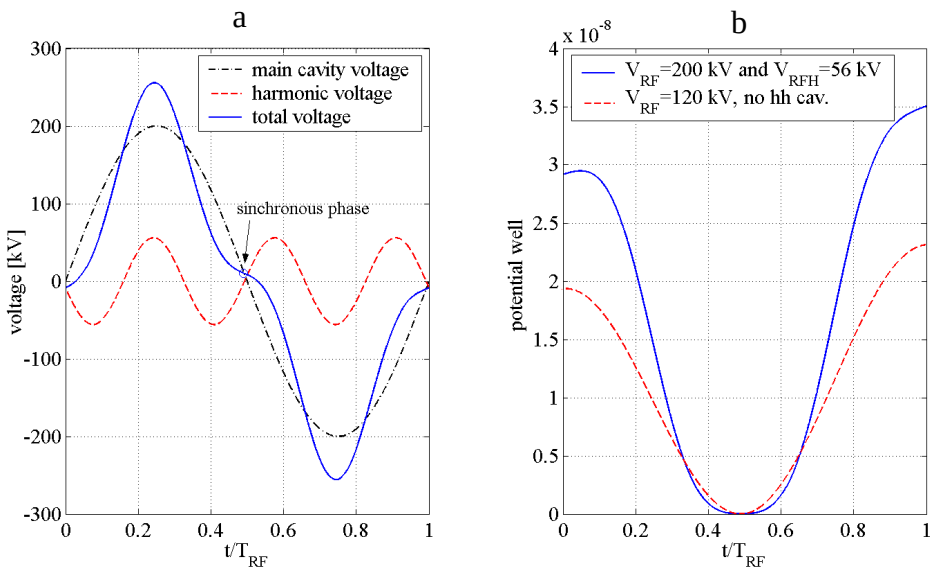

Fig 3.2: (a) main and harmonic voltages; (b) resulting potential well.

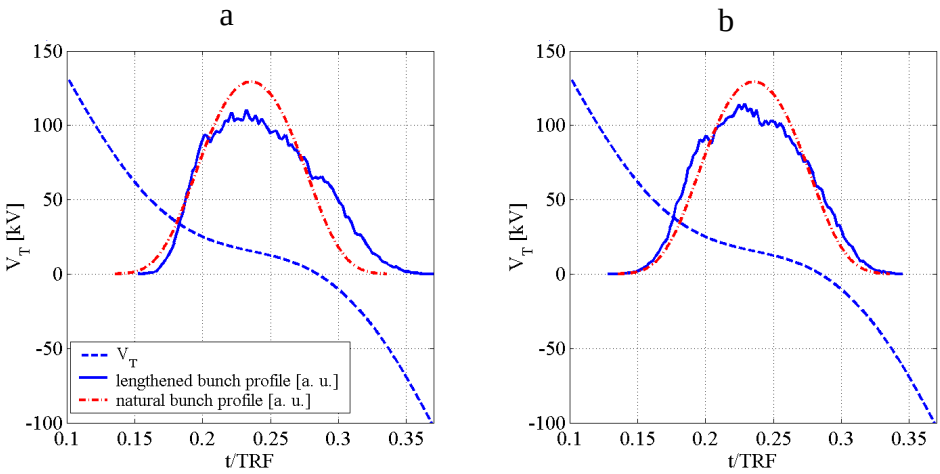

Fig 3.3: natural and lengthened bunch profile with the harmonic cavity (a-34 mA/bunch, b-17 mA/bunch),

The natural bunch profile with this cavity detuning, as given by the Haissinski equation, is plotted in Fig. 3.3 with the lengthened profile obtained by the single bunch simulation code at two different bunch current: 17 mA and 34 mA.
This RF working point should provide, therefore, a bunch length close to the hourglass limit, with an RF acceptance 30% higher with respect to the present DAFNE operating conditions. In addition, since the harmonic voltage makes the natural bunch length larger, the lengthening process is less pronounced, which indicates that microwave effect and single bunch dynamics are relaxed (par. 1.2.3-4).

3.1.1 Analysis of the coupled bunch instabilities in case of uniform filling pattern

Considering N_b equidistant bunches, the coherent angular synchrotron frequencies and the growth rates of the μ-mode are given by the equations (1.76)-(1.79) using a macroparticle model with or without considering the bunch length and by (1.82) using the perturbative theory.
The incoherent synchrotron angular frequency ω_s is, in the case of eq. (1.76)-(1.82), the frequency of the small amplitude oscillations, while in (1.79) it is the average frequency oscillation amplitude over the bunch length (1.80).
In principle, the formulae (1.76)-(1.79) can be applied also in the limit of $\omega_{c\mu} \to 0$ ([45]). Moreover eq. (1.82) is valid only for small perturbations of the unperturbed Haissinski profile even if it takes into account the whole distribution function instead of a rigid bunch profile.
The calculation of the "real" coherent frequency shift in the case of strong perturbations and in the presence of non-linearities in the total RF slope (as in the case of the harmonic cavity) is an open problem.
A multi-particle multi-bunch tracking code could give a possible solution to the whole problem but, in this case, the parameters of the system have to be found tentatively and the physical phenomenology can be definitively lost. Eventually, in a further study, such a code can be used for the optimization of the working point obtained by the analysis of the beam dynamics with the approximated analytical equations.
Considering only the contribution of the main and harmonic cavities the most affected coupled bunch modes are the modes "0", "1", and "N_b-1" with sidebands close to the resonant frequencies of the main and harmonic cavity impedances (Fig. 3.4).

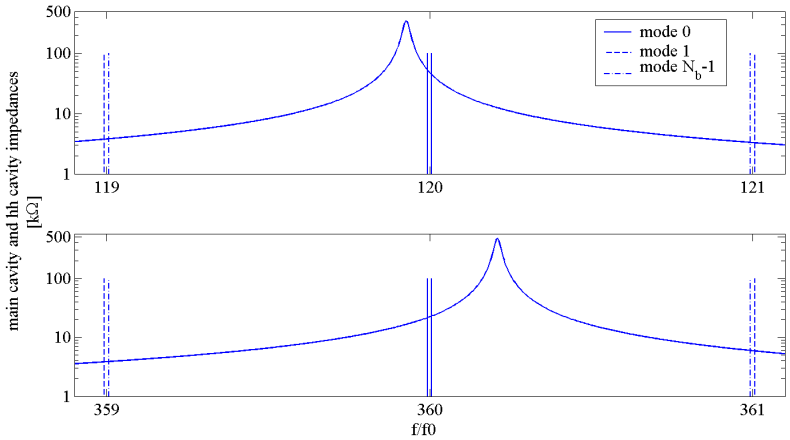

Fig 3.4: sidebands of the modes 0,1 and N_b-1 close to the main and harmonic cavity impedances.

[45] In this case the bunches become unstable. This is also called the second Robinson limit.

The fact that, for a certain parameter set, $\omega_{c\mu}$ can tend to 0 for a certain beam current, can be physically explained in the following way: as $\omega_{c\mu}\rightarrow 0$, the restoring force for the oscillation mode μ due to the total RF accelerating field is completely "compensated" by the force due to the long range wake field and the "equivalent" RF slope for such a mode approaches to 0.
Following this explanation, since in the eq. (1.79) the incoherent synchrotron angular frequency is averaged over the bunch, it may happen that some particles "inside" the bunch reach the second Robinson limit before the whole bunch considered as a rigid macroparticle and that bunch becames, therefore, unstable.
For this reason it may be interesting to calculate the formulae (1.79) considering the incoherent angular synchrotron frequency of a particle that performs small amplitude oscillations (the ω_s in this case is given by (1.69)). The ratios between the coherent and the incoherent values of the synchrotron frequencies for the modes "0", "1" and "N_b-1" are shown in Fig. 3.5 as a function of the total stored current, considering both the formulae (1.79)-(1.69) (case 1) and (1.79)-(1.80) (case 2) and different initial detuning of the main cavity ([46]).
As predictable, the mode "0" is the most perturbed since it interacts with the impedance of both main and harmonic cavities and, in order to prevent the mode "0" coherent frequency getting too small in the case 1, a large detuning of the main RF cavity has to be provided ($Q_L\delta_0\cong 1.2$).
This condition corresponds to an inefficient operation of the main RF system (~60% of RF power reflected at the cavity input coupler). However, this is a conservative estimate since it is based on a linear macroparticle theory and the effects of the distribution function and large non-linearities of the longitudinal focusing force are not taken into account[47].
The expected shifts of the coherent frequencies of modes "1" and "N_b-1" are much smaller, while they are almost negligible for the other coupled-bunch modes. With the exception of the mode "0", which is damped by a dedicated feedback system as well as by the Robinson mechanism, the frequencies of all the CB modes remain inside the operational bandwidth of the DAΦNE bunch-by-bunch longitudinal feedback system.
The growth rates of modes "0", "1" and "N_b-1" are shown in Fig. 3.7. The expected growth rate of mode "1" is much smaller than the typical damping rate provided by the DAΦNE LFB system (~10 μs^{-1}).

[46] As discussed in the par. 1.3.3 the resonant frequency of the main cavity changes if the current increases to compensate the beam loading effects. The final resonant frequency depends on the initial detuning.
[47] The problem of the mode "0" coherent frequency shift could be relaxed by implementing a direct RF feedback around the RF system [92] that reduces the imaginary impedance sampled by the mode "0" sidebands and, as consequence, the shift of the mode "0" coherent frequency.

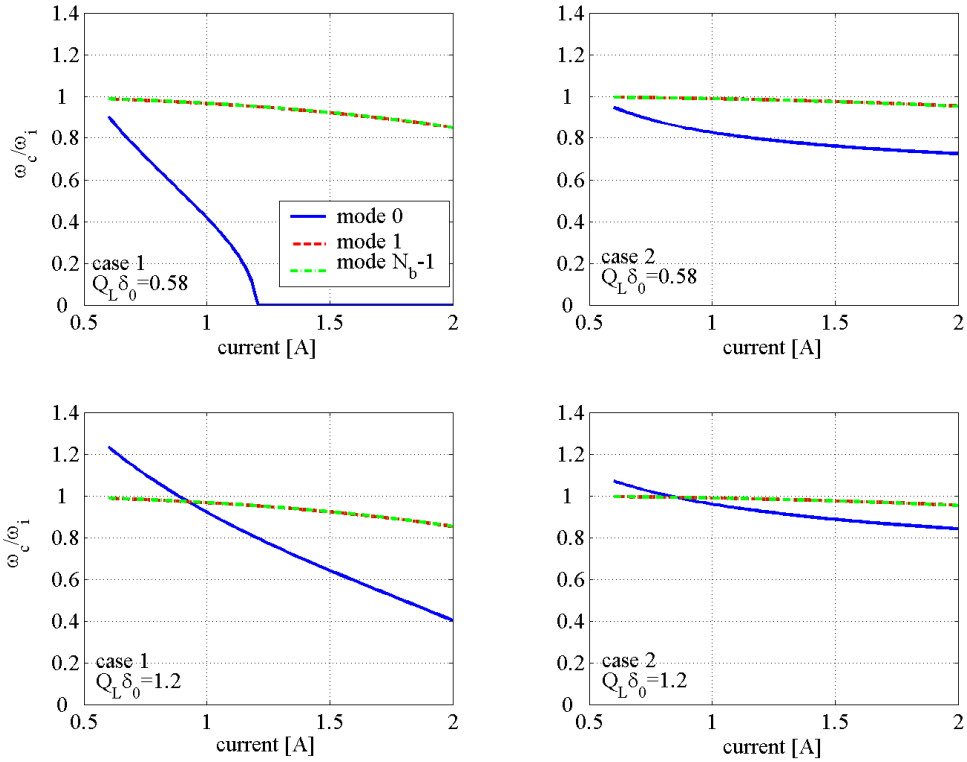

Fig 3.5: ratios between the coherent and the incoherent values of the synchrotron frequencies for the modes “0”, “1” and “N_b-1” as a function of the total stored current

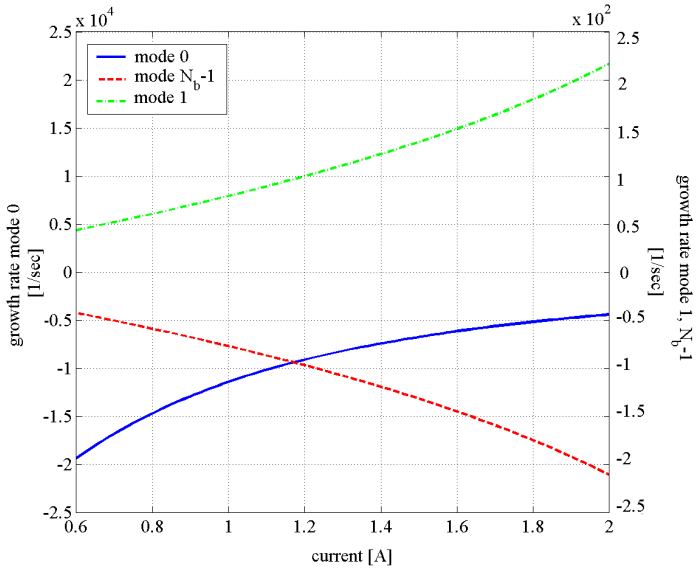

Fig 3.6: growth rates of the modes “0”, “1” and “N_b-1” as a function of the total stored current.

3.1.2 Operation with a gap in the bunch filling pattern

The modal expansion, which is the base of the theory used in the previous paragraph to calculate the coherent frequency shifts, is completely appropriate only in the case of multibunch beams with uniform filling pattern (same charge and shape of each bunch and no gaps along the pattern). This condition cannot be fulfilled in DAΦNE, since a gap of 20÷30% in the filling pattern is required in the e^- ring to prevent the ion trapping [93] and consequently transverse beam emittance blow up.
The analytical results obtained from the theory have to be interpreted as an indication, and have to be validated, in the presence of a gap in the bunch filling pattern, by numerical simulations.
In the multibunch tracking code discussed in par. 1.3.4, it is possible to include the contribution of the passive harmonic cavity adding in the HOMs the impedance due to the harmonic cavity itself.
Results from tracking simulations of uniformly filled multibunch beams are in a very good agreement with the theory. However, when a gap is introduced in the bunch filling pattern, the situation described by the tracking code is strongly perturbed.
The long-range wakes sampled by each bunch depend on the bunch position along the train. This generates a spread of the parasitic losses along the train and, as consequence, a spread of bunches synchronous phases. In ALS, where passive harmonic cavities have been installed, this effect has been already observed [94].
This effect is already well evident also in DAΦNE, but, due to the large linear range of the RF voltage, it does not significantly affect the synchrotron frequency and the shape of each bunch.
The effect is largely magnified in presence of the harmonic voltage for the two following reasons:

a) to the long-range wakes of the machine one has to add the contribution due to the harmonic cavity impedance that gives, as illustrated in the following, further losses spread along the train;

b) the total RF voltage (main+harmonic cavity) has a very little slope around the synchronous phase and it is, also, strongly non-linear. The result is that the parasitic loss spread is converted in a large synchronous phase spread.

This effect can be also conveniently described in the frequency domain. In fact, because of the gap in the filling pattern, the beam spectrum contains all the revolution harmonics. In the ideal case, with no gap in the pattern, only the harmonics of the bunch repetition frequency would be present (see eq. (1.83)).
In Fig. 3.7 the DAΦNE beam spectrum near the harmonic 3h is reported in the case of a uniform filling pattern (60 bunches over 60) and considering a gap (45 bunches over 60) without synchrotron phases spread.

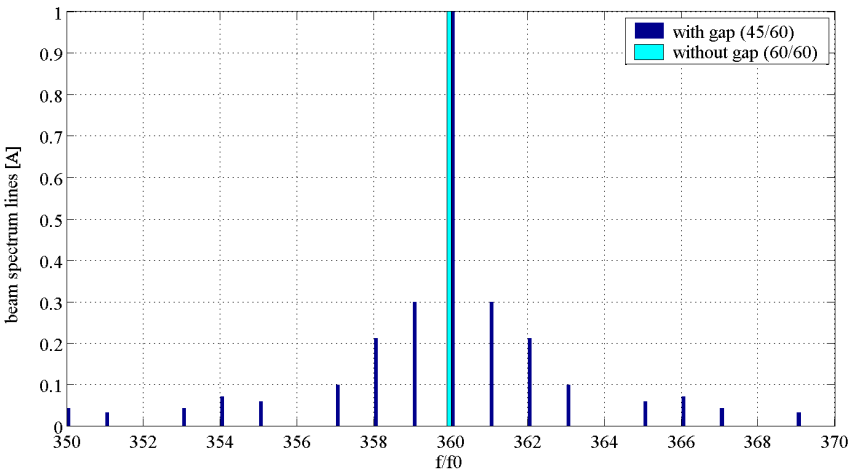

Fig 3.7: DAΦNE beam spectrum near the harmonic 3h in the case of a uniform filling pattern (60 bunches over 60) and considering a gap (45 bunches over 45) without synchrotron phase spread.

Because of the gap, also other lines are present, and the total accelerating voltage is given by:

$$V_T(t) = V_{RF}\cos(\omega_{RF}t + \varphi_s) + V_{RFH}\cos(3\omega_{RF}t + \varphi_H) + V_{NH}(t) \tag{3.2}$$

where

$$V_{NH}(t) = -\mathrm{Re}\left[\sum_{k\neq h,3h} \tilde{I}_k Z_T(k\omega_r) e^{jk\omega_r t}\right] \tag{3.3}$$

where $Z_T(\omega)$ is the total ring impedance, which is mainly given by the two contributions of the RF cavity and harmonic cavity accelerating modes. In the expression (3.2) the total voltage $V_T(t)$ is represented as a sum of 3 terms: the first one is the main RF voltage, which is actively excited by the RF system; the second term is the harmonic voltage, which is passively excited by the beam with an amplitude that can be varied by changing the harmonic cavity tuning; the third term $V_{NH}(t)$, contrary to the previous two, has only the revolution periodicity, which means that it produces a constant voltage over a given bunch, but different voltages over different bunches in the train (NH means "non-harmonic" voltage).
The parasitic loss spread can be, therefore, seen as the spread of the non-harmonic voltage values as sampled by the bunches along the train.
The bunch positions given by the tracking simulation code comparing the present DAΦNE working point to the one proposed for implementing the harmonic cavity are shown in Fig. 3.8. In the figure dots represent the positions of the macro-particles distributed over the RF voltage (the non-harmonic voltage is not included in this representation).

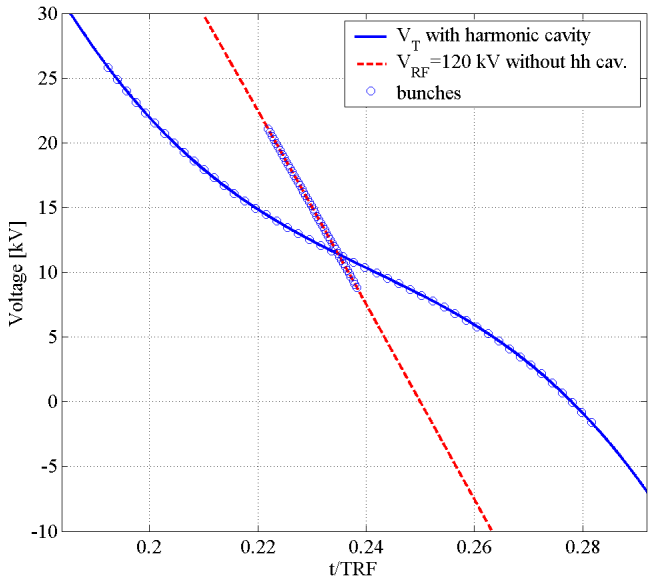

Fig 3.8: bunch positions given by the tracking simulation code comparing the present DAΦNE working point to the one proposed for implementing the harmonic cavity (I=1.2 A).

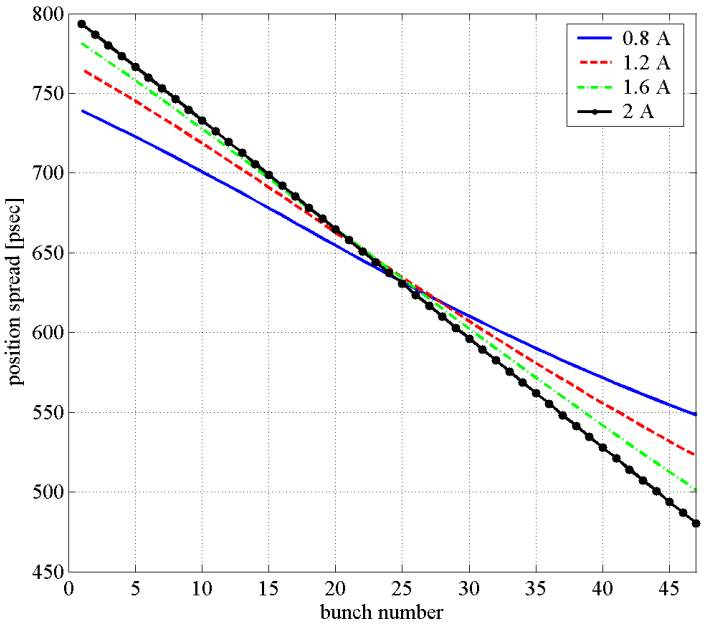

Fig 3.9: bunches position as a function of the bunch number for a train of 47 bunches spaced 2 RF periods with the harmonic cavity.

The bunch positions as a function of the bunch number for a train of 47 bunches spaced 2 RF periods, including the effect of the harmonic cavity and for total current values of 0.8, 1.2, 1.6 and 2 A are shown in Fig. 3.9. The synchronous phases variation is almost linear along the train and changes from ~180 ps to ~320 ps.

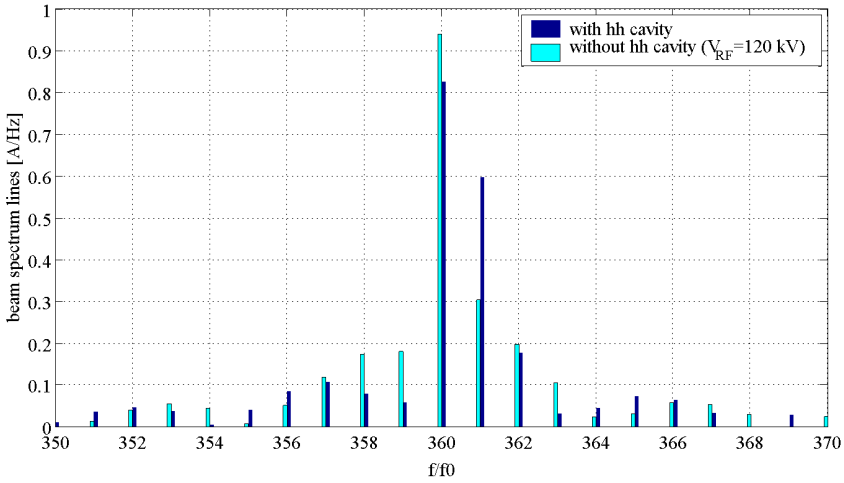

Fig 3.10: DAΦNE beam spectrum near the harmonic 3h considering 47 bunches over 60 with and without the harmonic cavity

It is also important to observe that the displacing of the bunch positions from the "unperturbed" synchronous phases produces a significant distortion of the beam current spectrum. As an example, the spectra of the beam current near the 3h harmonics are reported in Fig. 3.10 in the two cases. A large head-tail displacement of the bunch synchronous phases produces a modulation of the "powerful" harmonics and a distortion of the revolution harmonics around them. It was surprising to find that in this case the intensity of the line 3h (the beam spectrum line powering the 3rd harmonic cavity) is comparable with that of the adjacent line (3h+1).

The total voltage and the non-harmonic voltage around bunch 1, 12, 24, 36 and 47 are plotted in Fig. 3.11 for a beam of 1.6 A in 47 bunches. The non-harmonic voltage sampled at the position of the bunch centroid sets the bunch parasitic loss individual value (in the case of 94 bunches over 120 and for the same total current the situation is exactly the same in terms of non harmonic voltages and head-tail synchronous phases spread).

The non-harmonic voltage over the bunch is an additional perturbation of the potential well and has to be taken into account to compute the bunch natural and lengthened profiles. In particular, it may be observed that bunches at the edge of the train seat close to a maximum or minimum of the non-harmonic voltage and their potential wells are almost unperturbed. On the contrary, the phase of the non-harmonic voltage is almost opposite to that of the 3rd harmonic voltage over the central bunch of the train, so that the lengthening effect is weakened.

Since the bunch centroids occupy different positions along the total RF voltage (which is largely non-linear) and since the non-harmonic voltage has a different form over the bunches, each bunch seats at a different RF slope and ends up with its own synchrotron frequency and charge distribution. Each bunch has, therefore, its own "natural" length, its equilibrium profile (in the lengthening regime) and its own Touschek lifetime.

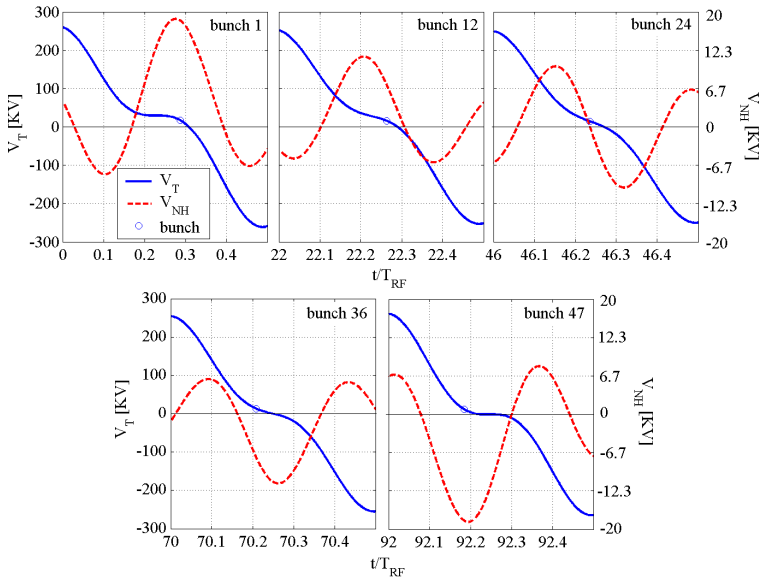

Fig. 3.11: total voltage and non-harmonic voltage around bunch 1, 12, 24, 36, 47 in the case of 47 bunches over 60 (or 1, 24, 48, 72, 94 in the case of 94 bunches over 120) with a total beam current of 1.6 A.

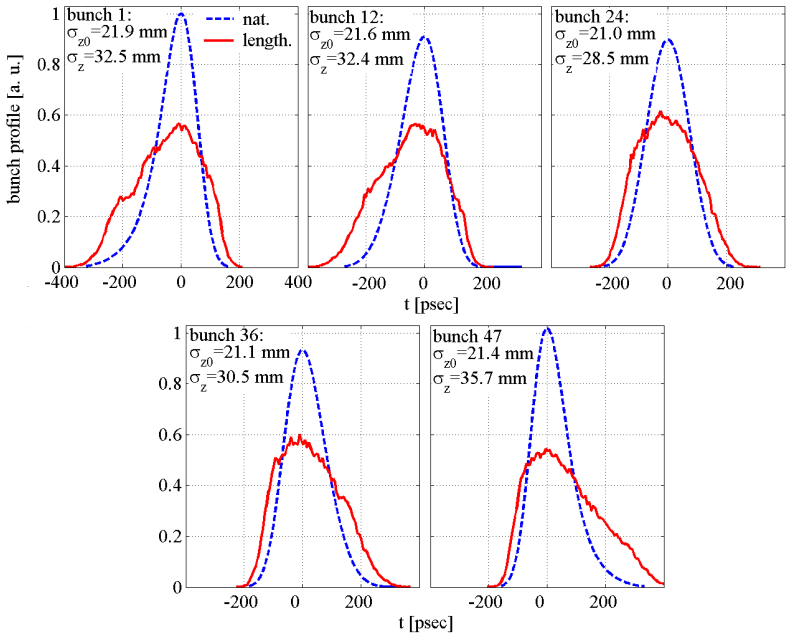

Fig. 3.12: natural and lengthened profiles of the bunches (1.6 A into 47 bunches)

The natural and lengthened profiles of bunches 1, 12, 24, 36, 47 in the case of 47 bunches over 60 are shown in Fig. 3.12. The beam current is 1.6 A (≈34 mA per bunch). The positions of the bunch centroids have been obtained from the macroparticle tracking, as discussed before, while the profiles have been obtained from the single bunch tracking code.

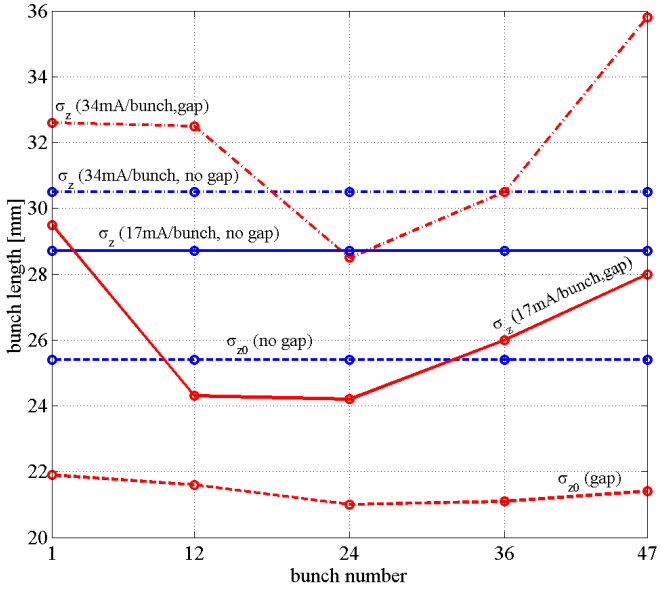

Fig 3.13: natural and lengthened bunch lengths as function of the bunch number.

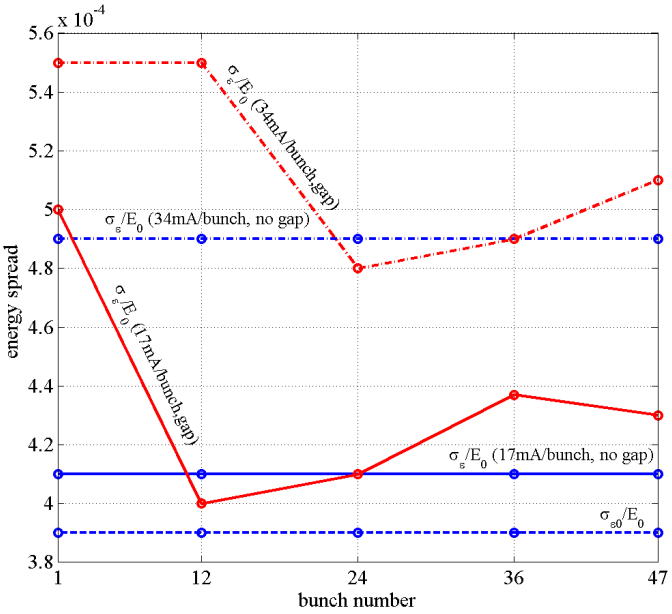

Fig 3.14: energy spread as function of the bunch number.

The r.m.s. natural and lengthened bunch lengths as function of the bunch number are reported in Fig. 3.13 for the mentioned five bunches and compared with the natural bunch length with and without gap. The relative energy spreads are reported in Fig. 3.14.

It may be seen that, considering the natural bunch length, the bunches do not reach the design length. This is because the bunches near the train edges seat outside the low RF slope region while the RF slope over the central bunches is increased by the non-harmonic voltage contribution.

In the strong lengthening regime (34 mA per bunch), however, there is an increase of the bunch length due to the turbulent regime that strongly lengthens the bunches more than without the gap. This effect is confirmed by the increase of the energy spread of the bunches.
A large spread of the synchronous phases is cumbersome at least from two points of view. First of all, the position of the interaction point (IP) changes from bunch to bunch which may cause problems to the experiments as well as luminosity degradation if some bunch centroids collide significantly apart from the waist of the vertical β-function. One could argue that, provided that the synchronous phase spread is equal in the two beams, the IP position remains fixed and only the collision times vary with respect to the RF clock. But there is little hope that the synchronous phase spread will be equal in the two rings, since in each ring it is generated by the long range wake fields associated to all machine HOMs. As a matter of fact, we already observed a substantial difference in the bunch phase spread in the two DAΦNE rings in present operation which is probably due to a difference in the HOMs distribution in the two RF cavities (their internal profile is not exactly equal).
The impact of the bunch phase spread on the operational efficiency of the DAΦNE LFB system is the second worrying aspect. The LFB is a synchronous system timed on the RF clock. In particular, the front-end works at $6f_{RF}$ while the back-end (the part of hardware dedicated to kick properly each bunch) works at $3.25f_{RF}$. Both hardware sections will suffer from an excessive phases deviation of the bunch from a common equilibrium value. In particular, the front-end phase detector has a limited dynamic range, which can be overcome by an excessive phase spread while the back-end section can not be properly phased on all the bunches.
The tracked oscillations of bunches 1, 24 and 47 for a beam current of 1.6 A into 47 bunches with and without LFB are shown in Fig. 3.15. It may be seen that the damping of the LFB is still necessary, even though we know that it can not be effective on the bunches near the train edges because of the off-time of both the front-end and back-end sections.
It might be asked if there is a way to limit the spread of the synchronous phases or, at least, some of its effects. Only in the e^+ ring it is possible to remove the spread by removing the gap in the filling pattern. This will increase the average beam current, increasing the background production but not the luminosity, since the extra bunches closing the gap have no partner bunches in the other beam. Nevertheless, this kind of operation may have some advantages like a better average lifetime of the e^+ beam and a less critical operation of the e^+ LFB system.
The stability of the LFB system operation could be possibly improved even without removing the gap. In this case one should, in principle, synchronize the system on a linearly phase modulated RF tone, to follow the phase displacement from bunch to bunch. A solution of that kind seems to be feasible from a technical point of view [95].

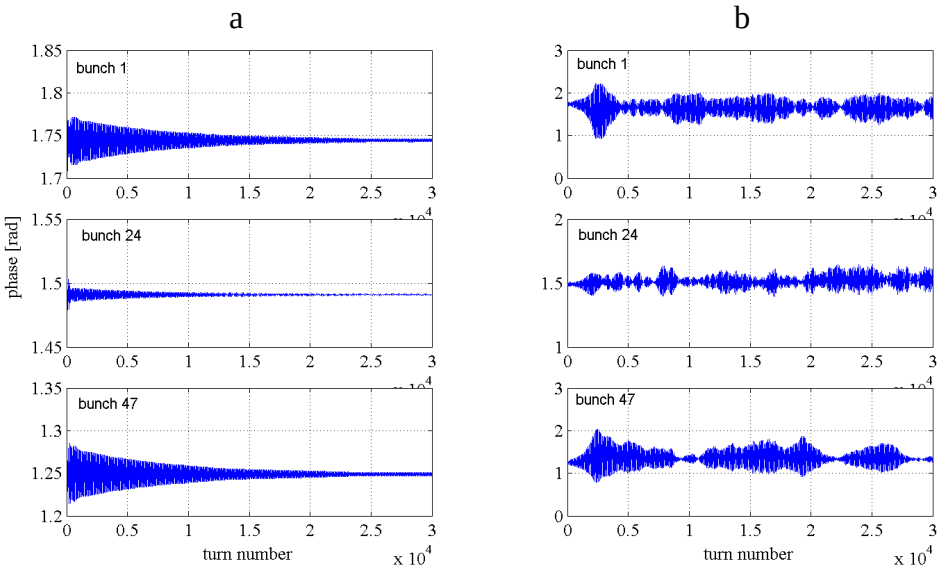

Fig 3.15: tracked oscillations of bunches 1, 24 and 47 for a beam current of 1.6 A into 47 bunches over 60 with (a) and without (b) LFB.

3.1.3 Expected improvement in the lifetime with the 3rd harmonic cavity

The DAΦNE beam lifetime is dominated by the Tousckek effect [96].
Supposing that the limiting acceptance for the relative momentum deviation is given by the minimum between the RF acceptance and the physical transverse aperture, the Touschek lifetime can be calculated in each longitudinal point s of the machine by the formula (1.100). The total lifetime can be finally calculated by the equation (1.102).
The performed calculations give the results plotted in Fig. 3.16. In the plot the bunch lifetimes with the harmonic cavity are compared with those calculated in the present operation conditions (V_{RF}=110 KV) and with V_{RF}=200 KV (without harmonic cavity) for two different bunch currents (17 and 34 mA).
Considering the case V_{RF}=110 KV, without the gap, it is important to observe that:

a) the bunches have the same lifetime because there is no spread of the synchronous phases;
b) there is an improvement of ~90% and ~75% in the lifetime with a bunch current of 17 and 34 mA respectively. This improvement is given by the enlargement of the energy acceptance and by the fact that the bunch is longer;
c) in the case of 34 mA/bunch the improvement is reduced because the lengthening process without the harmonic cavity is more pronounced;

In the presence of a gap, because of the synchronous phase spreads, each bunch has its proper lifetime. Also in this case, however, the average beam lifetime improvement is ~80% and is worst for the central bunches of the beam that are shorter.
Similar considerations can be done in the case of V_{RF}=200 KV. In this case the improvement is only given by the fact that the bunch is longer because the energy acceptance is almost the same (~0.75%).

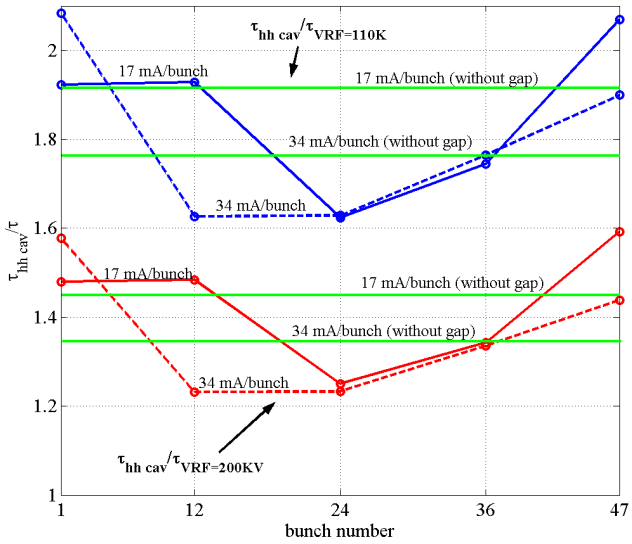

Fig 3.16 DAΦNE Touschek lifetime improvement with the harmonic cavity.

3.1.4 The cavity parking option

As discussed in the previous paragraphs, the implementation of the harmonic cavity presents beneficial aspects such as lifetime and Landau damping increase but also other effects like the amplification of the synchronous phase spread, whose impact on the collider is not completely predictable.
A back-up procedure consists in tuning the harmonic cavity between two revolution harmonics sufficiently away from the 3h lines (for instance $\omega_{RFH} \cong (3h+0.5+k)\omega_0$ with k=1,2,3).
This option is the so-called “cavity parking”. By parking the harmonic cavity one expects to recover approximately the operating conditions existing before the harmonic cavity installation because the harmonic voltage is quite low and the interaction of the cavity impedance with beam is minimized (but still significant).
In this case, in fact, the cavity interact with the modes N_b-1, 1, N_b-2, 2 and so on depending on the number k.
In Fig. 3.17 the coherent angular frequencies and growth rates of the modes 2 and 3 as a function of the beam current are plotted for the case k=2 and with the present DAΦNE operation parameters. As shown, the frequency shifts and the growth rates are small enough to consider the perturbation almost negligible.
The synchronous phase spread for a current of 1.6 A with a gap of 22% is shown in Fig. 3.18 for k=1, 2, 3. It may be seen that the phase deviation is not anymore linear with the bunch position along the train, while the total spread is even smaller than the value expected at the same current without harmonic cavity. This is not surprising, since it may be demonstrated that, provided that k>1, there is a partial compensation of the wakes generated by the accelerating mode impedances of the main and harmonic cavities.

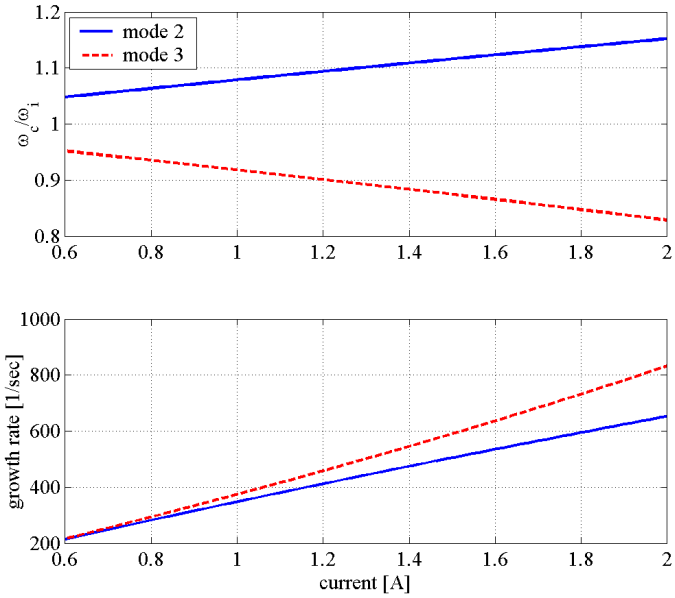

Fig. 3.17: coherent angular frequencies and growth rates of the modes 2 and 3 as a function of the beam current for the parking case k=2.

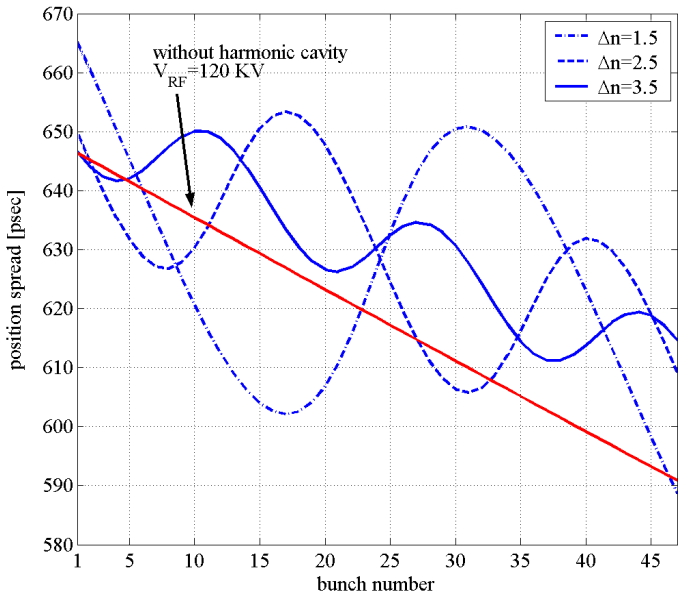

Fig 3.18 The synchronous phase spread for a current of 1.6 A for k=1, 2, 3.

3.1.6 Conclusions

Using a passive 3rd harmonic cavity in the lengthening regime can improve the Touschek lifetime of the DAΦNE beam by a factor equal to the ~80% if compared with the present operation conditions

This is obtained by increasing the RF acceptance while keeping the bunch length at the limit of the hourglass effect. The microwave lengthening process is less pronounced and the larger non-linearities of the harmonic voltage over the bunch increase substantially the Landau damping.
Both these effects are expected to result in a more relaxed single and multibunch dynamics.
On the other hand, the presence of a gap in the bunch filling pattern will produce a large spread in parasitic losses and synchronous phases. As a consequence, the Touschek lifetime gain is not uniform over the train, different bunches will collide at different IPs and the synchronization of the bunch-by-bunch feedback systems may be affected. The actual tolerability of such effects cannot be exactly predicted depending on the operating conditions (such as the gap width).
The parking option (that consists in tuning the cavity away from the 3rd harmonic frequency and in-between two revolution harmonics) allows to recover approximately the operating condition established before the harmonic cavity installation, and may be considered a reliable back-up procedure. Moreover, in the parking option the synchronous phase spread is compressed by a long-range wake compensation effect, and a very moderate harmonic voltage is still present, which is expected to increase the Landau damping in the longitudinal dynamics.

3.2 DAΦNE harmonic cavity design

The design of the harmonic cavity has been aimed to obtain a relatively low R/Q factor with a Q as high as possible for the beam dynamics considerations discussed in the previous paragraphs. For this reason a spherical shape has been proposed as an optimum compromise between a high Q resonator and a low R/Q factor [97].
For the damping of the higher order modes it has been decided to use the same technique as that adopted at the KEK B-factory [98]. It foresees using special rings of dissipative ferrite material coupled with the HOM and completely decoupled with respect to the field of the accelerating mode.
The final designed shape is shown in Fig. 3.19. The rounded cell is the volume where the fundamental mode resonates. On the cell top there is a port for the insertion of a tuning plunger and three small RF probes have been inserted in the structure to measure the beam-induced field allowing the low-level control and diagnostics. The cell is connected through the tapered section to HOM damper consisting of the ferrite rings bonded on a stainless steel flanges.

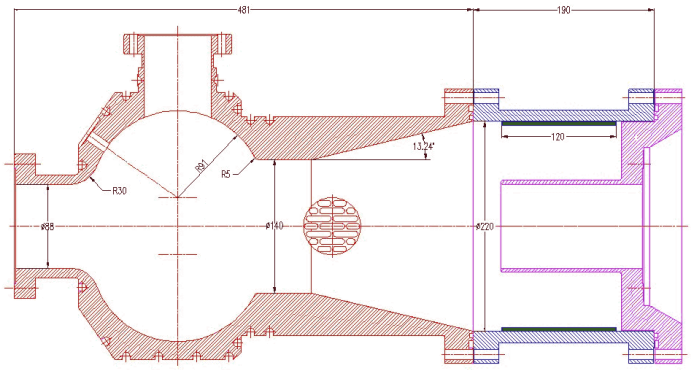

Fig. 3.19: sketch of the DAΦNE 3rd harmonic cavity.

The cavity fundamental mode has been calculated both by MAFIA and by HFSS in order to define the final dimensions of the cavity. The task of the simulations has been to obtain simultaneously:

a) an R/Q of the fundamental mode of about 25 with a Q as high as possible;
b) a strong coupling of the cavity HOMs with the damper and a weak coupling of the fundamental one;
c) controlled dimensions of the cavity because of the limited total length available for allocating the structure in the ring.

For this purpose the radius r1 and r2 of the rounded cell and the dimensions h1, h2, z1 and z2 (Fig. 3.20) have been properly tuned. Furthermore, in order to avoid direct exposure of the ferrite to the beam charge the ferrite load has been shielded by a coaxial cylinder. The shield prevents direct heating of the ferrite that, in this case, can interact with the beam only through the cavity HOMs. Moreover this solution avoids the risk of degradation of the DAΦNE broadband impedance associated with the direct beam-ferrite interaction[48].
To reduce the cost it has been decided to build the cavity body in aluminum instead of copper even if this implies a reduction of the fundamental mode Q-factor by ~20%.
Since the e.m properties of the special ferrites used in the HOM dampers varies with the frequency [99], in the simulations of the ferrites it has been considered the following averaged characterization:

0-1.5 GHz $\rightarrow \varepsilon_r=12\ \mu_r=2+10j$
1.5-3 GHz $\rightarrow \varepsilon_r=12\ \mu_r=0.5+5j$

[48] That risk cannot be easily evaluated by means of simulations or analytical estimates [100].

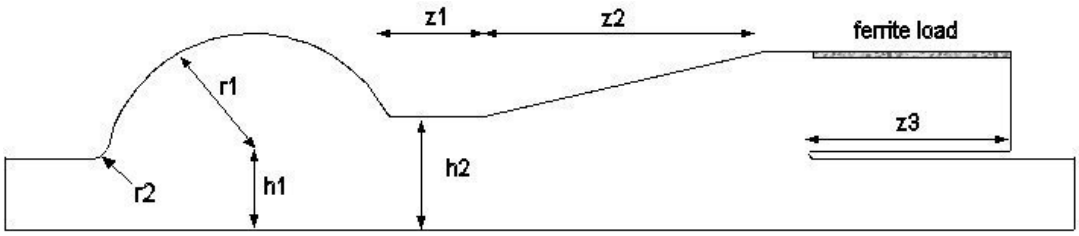

Fig. 3.20: cavity profile simulated by MAFIA and HFSS.

The resonant frequencies (f), the R/Q and the Q values of the cavity longitudinal modes (M=monopole) as given by the MAFIA simulations of the 2D profile are reported in Table 3.3 (the HFSS simulations give substantially the same results).
In Table 3.4 the resonant frequencies and the transverse impedances for the dipole modes (D) are reported while in Table 3.5 the frequencies (up to 2.5 GHz) and the Q factors of the quadrupole (Q), sextupole (S) and octupole (O) modes.
Some of these modes are weakly coupled with the damper (high Q factors) but they don't give longitudinal or transverse impedances to the first order (see par. 1.1.1).
In Figs. 3.21a and b the magnitude of the Electric field of the working modes M1 and of the HOM M4 is plotted, as obtained by HFSS. In the first case the e.m. field vanishes in the tapered transition and only a negligible amount of power can reach the damper while in the second one the e.m. field propagates through the transition toward the ferrite load.

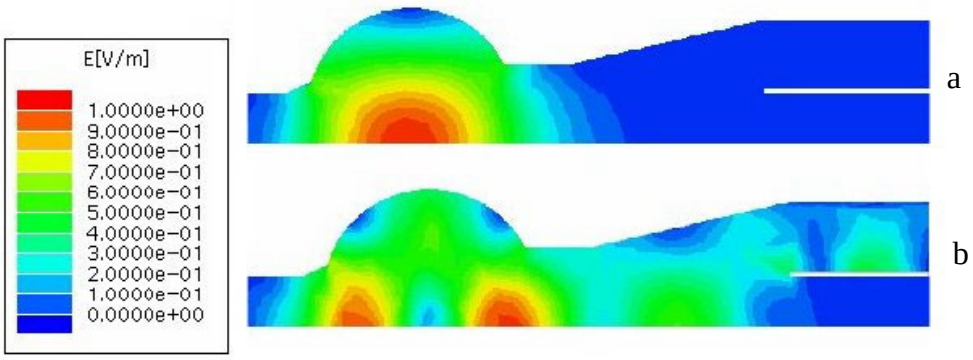

Fig. 3.21: Magnitude of the electric field of the working mode M1 (a) and of the HOM M4 (b) obtained by HFSS.

Table 3.3: monopole cavity modes obtained by 2D MAFIA simulations.

	MAFIA Simulations		
	f [GHz]	Q	R/Q [Ω]
M_1	1.105	28000	26
M_2	1.335	10	16
M_3	1.600	30	6
M_4	1.650	50	2
M_5	1.899	50	4
M_6	2.094	110	7
M_7	2.270	120	9
M_8	2.495	170	3
M_9	2.524	230	10

Table 3.4: dipole cavity modes obtained by 2D MAFIA simulations

	MAFIA Simulations		
	f [GHz]	Q	R/Q [Ω/m]
D_1	1.089	438	66
D_2	1.244	35	26
D_3	1.445	158	22
D_4	1.618	158	29
D_5	1.797	266	37
D_6	1.886	283	24

Table 3.5: quadrupolar (Q), sextupolar (S) and octupolar (O) cavity modes obtained by 2D MAFIA simulations

	f [GHz]	Q
Q_1	1.597	19700
Q_2	1.975	340
Q_3	2.078	30
Q_4	2.242	40
Q_5	2.323	40
Q_6	2.398	90
Q_7	2.448	130
S_1	2.042	36930
S_2	2.469	12400
O_1	2.471	36700

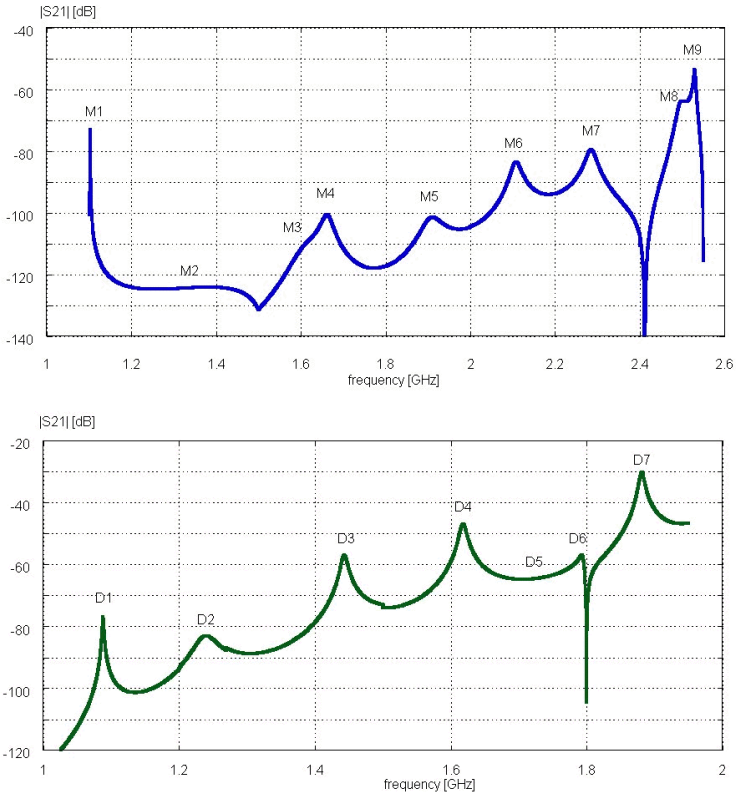

Fig. 3.22: $|S_{12}|$ obtained by HFSS exciting the longitudinal (a) and dipole (b) modes by two RF probes.

HFSS simulations exciting the cavity by two RF probes have been also performed. The obtained R and Q values confirm the previous simulations results and in Figs. 3.22a and b the resulting $|S_{12}|$ is shown as a function of frequency for the longitudinal and dipole modes respectively.
The tuner inserted in the cavity allows to properly set the cavity frequency with beam current or to "park" the cavity itself.
Since it perturbs the 2D profile of the structure, two relevant effects have been examined:

a) first of all there is a degradation of the Q factor of the fundamental mode caused by the strong field in the gap between the tuner itself and the cylinder in which it is allocated. According to numerical simulations, the reduction of Q with respect to 2D results is ~20% with the cavity properly tuned, or ~30% with the tuner in the "parking option" position. In Fig. 3.23 the magnitude of the H field between the tuner and the outer cylinder corresponding to the fundamental mode as obtained by MAFIA is plotted;

b) the second relevant effect is the appearance, in the case of "parked cavity", of longitudinal and transverse impedance due to the quadrupole mode (Q1).

In fact, while in the 2D symmetric geometries the quadrupole modes have not transverse and longitudinal impedance, in this case, the presence of the tuner strongly perturbs the symmetry of the cavity inducing a non zero longitudinal and transverse impedance. In Fig. 3.24 the longitudinal Electric field of this quadrupole mode with the tuner deeply inserted as obtained by HFSS is plotted. When the tuner is inserted to shift the fundamental mode at 1.113 GHz ($\cong 3f_{RF}+2.5f_0$), HFSS provides for this mode: f≅1.559 [GHz] Q≅10000 Rs/Q≅0.59 [Ω] R_t/Q≅0.1 [Ω/m].

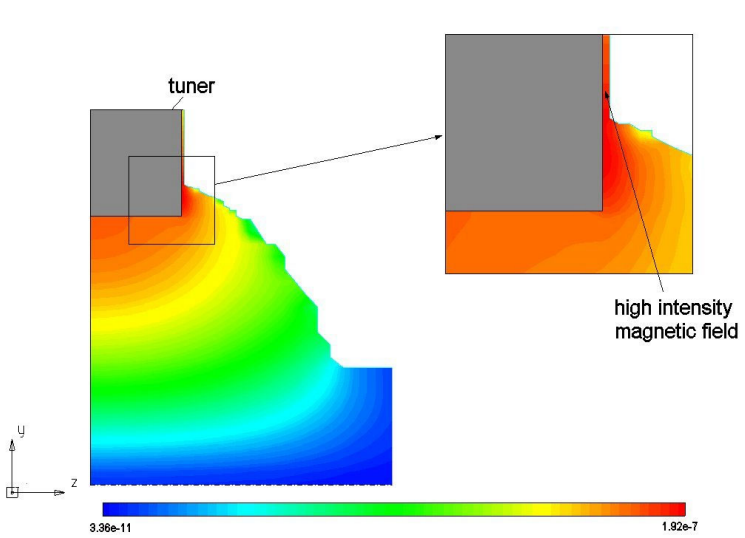

Fig. 3.23: Magnitude of the H field between the tuner and the outer cylinder corresponding to the fundamental mode as obtained by MAFIA 3D simulation.

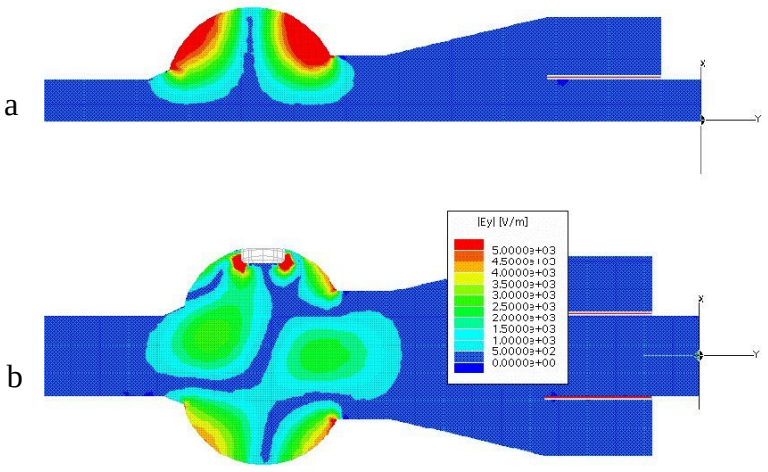

Fig. 3.24. Electric field of the quadrupole mode Q_1 obtained by HFSS without the tuner (a) and with the tuner deeply inserted (b).

3.3 DAΦNE harmonic cavity RF measurement results

The picture of the DAΦNE harmonic cavity is shown in Fig. 3.25.
The RF measurements have been, substantially, of two types:

a) port-to-port transmission coefficient ($|S_{12}|$) between two probes to measure the resonant frequencies and the Q-factors of the fundamental and higher order modes. This measurement has also allowed to check the range of tunability of the fundamental mode itself by changing the tuner position;

b) wire measurements of the longitudinal and transverse impedances in order to evaluate the longitudinal and vertical coupling impedance. As discussed in par. 2.4.2, this method allows measuring the impedances with good precision in the case of "lumped impedances" even if it perturbs both the field configuration and the resonant frequencies of the cavity modes. In this case both the longitudinal and vertical impedances are not properly "lumped" elements and, furthermore, the wire itself modifies the HOM coupling with the damper ring, as we will discuss in the following. In any case this kind of measurement can give some useful informations on the impedance overview.

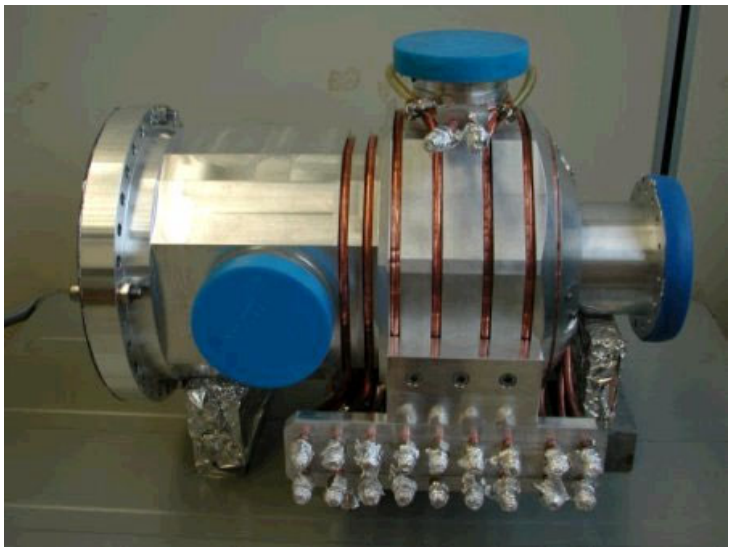

Fig. 3.25:picture of the DAΦNE harmonic cavity.

3.3.1 Tuned cavity

The resonant frequencies (f), the R/Qs and the Q values of the cavity longitudinal (M) and transverse (D) (V and H identify the vertical and the horizontal polarization respectively) modes are reported in Tables 3.6 and 3.7.

Table 3.6: longitudinal modes obtained by measurements and compared with the simulations in the case of tuned cavity

	MAFIA Simulations			**Measurements**		
	f [GHz]	Q	R/Q [Ω]	f [GHz]	Q	R/Q [Ω]
M_1	1.105	23000	26	1.105	18500	21.4
M_2	1.335	10	16	not measurable (n.m.)	n.m.	n.m.
M_3	1.600	30	6	n.m.	n.m.	n.m.
M_4	1.650	50	2	1.65	168	16.8
M_5	1.899	50	4	n.m.	n.m.	n.m.
M_6	2.094	110	7	2.100	224	n.m.
M_7	2.270	120	9	2289	60	n.m.
M_8	2.495	170	3	2.466	140	n.m.
M_9	2.524	230	10	2.507	278	n.m.

Table 3.7: transverse modes obtained by measurements and compared with the simulations in the case of tuned cavity

	Simulations			**Measurements**		
	f [GHz]	Q	R/Q [Ω/m]	f [GHz]	Q	R/Q [Ω/m]
D_1	1.089	438	66	1.070	450	146
D_2	1.244	35	26	not measurable (n.m.)	n.m.	n.m.
D_3	1.445	158	22	1.400	139	29
D_4	1.618	158	29	1.560	175	n.m.
D_5	1.797	266	37	1.725	163	n.m.
D_6	1.886	283	24	1.865	190	74

The modes have been measured in the case of tuned cavity and compared with the simulations of the 2D MAFIA structure. The resonant frequencies (f) and the Q values of the modes have been calculated by fitting the port-to-port transmission coefficient (reported in Fig. 3.26) between two RF probes while the R/Qs have been obtained by the wire measurement (reported in Figs. 3.27-3.28). As well predicted by simulations the ferrite load substantially damps all the longitudinal and transverse modes with the exception of the fundamental one (M1).
Some modes, calculated by simulations, are not measurable on the prototype because of the low Q values of these modes and because of the presence of high polarity modes with high Q-factors (quadrupoles, sextupoles, octupoles).

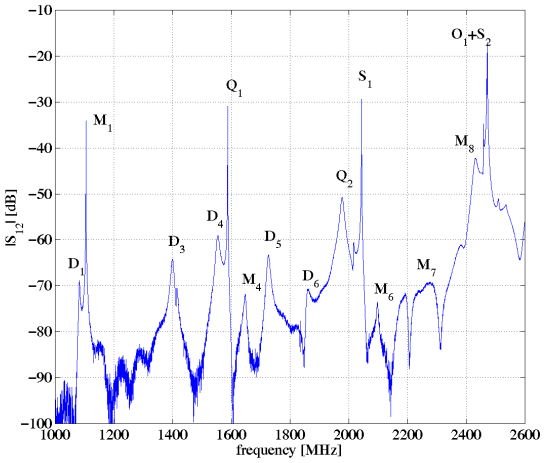

Fig. 3.26: Transmission coefficient ($|S_{12}|$) between two RF probes in the case of tuned cavity.

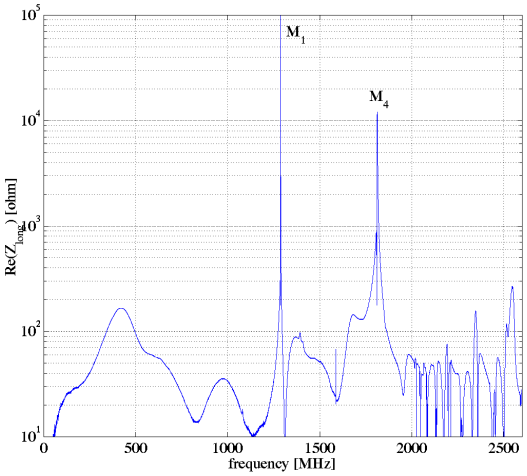

Fig. 3.27: Longitudinal impedance obtained by the wire measurement method (tuned cavity).

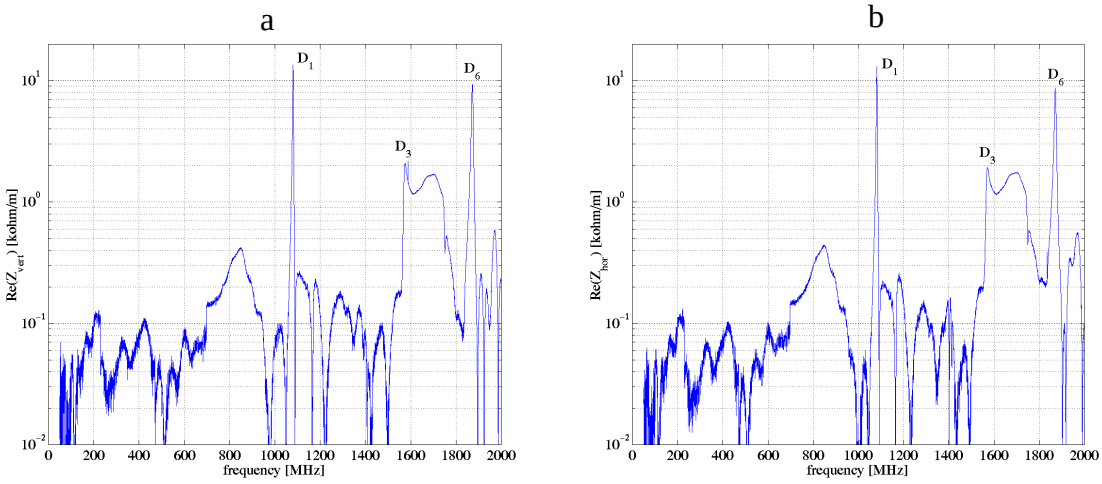

Fig. 3.28 Vertical (a) and horizontal (b) impedances obtained by the wire measurement method in the case of tuned cavity.

As observed before, the results obtained by the wire measurement have to be carefully analyzed. In fact, the wire itself, as it can be seen putting it in HFSS simulations, perturbs both the resonant frequency of the modes and also their field configuration. The coupling with the ferrite damper can be then strongly varied. For example the field resulting from an HFSS simulation of the wire measurement is shown in Fig. 3.29. Without the wire (Fig. 3.29a) the monopole M4 propagates along the tapered transition toward the ferrite load. With the wire (Fig. 3.29b) the e.m. field can propagate along the coaxial line formed by the beam pipe and the wire itself and the ferrite is by-passed. Consequently, the mode is no more damped and a high impedance value is measured at ~1.8 GHz as shown in Fig. 3.27.

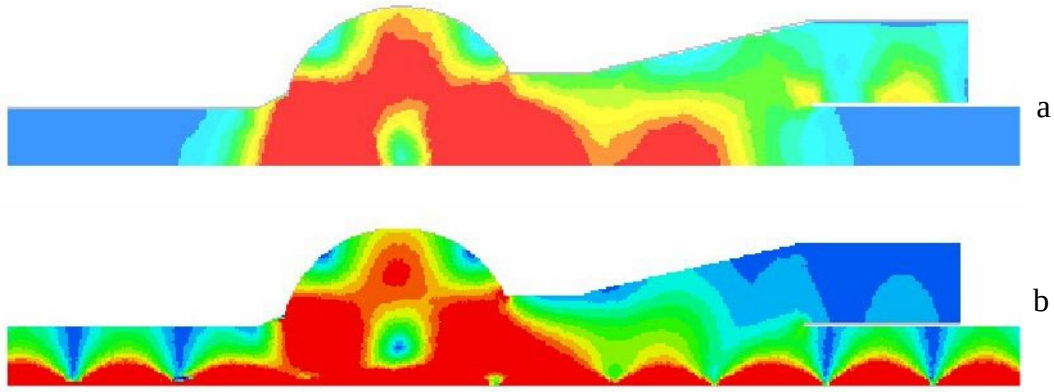

Fig. 3.29. Electric field configuration of the mode M4 obtained by HFSS simulation: (a) without the wire (b) with the wire.

Considering the bunch longer than 2.5 cm, the longitudinal HOMs effective[49] impedance is always lower than 800 Ohm and the dipole modes lower than 25 KΩ/m.
These contributions will not change significantly the present scenario of the DAΦNE Beam Dynamics from the point of view of higher order mode impedances and, on the contrary, one expects beneficial contributions to the beam dynamics from the Landau damping which will be strongly emphasized by the non-linearity of the harmonic voltage.
The resonant frequency of the fundamental mode as a function of the tuner position is shown in (Fig. 3.30).

3.3.2 Parked cavity

A full characterization of the cavity has been performed also when the tuner is in the parking position. The measurement results in this case are shown in Figs. 3.31-3.34. The frequencies, the Q-factors and the R/Q values for the longitudinal and transverse

[49] The impedance multiplied by the exponential factor $\exp(-\omega\sigma_z/c)^2$ (that gives the correct growth rates and coherent frequency shifts in the case of macroparticle model with a finite bunch length (par. 1.3.1)).

modes are reported in the Table 3.8 and 3.9. In this case, as predicted by simulations, it has been found non-zero longitudinal and transverse impedance for the quadrupole mode Q1.
Anyway, also for the parked cavity case it is reasonable to conclude, looking at the effective impedances, that the present scenario of DAΦNE beam dynamics will not be change significantly.

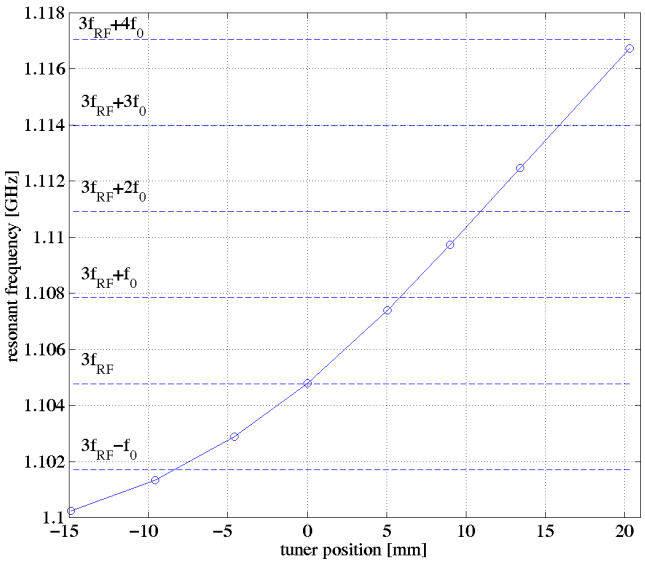

Fig. 3.30 Measured resonant frequency of the fundamental mode as a function of the tuner position.

Table 3.7: longitudinal modes obtained by measurements in the case of parked cavity

	Measurements		
	f [GHz]	Q	R/Q [Ω]
M_1	1.113	12000	18
M_2	not measurable (n.m.)	n.m.	n.m.
M_3	n.m.	n.m.	n.m.
M_4	1.640	90	14
M_5	n.m.	n.m.	n.m.
M_6	n.m.	n.m.	n.m.
M_7	2300	70	n.m.
M_8	n.m.	n.m.	n.m.
M_9	2.520	280	--
Q_1	1.585	11300	0.3

Table 3.8: transverse modes obtained by measurements in the case of parked cavity

	Measurements		
	f [GHz]	Q	R/Q [Ω/m]
D_1	1.087	280	130
D_2	n.m.	n.m.	n.m.
D_3	1.397	140	24
	1420	215	
D_4	n.m.	n.m.	n.m.
D_5	1.728	1170	n.m.
D_6	1.863	70	65
Q_1	1.585	11300	4

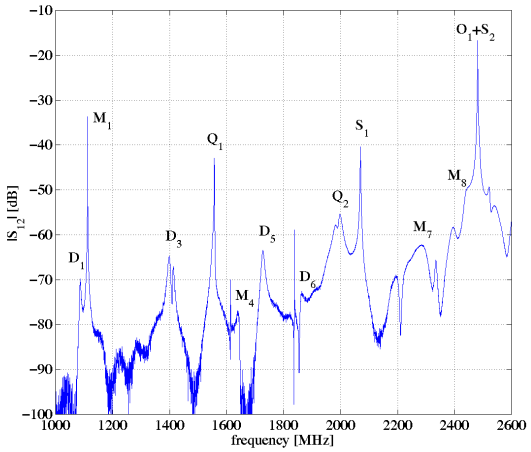

Fig. 3.31 Transmission coefficient ($|S_{12}|$) between two RF probes in the case of parked cavity.

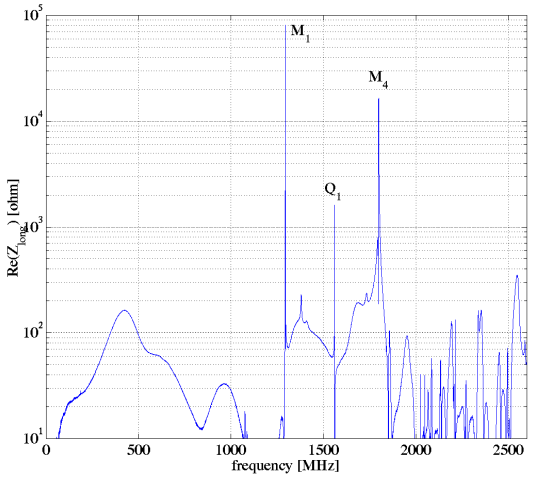

Fig. 3.32 Longitudinal impedance obtained by the wire measurement method in the case of parked cavity.

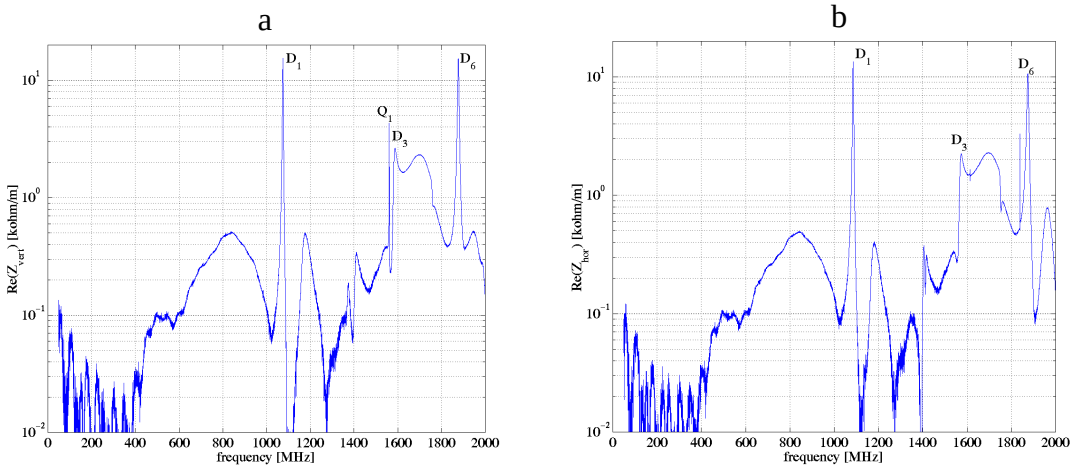

Fig. 3.33. Vertical (a) and horizontal (b) impedance obtained by the wire measurement method in the case of parked cavity.

Chapter 4

RF deflectors for CTF3

CTF3 (CLIC Test Facility) is the third facility of the CLIC (Compact Linear Collider) project. The CLIC study focuses on high-gradient, high frequency (30 GHz) acceleration for multi-TeV linear colliders[50] [101-103]. 30 GHz is considered to be close to the limit beyond which standard technology for the fabrication of normal-conducting tw accelerators cannot longer be used.
Since conventional RF power sources based on modulators and klystrons are not available at this specially high frequency, CLIC was based on the novel and promising concept of Two-Beam Acceleration (TBA).
In the first paragraph of this chapter the basics CLIC-CTF3 concepts are illustrated.
The study of the beam dynamics in the CTF3 Combiner ring considering the effect of the beam loading in the RF deflectors is presented in the second paragraph.
The last two paragraphs are dedicated to illustrate the RF deflectors design procedure and measurements.

4.1 The CLIC-CTF3 Projects

The basic idea of the TBA is to properly recombine the bunch train (Drive Beam) generated by a conventional linear accelerator in order to create an high peak current beam with a time spacing between bunches considerably reduced.
This bunch structure is realized by a novel technique of bunch combination which converts a long bunch train with a large bunch spacing of 64 cm into a sequence of short trains with a bunch spacing of only 2 cm, which is used for 30 GHz power production.
The principle is shown in Fig. 4.1. The bunch manipulation is done in three rings, using RF deflectors, giving a multiplication of the bunch repetition frequency by factor two in the first one and four in each of the two others.
The beam is then decelerated and the extracted power is used to accelerate the beam in the main linac at 30 GHz.

[50] The choice of the high working frequency aims to reach high accelerating field of the order of 160 MV/m. In fact, as shown in (par. 2.2), $r_0 \propto \omega^{1/2}$ and this suggests the choice of high frequencies to reach high acc. field.

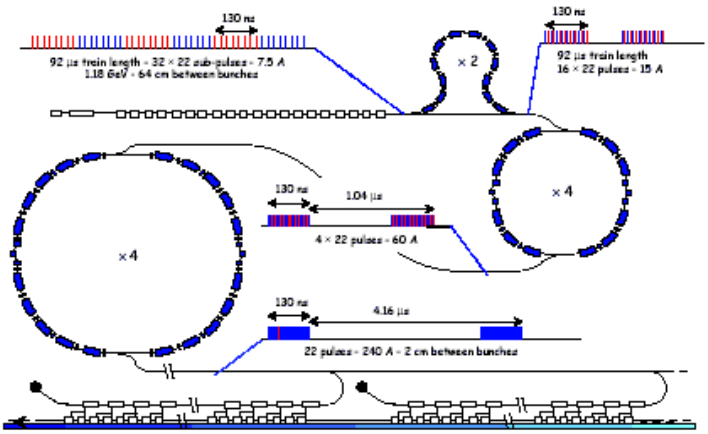

Fig. 4.1: Drive Beam structure of CLIC.

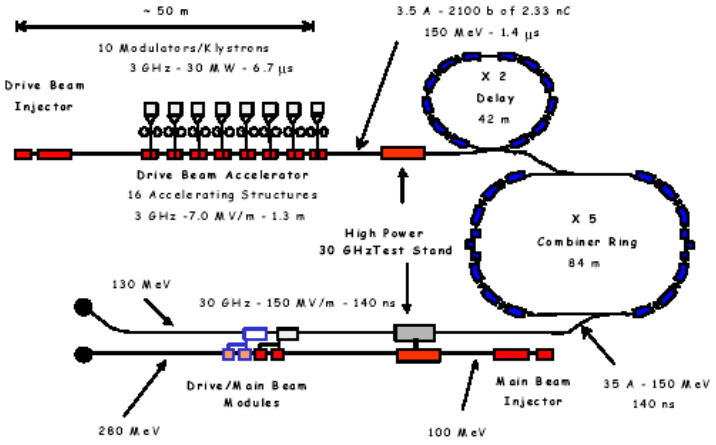

Fig. 4.2: conceptual layout of CTF3.

CTF3 is an important test and demonstration facility for many vital components of CLIC [104]. Its main aim is to prove the feasibility of the RF power source design and to produce 30 GHz power at the nominal CLIC parameters. The conceptual layout of CTF3 is shown in Fig. 4.2.

One of the most important issues to be tested is the frequency multiplication by the novel bunch interleaving technique. In CTF3 a long train of short bunches with a distance of 20 cm between bunches is converted into a series of short bunch trains, with the individual bunches spaced by 2 cm. This is done in two stages, first by a factor of two in the delay loop, then by a factor of 5 in a Combiner ring.

After the linac, a first stage of electron pulse compression and bunch frequency multiplication of the drive beam is obtained using a 42 m circumference Delay Loop with a transverse RF deflector at 1.5 GHz. The circumference of the loop corresponds to the length of one batch of “even” or “odd” bunches. The process is illustrated in Fig. 4.3. The RF deflector in the Delay loop deflects every second batch of 210

bunches into the delay loop, and, after one turn, insert this batch between bunches of the following batch. Therefore the bunch timing of subsequent batches is adjusted in such a way that they have a phase difference of 180 with respect to the ~1.5 GHz RF of the deflector.

An 84 m circumference Combiner Ring is used for a second stage of pulse compression and frequency multiplication by a factor five. This is achieved by means of two RF deflectors working at ~3 GHz, which insert the injected bunches between the already circulating ones, as illustrated in Fig. 4.4.

After the Combiner ring the drive beam pulse is 140 ns long and has a current of 35 A with the 2.33 nC bunches spaced by 2 cm.

A single 30 GHz power extraction structure, optimized for maximum power production, will be used in a high power test stand where CLIC prototype accelerating structures and waveguide components can be tested at the nominal power and beyond.

The main CTF3 parameters at the injection into the Combiner ring are reported in Table 4.1.

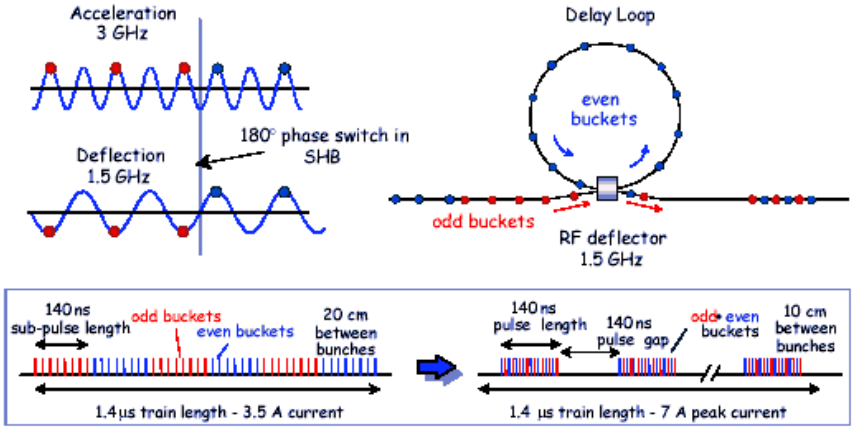

Fig. 4.3: sketch of the bunch frequency multiplication in the Delay Loop.

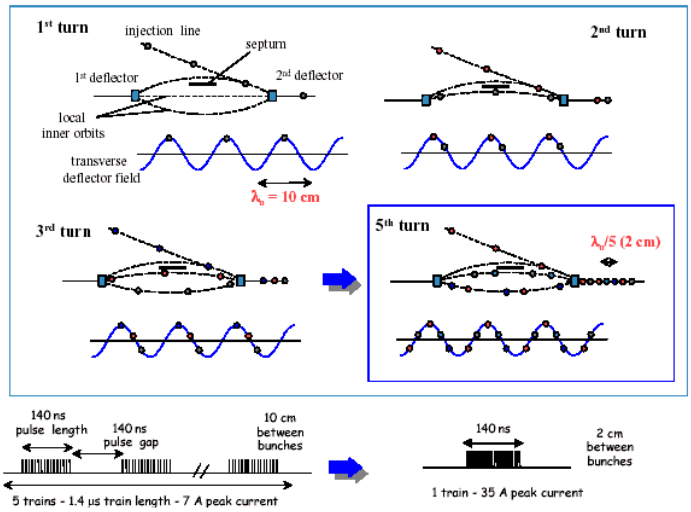

Fig. 4.4: sketch of the bunch frequency multiplication in the Combiner ring.

Table 4.1: The main CTF3 parameters at the injection into the Combiner ring

Energy (E)	180 [MeV][51]
Circumference length (L)	84 m
Pulse duration (τ_{CR})	1.4 [μs]
Number of bunches per pulse (N_b)	2100
Number of pulses recombined (N_p)	5
Bunch charge (Q_b)	2.33 [nC]
Bunch length (σ_z)	1.5-2.5 [mm]
Bunch separation before recombination (τ_{sb})	0.33 [ns]
Bunch separation after recombination (τ_{sa})	0.067 [ns]
Beam emittance (ε)[52]	~ 0.4 [mm mrad]

4.2 Study of the beam loading in the RF deflectors of the Combiner ring

As discussed in the previous paragraph, the bunch train compression in the Combiner ring is obtained by means of two RF deflectors [105].
The efficiency required by the CTF3 parameters can be easily met by scaling already existing tw or sw deflecting structures. On the contrary, the most demanding issues are those related to the beam dynamics, including the beam loading effects on the fundamental deflecting mode [106].
Strong beam loading effects can, in fact, degrade the beam quality in terms of transverse beam dimension growth, or looses of current and, consequently, the effectiveness of the power conversion to 30 GHz.
From this point of view it has been chosen to build tw RF deflectors since wake fields can leave the structure faster due to lowering the filling time. In fact, typical filling times for sw structures at these frequencies are of the order of 900 ns while of the order of 50 ns for tw structures. The main RF deflector parameters are reported in Table 4.2 ([53]).
To study the beam loading processes for a tw structure it is necessary to introduce a reliable model of the single-passage wake and then to implement it in a tracking code to analyze the multi-passage effects [107].

[51] Actually the energy is sliglty different (150 MeV). Here the value of the energy considered in the simulations is reported.
[52] See note 70.
[53] The RF parameters such as the shunt impedance have been obtained scaling the parameters of the existing tw RF separators.

Table 4.2: Combiner ring RF deflectors parameters.

Frequency (f)	2.99855 [GHz]
Number of active cells (N_c)	10
Phase advance per cell (ph_c)	$2\pi/3$
Deflector length (L)	33 [cm]
Group velocity (v_g/c)	-0.0244
Filling time (τ_F)	46 [ns]
Shunt impedance per unit length (r_s)	17.35 [MΩ/m]
r_s/Q	1300 Ω/m
Input power (P_{inp})	1.5 MW
Deflection (ϕ_d)	5 [mrad]

4.2.1 Single and multi passage wake model

The design of the RF deflectors for the combiner ring has been done scaling existing structures (known as RF separators or Lengeler structures) already optimised for ion beam deflection [108,109]. These structures are disk loaded backward waveguides working on the so-called hybrid mode EH_{11}.
Referring to the Fig. 4.5, the e.m. field in the central region, in the case of small pitch approximation ($\lambda >> D$), negligible iris thickness ($t/D << 1$) and phase velocity equal to c, is given by the equations [73]:

$$\underline{E} = \left\{ \begin{array}{c} e_r = j\frac{E}{8}\left(k^2a^2 + k^2r^2\right)\cos(\vartheta) \\ e_\vartheta = -j\frac{E}{8}\left(k^2a^2 - k^2r^2\right)\sin(\vartheta) \\ e_z = \frac{E}{2}kr\cos(\vartheta) \end{array} \right\} \mathrm{e}^{\mathrm{j}\omega^*\left(t-\frac{z}{c}+\phi\right)} = \underline{\mathrm{e}}(r,\vartheta)\cdot \mathrm{e}^{\mathrm{j}\omega^*\left(t-\frac{z}{c}+\phi\right)}$$

$$\underline{H} = \left\{ \begin{array}{c} Z_0 h_r = j\frac{E}{8}\left(k^2a^2 - k^2r^2 - 4\right)\sin(\vartheta) \\ Z_0 h_\vartheta = j\frac{E}{8}\left(k^2a^2 + k^2r^2 - 4\right)\cos(\vartheta) \\ Z_0 h_z = -\frac{E}{2}kr\sin(\vartheta) \end{array} \right\} \mathrm{e}^{\mathrm{j}\omega^*\left(t-\frac{z}{c}+\phi\right)} = \underline{\mathrm{h}}(r,\vartheta)\cdot \mathrm{e}^{\mathrm{j}\omega^*\left(t-\frac{z}{c}+\phi\right)} \qquad (4.1)$$

where ω^* is the working frequency, $k=\omega^*/c$ and $Z_0=(\mu_0/\varepsilon_0)^{-1/2}$.

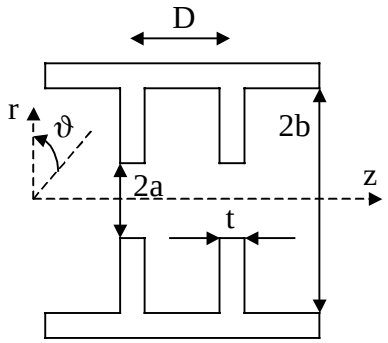

Fig. 4.5: sketch of a disk loaded waveguide

Using the expression of the Lorentz force acting on a particle of charge q that moves through the structure on the plane ϑ=0, with a velocity equal to c, one simply obtains[54]:

$$F_T = \mathrm{Re}\left(E_r - Z_0 H_\vartheta\right) = -q\frac{E}{2}\sin(\phi) \tag{4.2}$$

To evaluate the beam loading in the structure one has to consider both the interaction between the travelling charges and the transverse electric field E_r (beam loading in phase) and between the travelling charges and the longitudinal electric field E_z (beam loading 90° out-of-phase)[55].
The first contribution is very similar to the beam loading of a linac accelerating section and the deflection spread along the train can be estimated obtaining a quite small value in the CTF3 case.
The second contribution is of more concern because in the combiner ring the bunch pattern is such that at a certain time the deflector will be crossed by bunch trains off axis and with a phase separation of $2\pi/5$ generating a mutual perturbation mainly through the out-of-phase wake.
In order to calculate the wake field generated by the interaction between the travelling charges and the longitudinal electric field one has to refer to the general problem of modes excitation by an electric current J that flows through a waveguide [65].

[54] In the case of phase velocity different from c the equations of the field in the structure become more complicated [73] and, consequently, the expression of the transverse force itself.
[55] Also in the case of phase velocity different from c the longitudinal component of the electric field is 90° out-of-phase with respect to the transverse one.

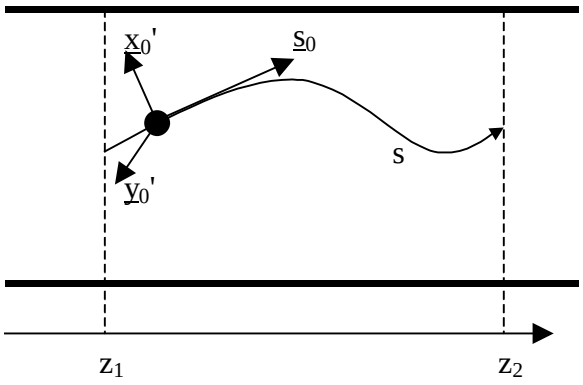

Fig. 4.6: sketch of a charge q moving in a waveguide

Considering a set of independent modes, the general propagating field in the structure can be written, in frequency domain as ([56]):

$$\underline{E}^{\pm} = \sum_{n=0}^{N} c_n^{\pm} \underline{e}_n e^{-j(\pm\beta_n)z} = \sum_{n=0}^{N} c_n^{\pm} \left(\underline{e}_{tn} \pm e_{zn} \underline{z}_0\right) e^{-j(\pm\beta_n)z}$$
$$\underline{H}^{\pm} = \sum_{n=0}^{N} c_n^{\pm} \underline{h}_n e^{-j(\pm\beta_n)z} = \sum_{n=0}^{N} c_n^{\pm} \left(\pm \underline{h}_{tn} + h_{zn} \underline{z}_0\right) e^{-j(\pm\beta_n)z} \tag{4.3}$$

where the signs "±" refer to the case of positive or negative phase velocities, respectively, N is the number of excited modes and $c_n^{\pm}$ and β_n are the amplitudes and the propagation constants of the n^{th} mode.
Assuming that a single particle passes through the structure of length L (Fig. 4.6) and considering only the interaction between the longitudinal component of the current and the deflecting mode, the coefficients c_1^{+} is given by the equation (Appendix A4.1):

$$c_1^{+}(\omega, z) = \frac{q}{4\Pi\ (\omega)} \int_z^L e_{z1}\left(\omega, \underline{r}(z')\big|_{\substack{particle \\ trajectory}}\right) e^{-j\omega\frac{z'}{c}} e^{j\beta\ (\omega)z'} dz' \tag{4.4}$$

where $r(z')|_{\text{particle trajectory}}$ is the transverse position of the particle along the structure, q is the charge and Π is the power flow along the structure[57]:

$$\Pi(\omega) = \frac{1}{2} \int_{\substack{transverse \\ section}} \underline{e}_{t1} \times \underline{h}_{t1} \cdot \underline{z}_0 dS \tag{4.5}$$

[56] The subscripts *t* and *z* indicate the transverse and the longitudinal components of the field ($\underline{e}_n$, $\underline{e}_z$ and $\underline{e}_{tn}$ are functions of the transverse coordinates and of the frequency).
[57] In the case of backward wave Π is negative.

The e.m. field of the excited mode can be calculated, in time domain, by a Fourier integral:

$$\underline{E}_1^+(t,z,r,\vartheta)=\frac{1}{2\pi}\int_{-\infty}^{+\infty}c_1^+(\omega,z)\underline{e}_{t1}(\omega,r,\vartheta)e^{-j\beta(\omega)z}e^{j\omega t}d\omega=\frac{1}{\pi}\mathrm{Re}\left[\int_0^{+\infty}c_1^+\cdot\underline{e}_{t1}\cdot e^{-j\beta z}e^{j\omega t}d\omega\right]$$

$$\underline{H}_1^+(t,z,r,\vartheta)=\frac{1}{2\pi}\int_{-\infty}^{+\infty}c_1^+(\omega,z)\underline{h}_{t1}(\omega,r,\vartheta)e^{-j\beta(\omega)z}e^{j\omega t}d\omega=\frac{1}{\pi}\mathrm{Re}\left[\int_0^{+\infty}c_1^+\cdot\underline{h}_{t1}\cdot e^{-j\beta z}e^{j\omega t}d\omega\right] \tag{4.6}$$

In order to calculate the coefficient c_1^+ and the corresponding e.m. field for all t and z one has to use the equations (4.4)-(4.6).
Unfortunately, these expressions are very difficult to manage numerically because all the quantities are frequency dependent and one has to compute a double integration (the first in the z' variable and the second in ω) in order to calculate the wake field generated by a single passage of a particle.
To evaluate the beam loading of a multiparticle passage, some approximated formulae can be introduced.

Approximation 1: linearization of the dispersion curve in a limited range of frequency

The typical dispersion curve of an RF deflector [73] is plotted in Fig. 4.7. The frequency f^* is the frequency at which the phase velocity (v_{ph}) is equal to c and it corresponds to the working frequency.
Tacking into account the expressions (4.4)-(4.6), it is easy to show that the major contribution, in time domain, to the deflecting force acting on a particle 90° out-of-phase from the leading one[58], comes from a small range of frequencies near f^* ([59]).
It is possible, therefore, linearize the previous expressions near the point (β^*,f^*) obtaining the following expressions for the coefficient $c_1^+(\omega,z)$ (see Appendix A4.2):

$$c_1^+(\omega,z)\cong\frac{q}{4\Pi_1(\omega^*)}\begin{cases}\displaystyle\int_z^L e_{z1}\left(\omega^*,\underline{r}(z')\Big|_{\substack{particle\\trajectory}}\right)e^{j\left(\frac{d\beta}{d\omega}\Big|_{\omega=\omega^*}\right)(\omega-\omega^*)z'}dz' & \omega\in\left[\omega^*-\frac{\Delta\omega}{2},\omega^*+\frac{\Delta\omega}{2}\right]\\ 0 & \text{elsewhere}\end{cases} \tag{4.7}$$

where the field $e_{z1}(\omega^*,r)$ is equal to e_z of eq. (4.1) and $[\omega^*-\Delta\omega/2,\ \omega^*+\Delta\omega/2]$ is a suitable interval near the center frequency f^* ([60]).

[58] It means that $t^*=T/4+hT$ where $T=1/f^*$ is the period of the wave in the deflector.
[59] In fact for a particle 90° out-of-phase from the leading one the real part of the coefficient $c_1^+(\omega)$ (for a fixed z) has a local maximum for $f=f^*$ (the exponential term oscillates for $f\neq f^*$) and also the deflecting force has a maximum when the particle is synchronous with the wave.

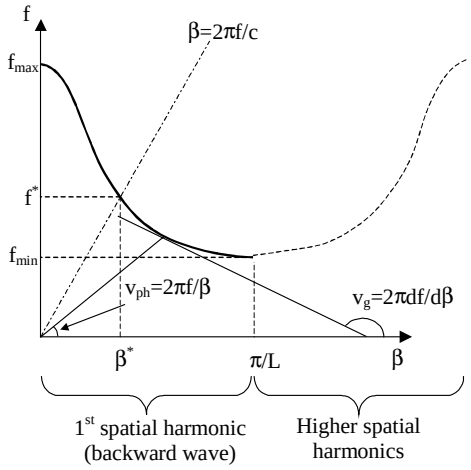

Fig. 4.7: sketch of a typical dispersion curve for a tw RF deflector

The expression for the electric field in the time domain becomes:

$$\underline{E}_1^+(t,z)=\frac{q}{2\pi\ \ \Pi_1(\omega^*)}\mathrm{Re}\left[\underline{e}_1(\omega^*)e^{j\omega^*\left(t-\frac{z}{c}\right)}\right]\int_z^L e_{z1}\left(\omega^*,\underline{r}(z')\Big|_{\substack{particle\\trajectory}}\right)\frac{\Delta\omega}{2}\mathrm{sinc}\left[\left(t-\frac{z-z'}{v_g}\right)\frac{\Delta\omega}{2}\right]dz' \tag{4.8}$$

where the field $\underline{e}_1(\omega^*)$ is equal to $\underline{e}$ of eq. (4.1) and sinc(x)=sin(x)/x.
The Lorentz force acting on a trailing particle that passes through the deflector after a time t^* from the leading one and that moves on the plane ϑ=0 is given by the formula[61]:

$$\begin{aligned}
&F_T(t^*,z)=q(E_r-Z_0H_\vartheta)=\\
&=-\frac{1}{\pi}\frac{q^2}{4\Pi_1\big|_{\omega=\omega^*}}E\sin(\omega^*t^*)\int_z^L e_{z1}\left(\omega^*,\underline{r}(z')\Big|_{\substack{leading\\particle\\trajectory}}\right)\frac{\Delta\omega}{2}\mathrm{sinc}\left[\left(t^*+\frac{z}{c}-\frac{z-z'}{v_g}\right)\frac{\Delta\omega}{2}\right]dz'\cong\\
&\underset{v_g<<c}{\cong}-\frac{1}{\pi}\frac{q^2}{4\Pi_1\big|_{\omega=\omega^*}}E\sin(\omega^*t^*)\int_z^L e_{z1}\left(\omega^*,\underline{r}(z')\Big|_{\substack{leading\\particle\\trajectory}}\right)\frac{\Delta\omega}{2}\mathrm{sinc}\left[\left(t^*-\frac{z-z'}{v_g}\right)\frac{\Delta\omega}{2}\right]dz'
\end{aligned} \tag{4.9}$$

[60] "Suitable interval" in order to have a good approximations of the exact expression for the field (11) in terms, for example of the deflecting force seen by a trailing particle.
[61] For the trailing particle $t=t^*+z/c$.

Approximation 2: linearization of the dispersion curve over an unlimited range of frequency

In this case the wake is given by the equation (4.8) when $\Delta\omega\rightarrow\infty$ obtaining[62]:

$$\underline{E}_1^+(t,z)=\frac{q|v_g|}{2\Pi_1|_{\omega=\omega^*}}\mathrm{Re}\left[\underline{e}_1(\omega^*)e^{j\omega^*\left(t-\frac{z}{c}\right)}\right]e_{z1}\left(\omega^*,\underline{r}(z-tv_g)\Big|_{\substack{\text{leading particle trajectoy translated in z-tv}_g}}\right) \tag{4.10}$$

$$F_T(t^*,z)=-\frac{q^2|v_g|}{4\Pi_1|_{\omega=\omega^*}}E\sin(\omega^*t^*)e_{z1}\left(\omega^*,\underline{r}\left(z-\left(t^*+\frac{z}{c}\right)v_g\right)\Big|_{\substack{\text{leading particle trajectoy translated in z-tv}_g}}\right)\cong$$

$$\underset{\frac{v_g}{c}<<1}{\cong}-\frac{q^2|v_g|}{4\Pi_1|_{\omega=\omega^*}}E\sin(\omega^*t^*)e_{z1}\left(\omega^*,\underline{r}(z-t^*v_g)\Big|_{\substack{\text{leading particle trajectoy translated in z-tv}_g}}\right) \tag{4.11}$$

Introducing the R/Q of the structure given by the formula (see par. 2.2):

$$\frac{R}{Q}=\frac{\left(\frac{E}{2}\right)^2\frac{v_g}{c}}{\Pi_1(\omega^*)k} \tag{4.12}$$

one obtains for the field the expression:

$$\underline{E}_1^+=-\frac{1}{2}q\omega^*\frac{R}{Q}kr(z-tv_g)\mathrm{Re}\left[\frac{\underline{e}_1(\omega^*)}{E/2}e^{j\omega^*\left(t-\frac{z}{c}\right)}\right]=$$

$$=-\frac{1}{2}q\omega^*\frac{R}{Q}\Big|_{eff}(r(z-tv_g))\mathrm{Re}\left[\frac{\underline{e}_1(\omega^*)}{E/2}e^{j\omega^*\left(t-\frac{z}{c}\right)}\right] \tag{4.13}$$

where:

$$\frac{R}{Q}\Big|_{eff}(r)=\frac{R}{Q}kr$$

[62] It is enough to remember that:

$$\lim_{\Delta\omega\longrightarrow\infty}\frac{\Delta\omega}{2}\mathrm{sinc}\left[\left(t-\frac{z-z'}{v_g}\right)\frac{\Delta\omega}{2}\right]=\pi|v_g|\delta(z'-(z-tv_g))$$

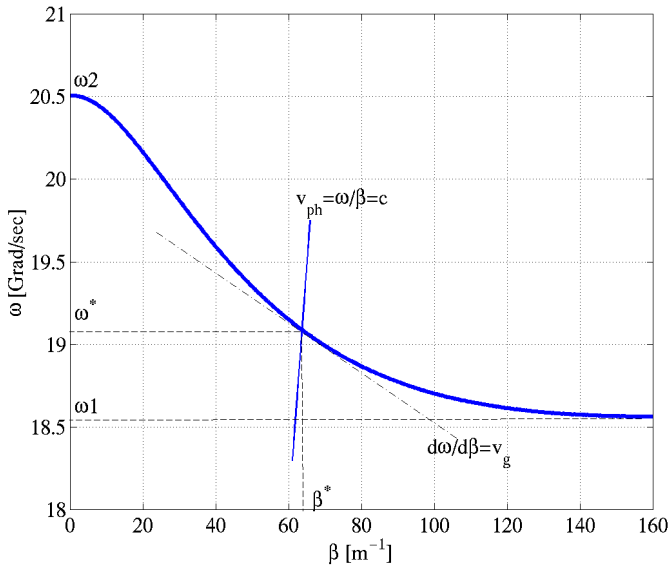

Fig. 4.8: dispersion curve for the considered RF deflector

and for the transverse force the expression:

$$F_T(t^*,z) \cong \frac{1}{2} q^2 \omega^* \frac{R}{Q} kr\left(z - t^* v_g\right)\sin\left(\omega^* t^*\right) = \frac{1}{2} q^2 \omega^* \left.\frac{R}{Q}\right|_{eff} \left(r\left(z - t^* v_g\right)\right)\sin\left(\omega^* t^*\right) \tag{4.14}$$

These expressions for the wake field and force correspond to what intuitively one could expect for the field generated by a passage of a particle in the RF deflector (see Appendix A4.3): an envelope of the field (or force) that follows the profile of the leading particle trajectory ([63]) and that rigidly translates along the structure with a negative group velocity equal to v_g and with a positive phase velocity equal to ω^*/c.
Assuming an RF deflector with the parameters[64] L=33 cm, a= 2.2 cm and b= 5.7 cm., one obtains the dispersion curve plotted in Fig. 4.8 ([65]).
By the previous equations it is possible to evaluate, in the correct case and in the approximated cases, the transverse field excited by a leading charge and probed by a trailing particle injected with a delay t^*.
Considering the leading particle trajectory of the type:

$$\underline{r}(z)\Big|_{\substack{leading\\particle\\trajectory}} = r_{in} + r'_{in}\, z + \frac{1}{2}\frac{\Delta r'}{L} z^2$$

[63] The field E_z is proportional to the displacement r of the particle from the axis of the structure.
[64] This parameters are scaled from that of [108,109] in order to have $f^* \cong 3$GHz. In the case of small pitch approximation ($\lambda >> D$) and negligible iris thickness ($t/D << 1$) the values of D and t do not affect the calculation of the dispersion curve [73].
[65] The analytical calculation gives for this structure $v_g = 0{,}058c$.

where r_{in} and r'_{in} are the initial injection position and angle and $\Delta r'$ is the deflection angle inside the deflector, the obtained transverse force[66] probed by a particle that enters in the structure after a time $t_1^*=T/4$ and $t_2^*=T/4+25T$ ([67]), are plotted in Fig. 4.10 in the case of trajectory 1 (Fig. 4.9). The correct result obtained by the numerical integration of eq. (4.6) (solid line) is compared with those obtained in the linear approximation of the dispersion curve in the pass-band interval of the EH_{11} mode $[\omega_1,\omega_2]$ (dashed line) and with those obtained by the linear approximation of the dispersion curve in an unlimited range of frequencies (dash-dotted line). In Figs. 4.11 and 4.12 the same quantities for the trajectory 2 and 3 of Fig. 4.9 are plotted.

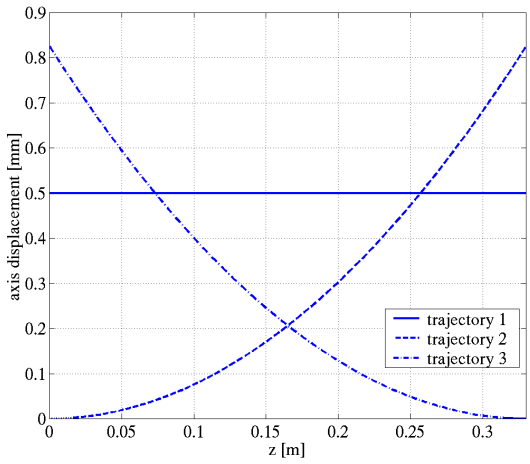

Fig. 4.9: trajectories of the leading particle:
trajectory 1 (r_{in}=0.5 mm, r'_{in}=0 and $\Delta r'$=0)
trajectory 2 (r_{in}=0 mm, r'_{in}=5 mrad and $\Delta r'$=5 mrad)
trajectory 3 (r_{in}=0.825 mm, r'_{in}=-5 mrad and $\Delta r'$=5 mrad).

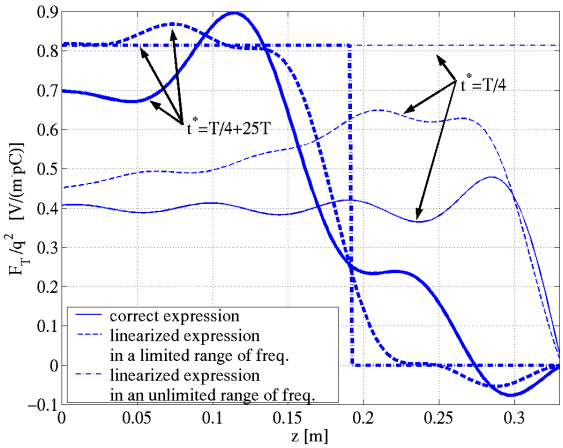

Fig. 4.10: transverse force probed by a trailing particle
(trajectory 1 of the leading particle).

[66] The force is calculated on the axis of the structure. More precisely, as shown in the eq. (4.9) and (4.14), in the approximated cases the transverse force does not depend on the displacement of the trailing particle. Nevertheless, considering the exact field distribution and the correct calculation (4.4-6), there is a force dependence due to the transverse position of the trailing particle.

[67] For this structure the analytical calculation gives a filling time $\tau_f=L/v_g\cong 50T$.

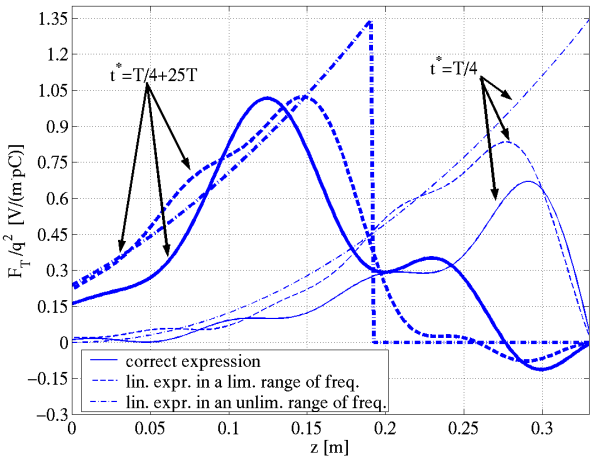

Fig. 4.11: transverse force probed by a trailing particle (trajectory 2 of the leading particle).

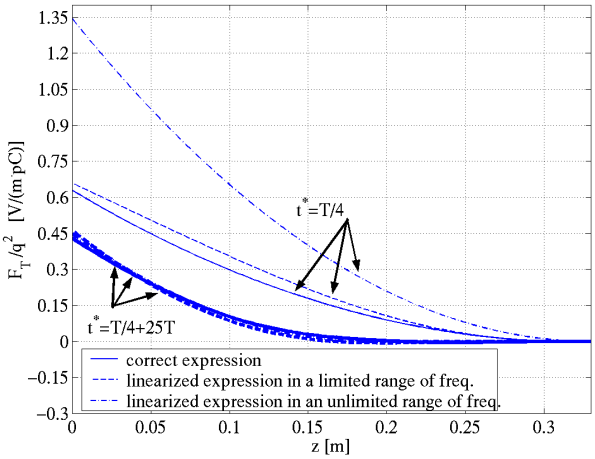

Fig. 4.12: transverse force probed by a trailing particle (trajectory 3 of the leading particle).

Introducing the transverse wake probed by a trailing particle that enters in the structure after a time $t_n^*=T/4+nT$ defined as:

$$w_{\perp n} = \frac{1}{q^2}\int_0^L F_T(t_n^*, z)dz \tag{4.15}$$

one obtains the results plotted in Figs. 4.13, 4.14 and 4.15 for the three different trajectories, respectively.

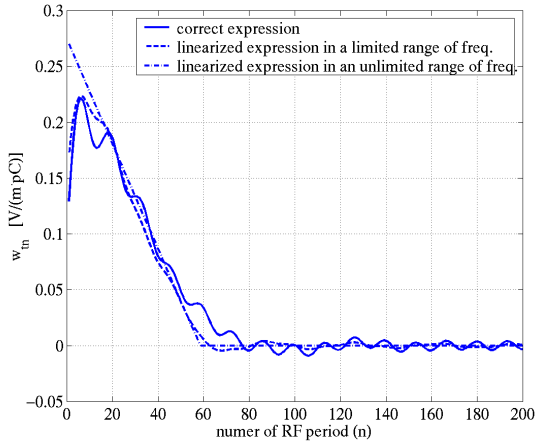

Fig. 4.13: transverse wake probed by a trailing particle that enters in the structure after a time t_n^*=T/4+nT (trajectory 1 of the leading particle)

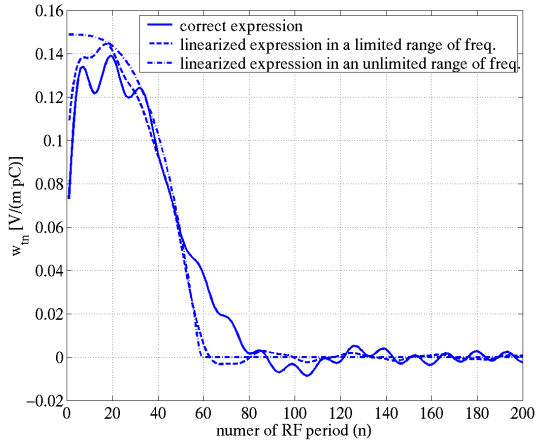

Fig. 4.14: transverse wake probed by a trailing particle that enters in the structure after a time t_n^*=T/4+nT (trajectory 2 of the leading particle)

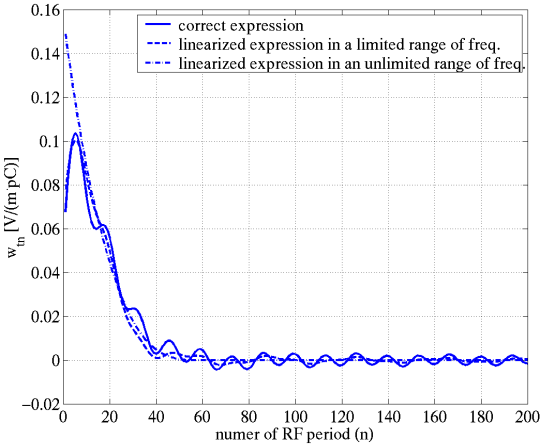

Fig. 4.15: transverse wake probed by a trailing particle that enters in the structure after a time t_n^*=T/4+nT (trajectory 3 of the leading particle)

In the case of an infinite train of bunches spaced in time by T and with the same trajectories inside the deflector, the density current is given by:

$$\underline{J}(t) = q\underline{s}_0(s)\sum_{i=-\infty}^{\infty}\delta\left(t-\frac{s}{c}+iT\right)\delta(x')\delta(y') \tag{4.16}$$

that in the frequency domain becomes:

$$\underline{J}(\omega) = q\underline{s}_0(s)\delta(x')\delta(y')\omega^* e^{-j\omega\frac{s}{c}}\sum_{n=-\infty}^{\infty}\delta(\omega-n\omega^*) \tag{4.17}$$

where $\omega^*=2\pi/T$.

In order to evaluate the coefficient $c_1^+(\omega,z)$ one has to remember that the CTF3 RF deflectors work at ~3 GHz and that the dispersion curve for the mode EH_{11} for these structures has a pass-band of the order of few hundred of MHz (see Fig. 4.8). Furthermore, the trains of bunches have a spectrum with a distance (1/T) between the δ in eq. (4.17) that is bigger or equal to ~3 GHz (see Table 4.1). For this reasons the coefficients $c_1^+(\omega,z)$, in the case of a train of bunches, can be simply obtained substituting the term $e^{-j\omega z/c}$ in eq. (4.4) with the spectrum (4.17), obtaining for parabolic trajectories[68]:

$$\begin{aligned} c_1^+(\omega,z) &= \frac{q\omega^* Ek}{8\Pi_1\big|_{\omega=\omega^*}}\delta(\omega-\omega^*)\int_z^L\left(r_{in}+r'_{in}\,z'+\frac{1}{2}\frac{\Delta r'}{L}z'^2\right)dz' = \\ &= \frac{q\omega^* Ek}{8\Pi_1\big|_{\omega=\omega^*}}\delta(\omega-\omega^*)\left[r_{in}z'+\frac{1}{2}r'_{in}\,z'^2+\frac{1}{6}\frac{\Delta r'}{L}z'^3\right]_{z'=z}^{z'=L} \end{aligned} \tag{4.18}$$

The electric field is, in this case, given by:

$$\underline{E}_1^+(t,z) = \frac{1}{8\pi}\frac{q\omega^* Ek}{\Pi_1\big|_{\omega=\omega^*}}c(z)\mathrm{Re}\left[\underline{e}_1(\omega^*)e^{j\omega^*\left(t-\frac{z}{c}\right)}\right] \tag{4.19}$$

where:

$$c(z) = \left[r_{in}z'+\frac{1}{2}r'_{in}\,z'^2+\frac{1}{6}\frac{\Delta r'}{L}z'^3\right]_{z'=z}^{z'=L} = r_{in}(L-z)+\frac{1}{2}r'_{in}\left(L^2-z^2\right)+\frac{1}{6}\frac{\Delta r'}{L}\left(L^3-z^3\right) \tag{4.20}$$

and the transverse force seen by a trailing particle of charge q that moves through the deflector after a time t^*+hT is given by:

$$F_T(t^*,z) = -\frac{q^2kE^2}{8T\Pi_1\big|_{\omega=\omega^*}}\sin(\omega^* t^*)c(z) \tag{4.21}$$

[68] In practice the spectrum (4.17) samples the eq. (4.4) at the working frequency ω^*.

The easiest way to calculate the wake field in the multi-bunch regime in the case of linearized dispersion curve over an infinite range of frequencies, is to make a numerical calculation with rigid profile fields that propagate in the structure as pointed out previously.
The obtained results are plotted in Figs. 4.16, 4.17 and 4,18 for a trailing particle that enters in the structure out of phases with respect to the particles of the infinite train. Also in this case the correct solution (dashed line) is compared with the solution obtained by the linearized approximation over an unlimited range of frequencies (solid line) ([69]).

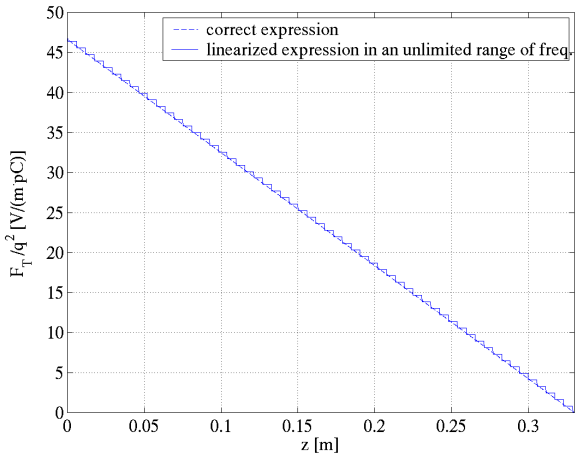

Fig. 4.16: transverse force seen by a 90° out of phase particle
in the case of multibunch regime (trajectory 1 of the train of bunches).

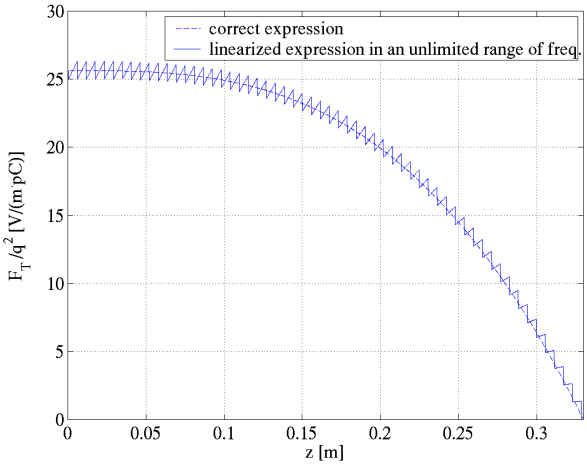

Fig. 4.17: transverse force seen by a 90° out of phase particle
in the case of multibunch regime (trajectory 2 of the train of bunches).

[69] In the case of multibunch regime there are not differencies between the correct solution and the case of linearaized dispersion curve in a limited range of frequencies.

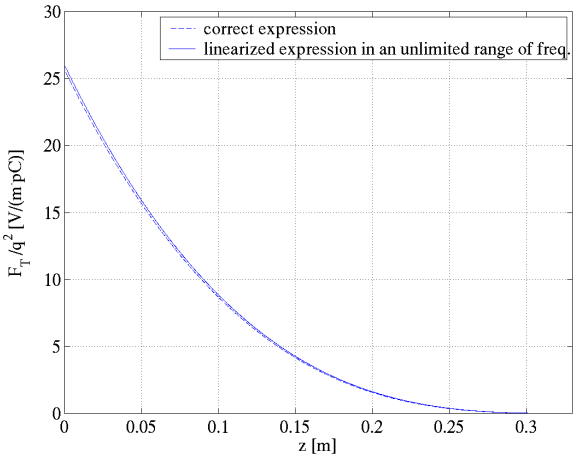

Fig. 4.18: transverse force seen by a 90° out of phase particle
in the case of multibunch regime (trajectory 3 of the train of bunches).

4.2.2 Tracking code results

The three different models for the wake field produce stationary multibunch forces along the deflector that are almost identical even if, in the single passage, the force probed by the particle is different in the three cases. The explanation is that the multibunch steady solution is the response to a "monochromatic" excitation and the details of the dispersion curve out of resonance are not relevant in this case.
Moreover, the integrated force (wake), also in the single passage, is very similar in the three cases.
For these reasons, the model of the single passage wake fields that has been adopted to study the multibunch regime with a tracking program, is the simplest one (Approximation 2).
The tracking code scheme is sketched in Fig. 4.19. Each bunch, represented as a macroparticle, enters in the 1st deflector with some horizontal initial conditions (x_{in},x'_{in}), interacts with the main RF deflecting field and with the wake left by the bunches ahead, contributes to the wake and exits the deflector with some new horizontal conditions (x_{out}, x'_{out}). The bunch, then, is transported to the other deflector by the transport matrix M_{21} ([70]), interacts with the RF field and wakes of this second device and so on.

[70] It can be shown [110] that, in a ring, the output position and angle at a certain section of the ring can be expressed as a function of the input position and angle of the section in the form:

$$\begin{pmatrix} x_o \\ x'_o \end{pmatrix} = \overbrace{\begin{pmatrix} \cos\phi + \alpha\sin\phi & \beta\sin\phi \\ -\gamma\sin\phi & \cos\phi - \alpha\sin\phi \end{pmatrix}}^{M} \begin{pmatrix} x_i \\ x'_i \end{pmatrix}$$

the matrix M is are called transport matrix and the quantity α, β, γ, ϕ (related to the magnets configuration of the ring) are called optical function (α, β, γ) and phase advance between the two points (ϕ), respectively.

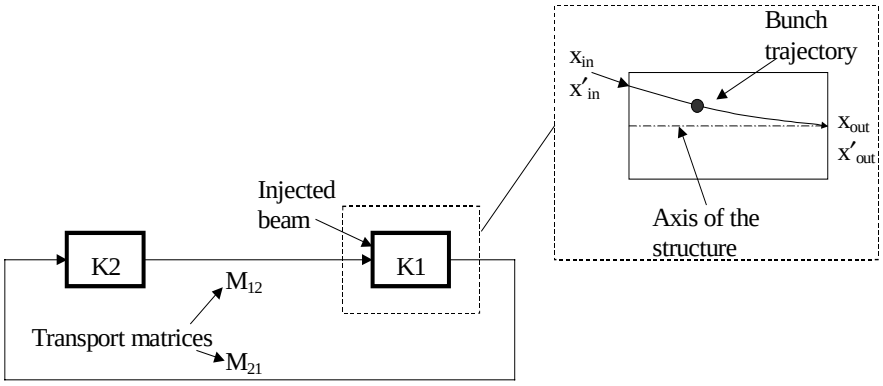

Fig. 4.19: tracking code scheme.

At the end of the merging process (five trains and five turns) each macroparticle ends up with certain horizontal conditions (x_{out}, x'_{out}) corresponding to a certain value of the Courant-Snyder invariant[71] I_o associated with the motion of the bunch center of mass.
The tracking allows studying, therefore, the distribution of the final values of the Courant-Snyder invariants for the all bunches, and its dependence on the deflector wakes, injection errors, ring optical function and phase advance.

Perfect injection of the 5 trains

This is the case of bunch trains injected with the initial conditions that perfectly match the main deflecting field of the deflectors so that, if there is no wake, all the bunches would end up on the combiner ring design orbit. These conditions correspond to the point x_{in}= 0.825 mm and x'_{in}=-5 mrad of the phase space at the injection plane.
The 1st train makes the first revolution alone, and there are no bunches interacting with its out-of-phase wake. During the second revolution, there is the contemporary presence of the 1st and 2nd trains which cross the deflectors with some horizontal displacement. The two trains are interleaved with a separation of $2\pi/5$ RF and their bunches interact through the out-of-phase wake. This generates a first perturbation that deviates the bunches from their ideal trajectories. Similar processes take place during the next interleaving phases and, when the 5 trains are finally merged in a single one, the bunches aquire a certain spread in the horizontal phase space.
A plot of the position and angle of the bunches with respect to the nominal orbit taken at the 1st deflector output at the end of the merging process is shown in Fig. 4.20. The corresponding plots of the bunch in the phase space and of the Courant-Snyder

[71] Considering a fixed longitudinal position in a storage ring, a certain macroparticle at the position (x,x') of the transverse phase space oscillates, turn by turn, around the same ellipse (this is propeirly true if one neglect the synchrotron radiation damping that is, however, negligible if one consider few turns in the ring). The equation of the ellipse is given by [110]:

$$\gamma x^2 + 2\alpha x x' + \beta y'^2 = I$$

and the quantity I is called the Courant-Snyder Invariant. The area of the ellipse is π times I.

invariant are shown in Figs. 4.21-4.22. In the tracking code the transport matrices M_{12} and M_{21} are given by the nominal combiner ring optics [104].
The Figs. 4.20-4.22 represent the so-called "systematic effect" of the wake field since the perturbations in the final bunches transverse positions are not driven by initial injection errors. The average and maximum values of the Courant-Snyder invariants are respectively $I_{oav} \cong 8 \cdot 10^{-3}$ mm mrad $I_{omax} \cong 4.2 \cdot 10^{-2}$ mm mrad.
The spread of the macroparticle Courant-Snyder invariant values caused by the systematic effect is a small fraction of the CTF3 bunch design emittance[72] ($\varepsilon \cong 0.4$ mm mrad @180 MeV).

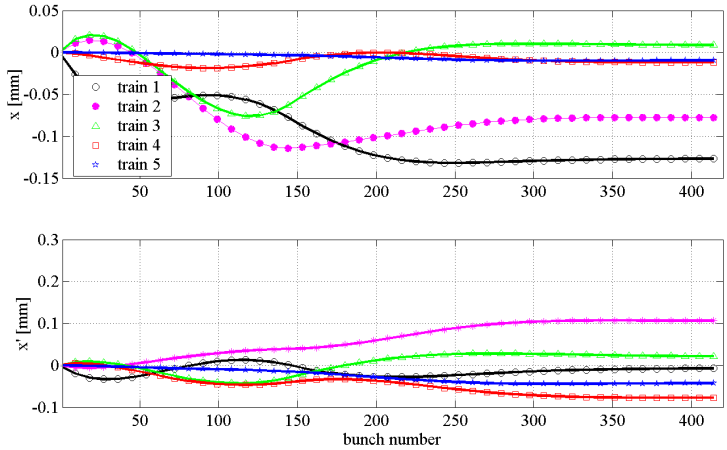

Fig. 4.20: positions and angles of the bunches with respect to the nominal orbit taken at the 1st deflector output at the end of the merging process.

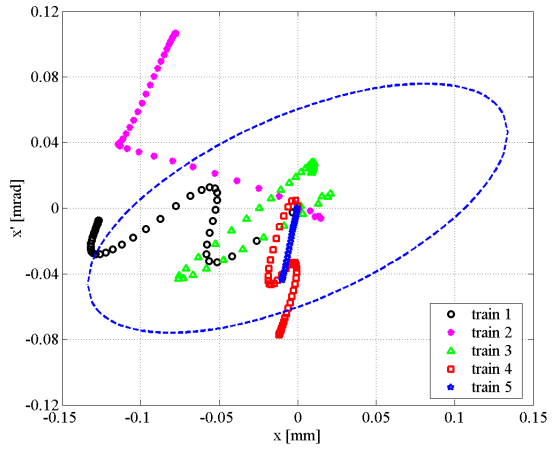

Fig. 4.21: bunches in the transverse phase space after the recombination process: "sistematic effect".

[72] The emittance of a single bunch is defined as the area occupied in the phase space x,x' by a certain fraction of the bunch particles divided by π [111]. This means that each point in the plot of Fig. 4.21 should be considered as a distribution function with an area equal to $\varepsilon\pi$.

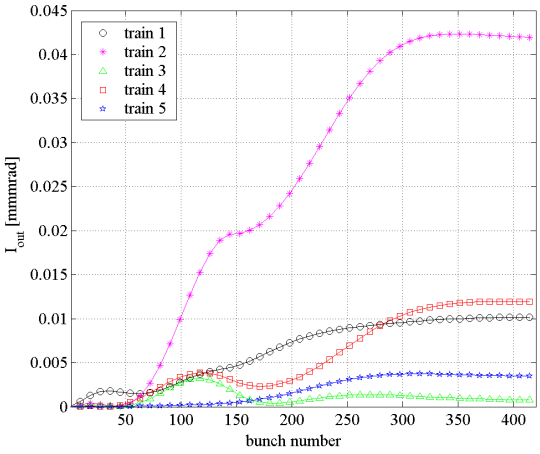

Fig. 4.22: Courant-Snyder invariant of the bunches after the recombination process.

Errors in the injection of the trains

Referring to the case of an equal injection error for all the bunches of the 5 incoming trains[73], the build-up mechanism for the final invariant spread is just the same as that described previously even if, in this case, the initial errors can drive the process to larger final errors.

The bunch trains footprints in the horizontal phase space at the output of the 1st deflector for an injection offset of 1 mm and for an injection error of 0.633 mrad in angle (both corresponding to an initial value of the Courant-Snyder invariant I_{in}=0.716 mm mrad[74]) are reported in Fig. 4.23.

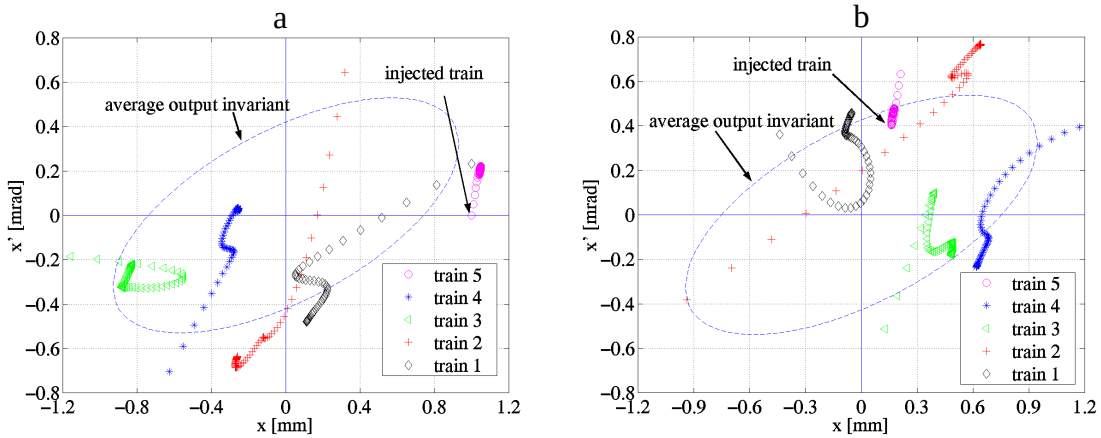

Fig. 4.23: bunch train in the horizontal phase space for an injection offset of 1 mm (a) and for an injection error of 0.633 mrad in angle (b)

[73] This is the case, for instance, if one assumes that the error can fluctuate only from pulse to pulse due to some jitter in the beam transport.

[74] The invariant is calculated with respect to the perfect injection case x=0.825 mrad x'=5 mrad, i.e., the position (0,0) is the position of perfect injection.

Performing different simulations with different initial conditions it may be seen that, in general, the maximum value I_{omax}, the average value I_{oav} and the standard deviation σ_{Io} of the Courant Snyder invariants of the final distributions are not constant for a given initial value I_{in} of the invariant, but, due to the nature of the wake, depend also on the position and angle of the incoming trains.
Considering all the possible injection errors (Fig. 4.24) for a given I_{in} and calculating the maximum and average values for the corresponding final distributions, one obtains the result shown in Fig. 4.25 where for any possible error the average invariant with the relative error bars is reported.
For any given initial value I_{in}, there are some errors that give the largest I_{omax} value (I_{pomax}), and the largest I_{oav} value (I_{poav}).
The plots of I_{pomax} and I_{poav} (this last including the ±rms error-bar) for I_{in} ranging from 0 to 2 mm mrad are shown in Fig. 4.26.
It may be seen that, for the optics parameters considered and with the exception of the $I_{in}\cong 0$ case, it is always $I_{poav}<I_{in}$, which means that, on the average, the deflectors wake gives a sort of "cooling" of the Courant-Snyder invariant of the bunch center of mass. On the other hand, from the same figure one has $I_{pomax}/I_{in}<2.6$, and the magnification factor is reduced to about 1.5 for all bunches staying within one standard deviation above the average (≈70% of the bunches).
The previous results have been obtained considering the nominal betatron phase advance between the deflector 1 and 2. Different phase advances ϕ give different amplification factors and the minimization of the ratios I_o/I_{in} is one of the criteria for the choice of this ring optical parameter.
As an example the ratios I_{omax}/I_{in} and I_{oav}/I_{in} are reported in Fig. 4.27 in the case of an injection error caused by a pure displacement of 1 mm, for various values of the betatron phase advance.
The nominal phase advance corresponds to 262°, which is close to the minimum. Modifications of the phase advance in the range of ±10° does not significantly change the scenario. Anyway, some tunes outside the range shown in Fig. 4.27 may give magnification factors larger than 10.

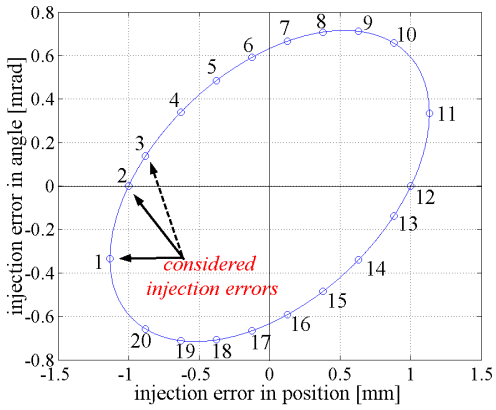

Fig. 4.24: possible injection errors in the horizontal input phase space.

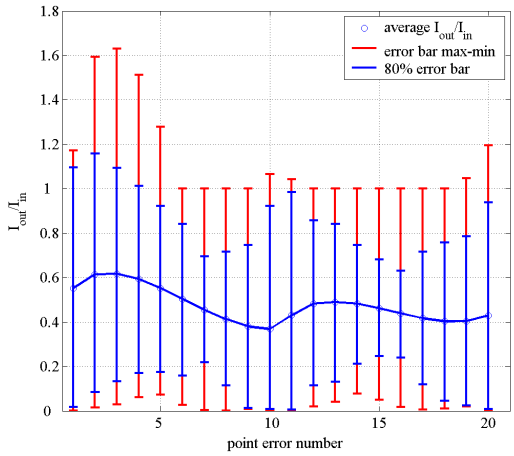

Fig. 4.25: average invariant with the relative error bars for any possible injection error.

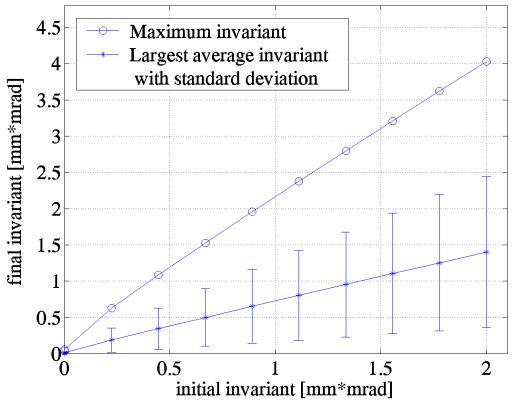

Fig. 4.26: maximum and average values of the final invariant as a function of the input invariant.

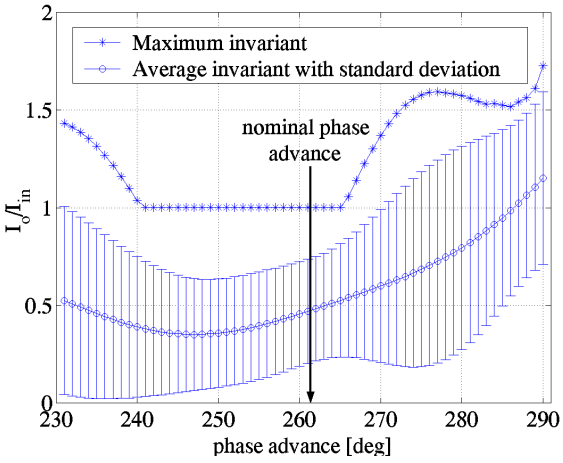

Fig. 4.27: ratios I_{omax}/I_{in} and I_{oav}/I_{in} in the case of an injection error caused by a pure displacement of 1 mm for various values of the betatron phase advance.

Simulations results including a finite bunch length

The design bunch length for CTF3 is between 1.5 and 2.5 mm and it is a very important parameter to be controlled in order to have a good efficiency in the power generation. In fact, in frequency domain, the spectrum of the bunches is given by the eq. (1.93) and an excessive increase of the bunch length may give a loss of power at the 30 GHz due to the exponential factor $\exp(-\omega^2\sigma_z^2/2c^2)$. Furthermore, as illustrated in the following, an increase of the bunch length can give loss of current due to the fact that the tails of the bunch may grow in terms of Courant Snyder invariant because of the finite wave length of the RF deflectors field and wakes.
On the contrary, an increase of the bunch length, reducing the charge density, may give, at high bunch current, a reduction of the collective effect in terms of coherent synchrotron radiation and interaction with the short range wake field [104].
The value of σ_z=3 mm seems to be a maximum acceptable value for the bunch length.
The effects of the beam loading in the RF deflectors considering a finite bunch length can be simulated dividing the bunches into slices (Fig. 4.28). Each slice can be considered as a macroparticle and the complete simulation can be performed.
Assuming a perfect injection of the trains and the absence of the wake field in the deflectors, one obtains the transverse bunch slice output positions after the recombination plotted in Figs. 4.29a and b.
In this case, also, there is a certain increase of the bunch emittance[75] calculated with respect to the central slice of the bunch. Nevertheless it is a negligible effect if compared with the bunch design emittance (Table 4.3).

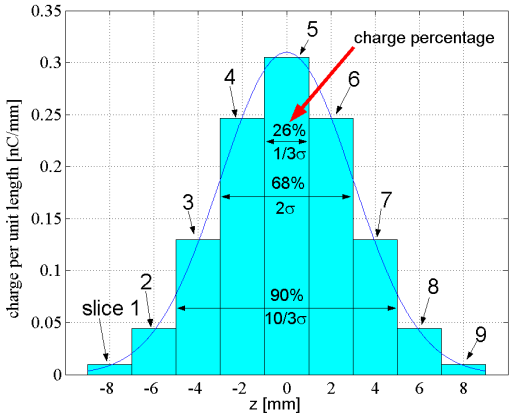

Fig. 4.28: discretization of the bunch in a finite number of slices.

[75] The r.m.s emittance of a the bunch with respect to central slice can be defined as [111]:

$$\varepsilon = \sum_{slices} \sqrt{\frac{q_i \Delta d_i^2}{Q_T}}$$

where the quantities Δd_i are the distances in the horizonthal phase space between the slices and the central one, q_i is the charge of the slice i and Q_T is the total charge of the slices.
The r.m.s. emittance is an indication of the spread of the slices around the central one in the phase space (it is equal to zero at the input of the deflector) and can be direcly compared with the emittance of the beam or with the Courant Snyder invariant.

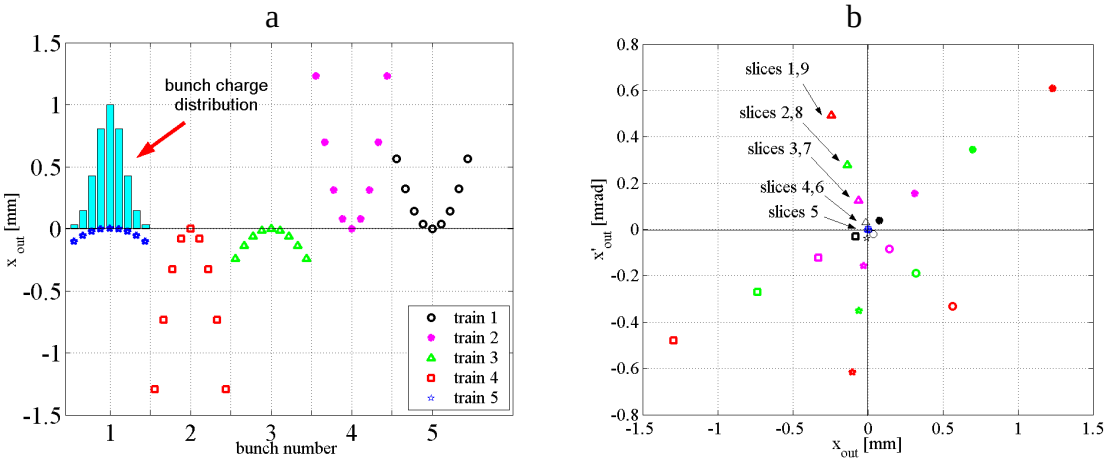

Fig. 4.29: transverse bunch slice output positions (a) after the recombination (perfect injection of the trains and absence of the wake field); (b) slices in the phase space

Table 4.3: r.m.s. emittance of the bunches referred to the central slice after the recombination process and without wake in the deflectors

TRAIN NUMBER	r.m.s. emittance [mm*mrad]
Train 1	0.043
Train 2	0.173
Train 3	0.027
Train 4	0.143
Train 5	0.015

The effect of the beam loading is shown in Figs. 4.30a and b.
In this case a nominal phase advance has been assumed and the output position and angle of the slices for the whole trains has been found. In Fig. 4.30b the output invariant of the central slices of bunches are reported as a function of the bunch number. Comparing this figure with the Fig. 4.22 one can observe that for the central slice of the bunches the output invariants are comparable with those obtained without considering the bunch length.
The r.m.s.emittances with respect to the central slice are reported in Fig. 4.31. In this case, also, the increase of the emittance is negligible if compared with the bunch design emittances.
The output invariants of the central slices and the r.m.s emittances have been calculated in the case of different injection errors.
The results are plotted in Figs. 4.32a and b. The beam loading effects do not change, for the central slices of bunches the scenario discussed in the case of $\sigma_z=0$. The r.m.s emittance growth due to the finite bunch length is, in the worst case, equal to the design emittance and can be considered a controllable effect.

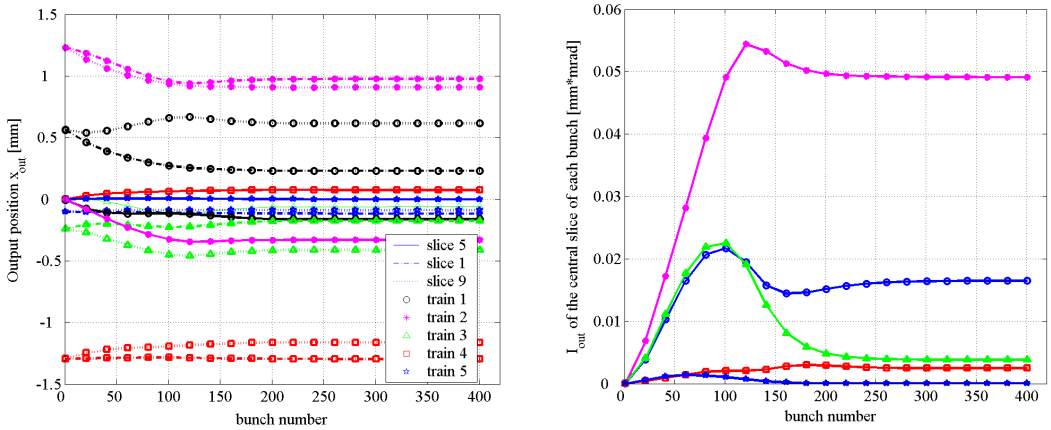

Fig. 4.30: (a) output position of the slices as a function of the bunch number without injection errors and wake fields; (b) output invariant of the central slices of bunches.

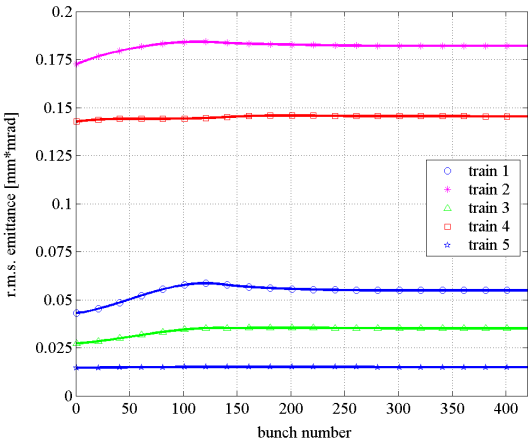

Fig. 4.31: r.m.s.emittances with respect to the central slice.

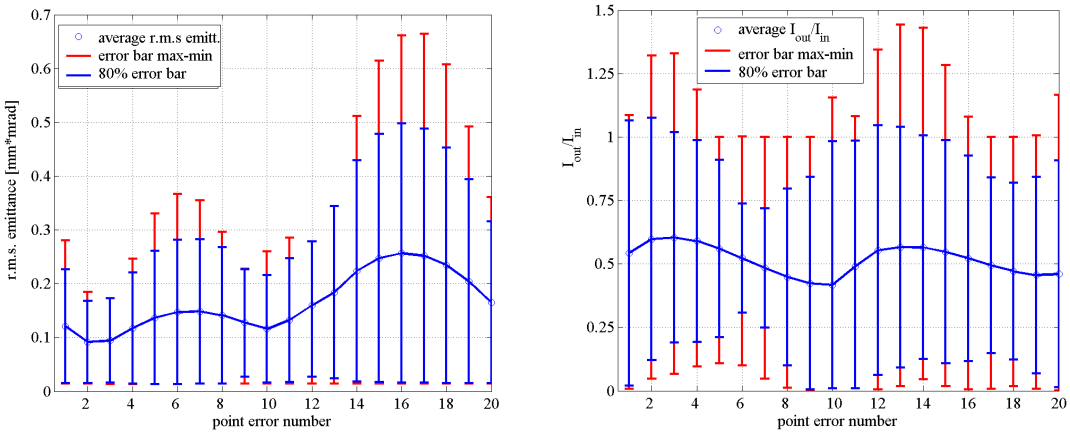

Fig. 4.32: output invariants for the central slices and the r.m.s emittances for different injection errors.

4.3 RF Deflector Design

The design of the RF deflectors has been done scaling to the CTF3 working frequency (2.99855 GHz) the dimensions of CERN RF separators with a reduced number of cells [112].
These are disk-loaded backward waveguides working in the $2\pi/3$ EH_{11} hybrid mode already optimized for beam deflection. $2\pi/3$ mode means that, at the working frequency, the phase advance per cell is $2\pi/3$.
The final 10 cells structure is sketched in Fig. 4.33a.
As described in the following the design of the single cell has been aimed to find the correct cell dimensions in order to have the correct phase advance at the working frequency f_{RF}. In parallel, the design of the coupler cells has been aimed to minimize the reflection coefficient at the input port in order to obtain the maximum transmitted power and the minimum reflection coefficient.

4.3.1 Single cell design

With the electromagnetic code MAFIA the scaled single cell 2D profile has been simulated and the local sensitivity of the $2\pi/3$ mode frequency with respect to the variation of each cell dimension has been computed (Table 4.4).
The $2\pi/3$ EH_{11} mode can degenerate in 2 frequencies of orthogonal polarity. The vertical one has been shifted far enough from the operating mode (horizontal polarity) in order to avoid its excitation by the RF generator or by the beam itself. This has been achieved by means of 2 longitudinal rods crossing off-axis the cells as shown in Fig. 4.33b.

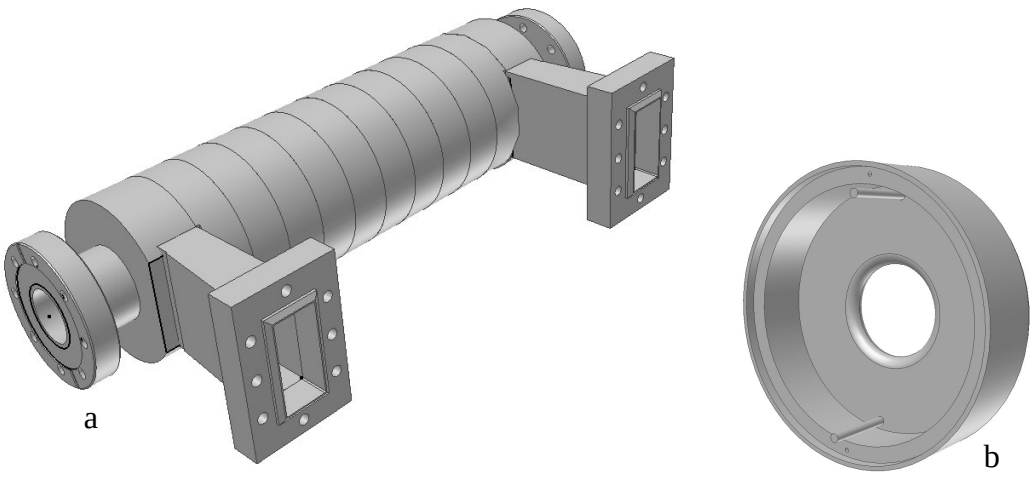

Fig. 4.33: sketch of the final 10 cells RF deflector structure.

Table 4.4: local sensitivity of the deflecting mode frequency vs. cell dimensions

Dimension	Sensitivity
A	$\partial f/\partial a$=-13.2 MHz/mm
B	$\partial f/\partial b$ =-49.7 MHz/mm
C	$\partial f/\partial t$ = 2.9 MHz/mm
D	$\partial f/\partial d$ =1.2 MHz/mm

Table 4.5: final dimensions of the cell and RF deflectors parameters

Final cell dimensions	a= 21.43 mm
	b = 56.01 mm
	d = 33.33 mm
	t = 9.53 mm
RF deflector parameters (HFSS and MAFIA)	f=2.9986 [GHz] (MAFIA) 2.9983 [GHz] (HFSS)
	v_g=-0.0237*c (MAFIA)
	R/Q=1460 [Ω/m] (HFSS)

The frequency shift of both polarities, caused by the break of the azimuthal symmetry due to the rods, has been calculated with the code HFSS. The obtained shifts have been of ~50 MHz for the vertical polarity and of ~80 KHz for the operating horizontal mode.

Finally, the frequency of the $2\pi/3$ mode has been calculated with HFSS considering the 3D cell profile with rods. Since the code uses a regular polygon to model a circle or an arc, depending on the starting vector for faceting, the polygon can be entirely inside or outside the arc to be modeled. This error can be in principle reduced increasing the number of faces but, unfortunately, this gives numerical and convergence problems. In order to control this systematic error, in the final single cell simulations the radius of curvature have been properly corrected in order to have the corresponding polygon areas equal to those of the ideal circles[76]. The final dimensions of the single cell are reported in Table 4.5 with the $2\pi/3$ mode frequencies obtained by HFSS (3D cell with rods) and by MAFIA (2D cell without rods).

[76] Simulating some known resonating structures and comparing the results with analytical calculations it can be shown that the error in the frequency calculation is reduced by a factor of 10.

In this case a precision of ~500 KHz in the frequency of the $2\pi/3$ mode is satisfactory. In fact, as shown in Appendix A4.4 an error in the resonant frequency of the mode corresponds to an error in the phase velocity of the field given by the equation:

$$\frac{\Delta v_{ph}}{c} = \frac{c}{|v_g|}\frac{\Delta\omega}{\omega} \tag{4.22}$$

And the effective maximum transverse kick normalized to the nominal one is given by:

$$\frac{\int_0^L F_\perp dz}{\int_0^L F_{\perp nom} dz} = \mathrm{sinc}\left(\frac{L}{2}\frac{\Delta\omega}{|v_g|}\right) \tag{4.23}$$

In Fig. 4.34 the transverse kick normalized to the nominal one is plotted as a function of the frequency error. One can immediately observe that an error of 1 MHz gives a reduction of the transverse kick of~0.4%.
The R/Q has been calculated following the formula (4.12) where E/2 is the amplitude of the fundamental harmonic of the deflecting field.
The dispersion curve of the deflecting mode obtained by MAFIA is plotted in Fig. 4.35 and the absolute value of the electric and magnetic fields in the 3D structure simulated by HFSS are plotted in Fig. 4.36.

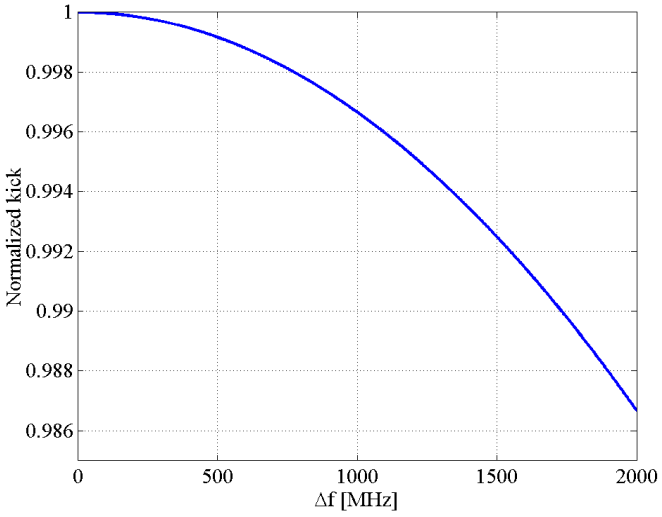

Fig. 4.34: transverse kick normalized to the nominal one as a function of the cell resonant frequency error.

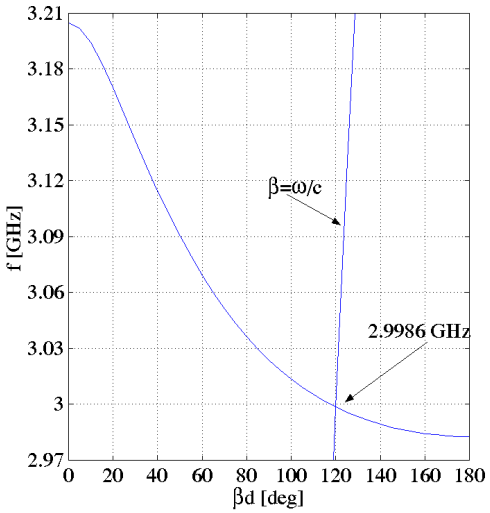

Fig. 4.35: dispersion curve of the deflecting mode obtained by MAFIA.

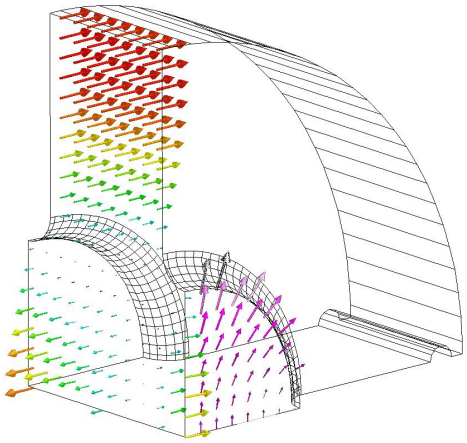

Fig. 4.36: absolute values of the electric and magnetic fields in the 3D structure simulated by HFSS.

4.3.2 Coupler simulations

In order to evaluate the coupler efficiency the whole structure has to be simulated. Since the structure is symmetric with respect to the horizontal plane the volume to simulate can be reduced considering one half of the structure and a perfect magnetic plane (Fig. 4.37a).
To reduce, further, the volume to simulate it is possible to do the following considerations. The structure shown in Fig 4.37b can be considered as a symmetric structure with respect to the longitudinal plane. The excitation at the input port can be considered, therefore, as the superposition of the two excitations shown in Fig. 4.38. In the “odd” case the longitudinal symmetric plane is a short circuit while in the “even” case it is an open circuit.

The total S_{11} can be calculated, therefore, as a sum of the S_{11} obtained in the two simulations.
The obtained absolute value of the reflection coefficient ($|S_{11}|$) at the device input port is plotted versus frequency in Fig. 4.39b while the HFSS simulated structure is shown in Fig, 4.39a with the magnetic field components in the "even" case.
As shown in Fig. 4.39b it is evident that, at the working frequency 2.99855 GHz, just few percent of the input power is reflected.

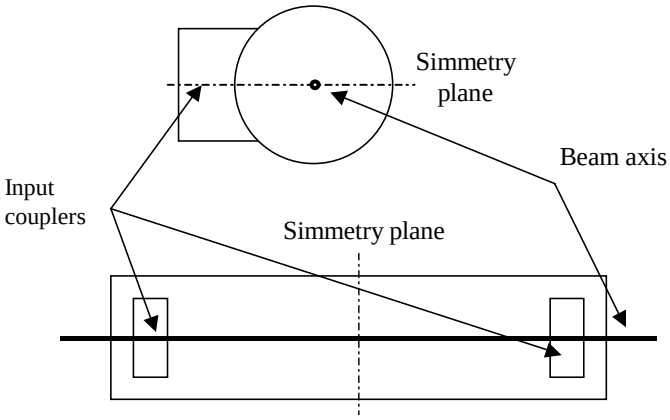

Fig. 4.37: symmetries in the RF deflector

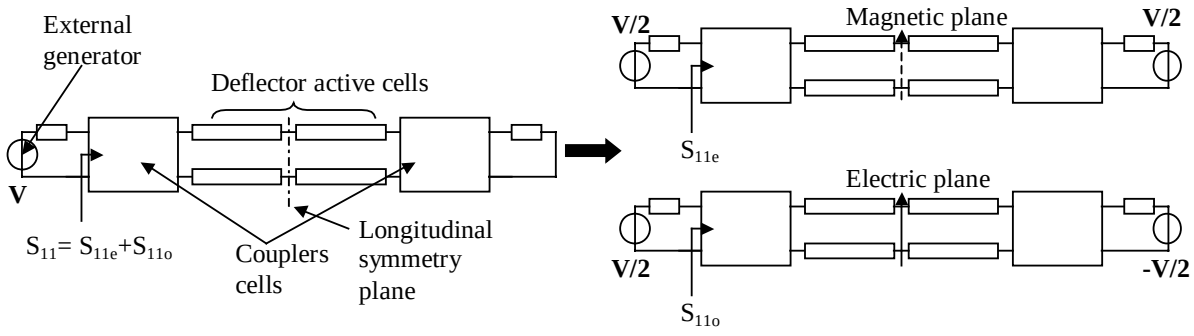

Fig. 4.38: equivalent circuit of the RF deflector excitation.

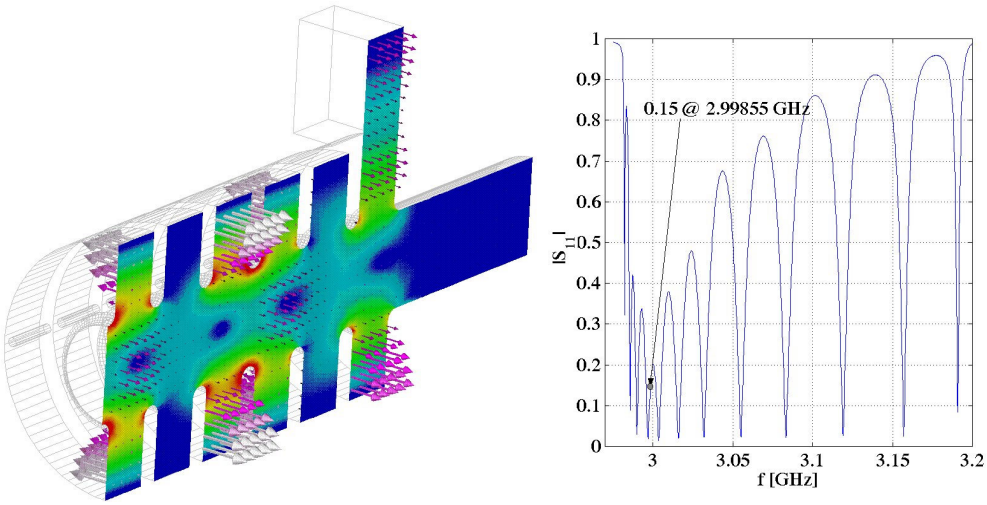

Fig. 4.39 (a) HFSS simulated structure; (b) absolute value of the reflection coefficient obtained by HFSS.

4.4 RF Deflector Measurements

The deflectors have been made of OFHC high quality copper using hard soldering (brazing) technique well mastered in production processes of accelerating structures in S band. Soldering has been done in steps, in hydrogen atmosphere. The single cells of the deflectors have been produced in the form of cups (Fig. 4.33b).
Before the production of the final deflectors, an aluminum full-scale prototype has been fabricated in order to verify the validity of the performed calculations.
The measurements (single cell resonant frequency, dispersion curve) have confirmed the simulation results for the two different polarities.
The deflector components have been, then, fabricated with the aid of numerical lathe and milling machines. Intermediate measurements made on prototypes copper cells and final structure have been performed in order to control the dimensions of the cells and the changes introduced by the soldering procedure.
A dedicated test set was constructed to check the frequency of each cell before soldering. Each cell (Fig. 4.40) has been short circuited with two plates (Fig. 4.41) and the frequencies of the first two monopoles and dipoles have been measured and compared with those obtain by HFSS simulations. The frequency deviations due to the presence of measuring antennas, to the air[77] and to the cell temperature with respect to the nominal one (30°C) have been taken into account with a progressive decoupling of the antennas and performing the measurements at different temperatures. The comparison of the calculated and measured frequencies in a sample of 8 cells is reported in Table 4.6.

[77] The e_{rair}=1,0008 and introduces a shift in the resonant frequency of the cells of the order of some hundreds of KHz.

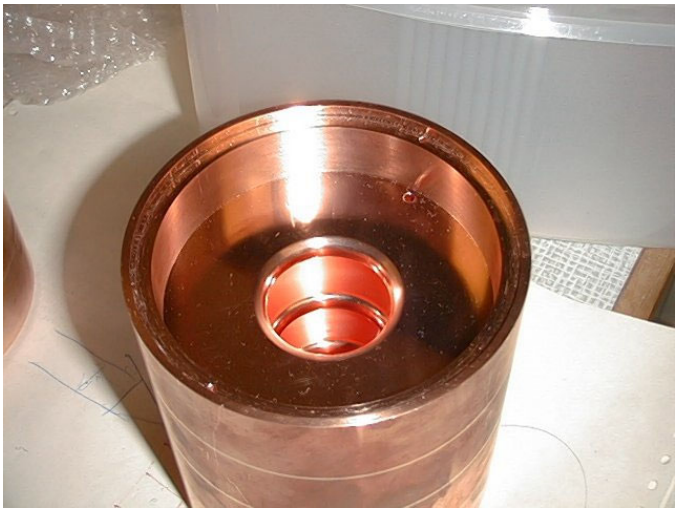

Fig. 4.40: RF deflectors cells before soldering.

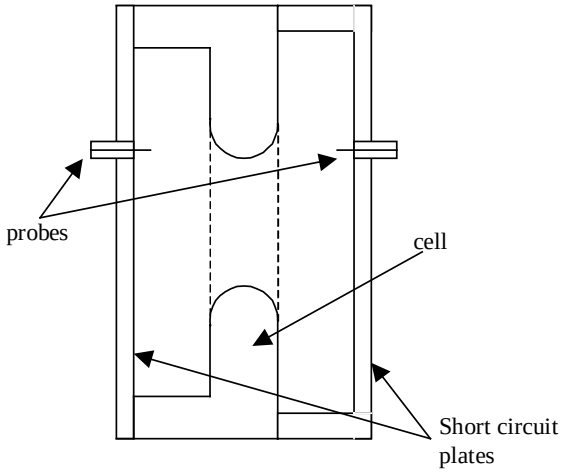

Fig. 4.41 sketch of the short-circuited cell.

Table 4.6: Comparison of calculated and measured frequencies of cells ready for soldering.

	Monopole 1	Monopole 2	Dipole 1	Dipole 2
HFSS simul.	2105.7 [MHz]	2176.8 [MHz]	3010.9[MHz]	3226.0 [MHz]
Cell number	Mesured frequency deviation [KHz]			
1	-295	-674	96	-846
2	-395	-599	-179	-846
3	-325	-549	-79	-771
4	-435	-675	-189	-926
5	-375	-535	-264	-840
6	-335	-594	-44	-826
7	-335	-554	-104	-825
8	-295	-534	-104	-826

In order to measure the dispersion curve of the structure, 8 cells +2 half-cells have been assembled as shown in Fig. 4.42. The $|S_{12}|$ plot is shown in Fig 4.43 for both polarities and the sampled dispersion curve is plotted in Fig. 4.44.
To evaluate the effect of soldering procedure, a series of 4 pilot copper cells have been measured before and after soldering showing that the change in the resonant frequency due to the soldering procedure is completely negligible.
The phase advance per cell and the reflection coefficient at the input port of the deflector (Fig. 4.47) have been, finally, measured with the technique illustrated in the par. 2.4.5. The first results are plotted in Figs. 4.45 and clearly shown that from cell to cell there is a phase advance in the range of ±5° that completely satisfy the tolerance requirements. The SWR measured at the input port and plotted in Fig. 4.46, where it is clearly shown that, at the working frequency, the reflected power is of the order of few percent.

Fig. 4.42: cells assembly in order to measure the dispersion curve of the structure

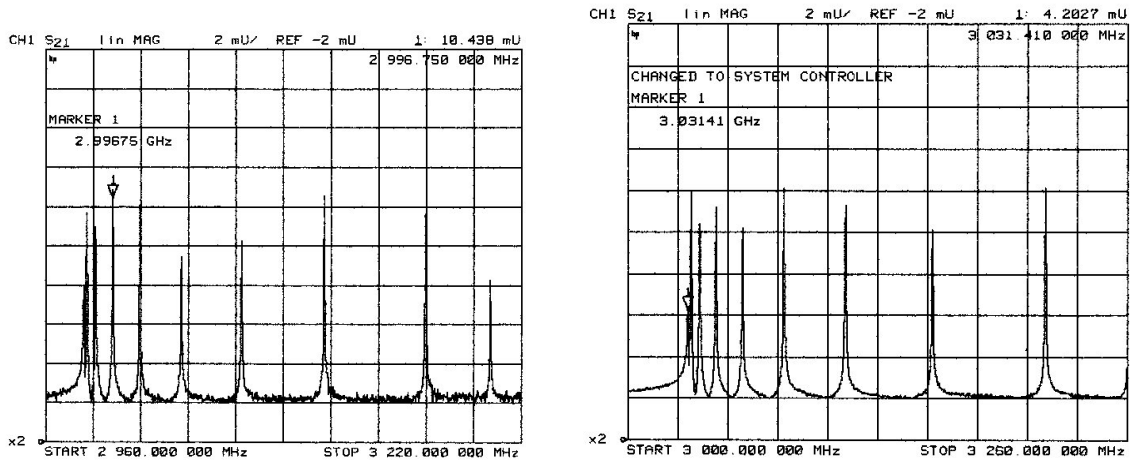

Fig. 4.43: $|S_{21}|$ of a 8 deflector cells+2 half cells assembly
(a-horizontal polarity; b-vertical polarity).

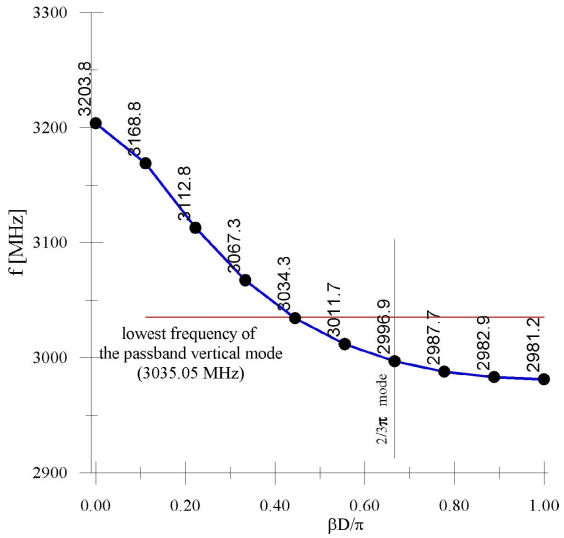

Fig. 4.44: sampled dispersion curve of 8 cells+2 half-cells of the RF deflectors

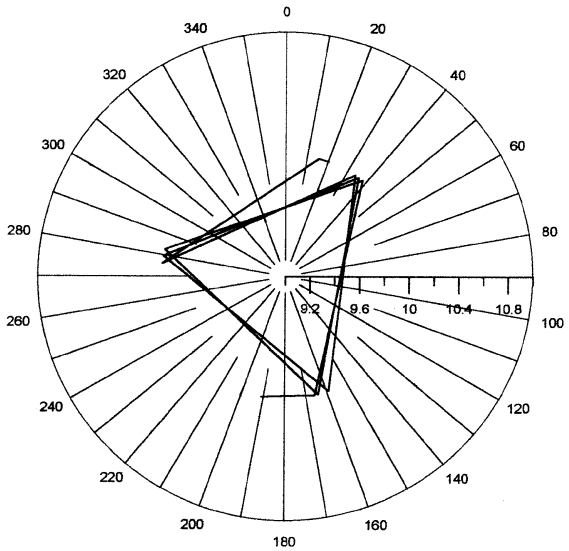

Fig. 4.45: phase advance per cell measurement results.

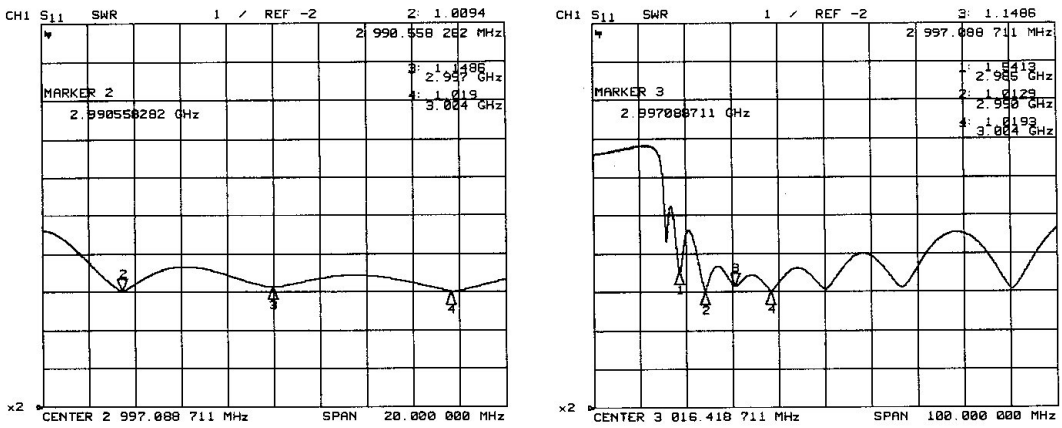

Fig. 4.46: SWR at the input port of the deflector.

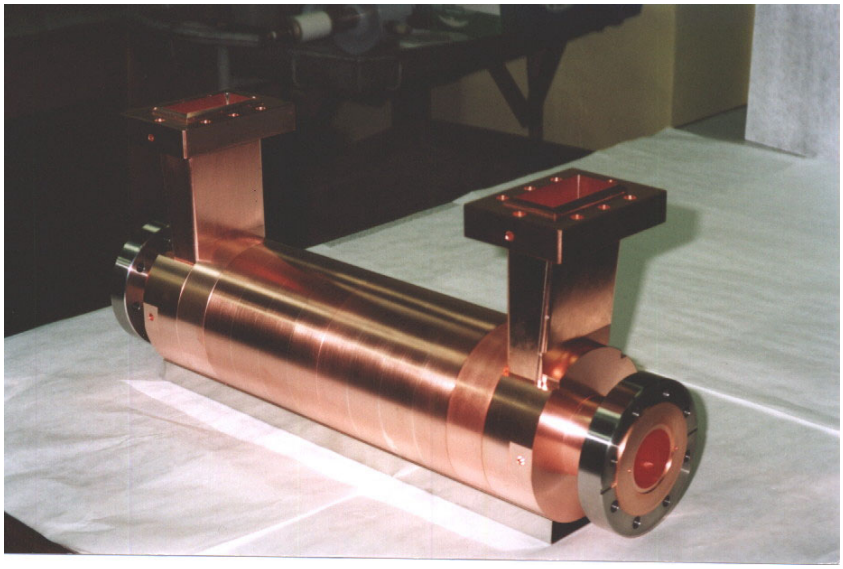

Fig. 4.47: Final RF Deflector.

Appendices to Chapter 4

Appendix A4.1: Calculation of the coefficient c_n^+ of eq. (4.3)

Considering an electric density current J(ω) at a certain waveguide section z_1-z_2 (Fig. 1.A4.1), it is possible to calculate the coefficients c_n^+ of the eq. (4.3) by the simple formula [65]:

$$c_n^+(\omega) = \mp \frac{\int_V (\underline{e}_{tn} - e_{zn}\underline{z}_0)\cdot \underline{J}(\omega) e^{j\beta_n(\omega)z} dV}{2\int_{S_2} \underline{e}_{tn} \times \underline{h}_{tn} \cdot \underline{z}_0 dS_2}$$

(1.A4.1)

where the sign "-" refers to the case of forward waves while the sign "+" to the backward ones[78].
The density current, in the time domain, of a particle of charge q that moves through the waveguide (Fig. 4.6) at the speed of light, is given by:

$$\underline{J}(t) = q\underline{s}_0(s)\delta\left(t - \frac{s}{c}\right)\delta(x')\delta(y')$$

(2.A4.1)

where s is the distance along the particle trajectory, s_0 is the unit vector tangent to the trajectory and (x',y') is the reference system on the plane normal to s_0. In the frequency domain the equation (2.A4.1) becomes:

$$\underline{J}(\omega) = q\underline{s}_0(s)e^{-j\omega\frac{s}{c}}\delta(x')\delta(y')$$

(3.A4.1)

Considering the beam loading 90° out-of-phase in RF deflectors, one has to consider, in the scalar product $\underline{E}\cdot\underline{J}$ of eq. (1.A4.1), only the longitudinal component of the electric field and density current. For a particle moving in the structure $\underline{J} \cong J\cdot\underline{z}_0$ and the coefficient $c_n^+(\omega,z_1,z_2)$ for a backward wave[79] can be written in the form:

$$c_n^+(\omega, z_1, z_2) = -\frac{q}{4\Pi'_n(\omega)}\int_{z_1}^{z_2} e_{zn}\left(\omega, \underline{r}(z')\Big|_{\substack{particle\\trajectory}}\right)e^{-j\omega\frac{z'}{c}} e^{j\beta_n(\omega)z'} dz'$$

(4.A4.1)

[78] For forward waves the group velocity ($v_g=d\omega/d\beta$) and the phase velocity ($v_{ph}=\omega/\beta$) have the same sign while for the backward ones have opposite signs.
[79] The RF deflectors for CTF3 are backward structures.

where $r(z')|_{\text{particle trajectory}}$ is the transverse position of the particle along the structure (function of the longitudinal position z') and Π'_n is given by:

$$\Pi'_n(\omega) = \frac{1}{2}\int_{S_1} \underline{e}_{tn} \times \underline{h}_{tn} \cdot \underline{z}_0 dS_1 \tag{5.A4.1}$$

It is easy to verify, from the analytical formulae [73], that[80]:

$$\Pi_n(\omega) = \frac{1}{2}\int_{S_1} \underline{e}_{tn} \times \underline{h}^*_{tn} \cdot \underline{z}_0 dS_1 = -\Pi'_n(\omega) \tag{6.A4.1}$$

where Π_n is the power flow along the structure[81].
If the deflector length is L and the particle enters at z=0 one obtains the following expression:

$$c_n^+(\omega, z) = \frac{q}{4\Pi_n(\omega)}\int_z^L e_{zn}\left(\omega, \underline{r}(z')\Big|_{\substack{particle\\trajectory}}\right) e^{-j\omega\frac{z'}{c}} e^{j\beta_n(\omega)z'} dz' \tag{7.A4.1}$$

and, therefore the eq. (4.4).

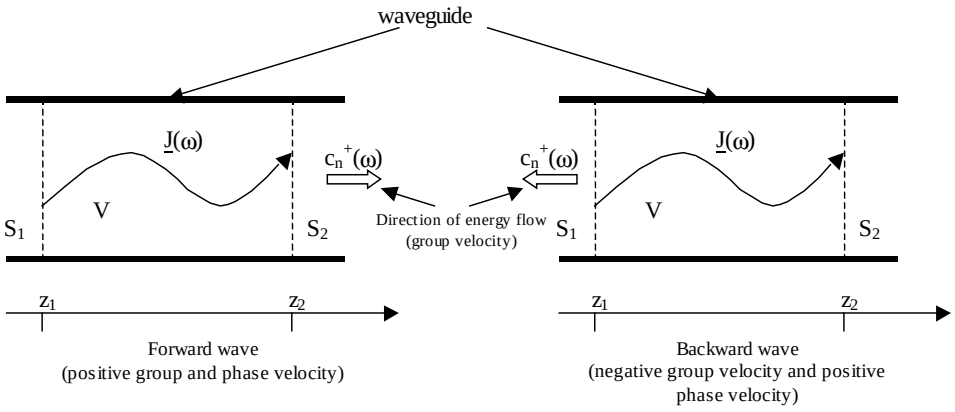

Fig. 1.A4.1: sketch of a waveguide excited by an electric current

[80] This is valid, in general, for all propagating fields in which the longitudinal dependence (z) and the transverse one (r,ϑ) are separated in the form $\underline{e}(r,\vartheta,z)=\underline{e}_t(r,\vartheta)\cdot\underline{e}_z(z)$ [65].
[81] In the case of backward wave Π_n is negative.

Appendix A2: Approximated expression for the field in the case of dispersion curve linearization in a limited range of frequency

Considering the equation (4.4) one can develop to the first order in ω the exponential term obtaining:

$$-\omega\frac{z'}{c}=-\omega^*\frac{z'}{c}+\left(\omega^*-\omega\right)\frac{z'}{c}$$
$$\beta(\omega)z'\cong\beta(\omega^*)z'+\left.\frac{d\beta}{d\omega}\right|_{\omega=\omega^*}(\omega-\omega^*)z'$$

(1.A4.2)

Substituting in the equation (4.4) one obtains ([82]):

$$c_1^+(\omega,z)=\frac{q}{4\Pi_1(\omega^*)}\begin{cases}\int_z^L e_{z1}(\omega^*)\big|_{\substack{particle\\trajectory}}e^{j\left(\left.\frac{d\beta}{d\omega}\right|_{\omega=\omega^*}-\frac{1}{c}\right)(\omega-\omega^*)z'}dz'\cong & \omega\in\left[\omega^*-\frac{\Delta\omega}{2},\omega^*+\frac{\Delta\omega}{2}\right]\\ \cong\int_z^L e_{z1}(\omega^*)\big|_{\substack{particle\\trajectory}}e^{j\left(\left.\frac{d\beta}{d\omega}\right|_{\omega=\omega^*}\right)(\omega-\omega^*)z'}dz' & \\ 0 & \text{elsewhere}\end{cases}$$

(2.A4.2)

The second approximation in the interval [ω^*-Δω/2, ω^*+Δω/2] comes out from the fact that the group velocity v_g for this kind of structures is few percent of the velocity of light.

The field is simply given by the expression (4.6) where one has to develop to the first order the exponential term -jβ(ω)z obtaining:

$$\underline{E}_n^+(t,z)\cong\frac{q}{4\pi\Pi_1(\omega^*)}$$
$$\mathrm{Re}\left[\underline{e}_1^+(\omega^*)\int_z^L e_{z1}\left(\omega^*,\underline{r}(z')\big|_{\substack{particle\\trajectory}}\right)\int_0^\infty e^{j\left.\frac{d\beta}{d\omega}\right|_{\omega=\omega^*}(\omega-\omega^*)z'}e^{-j\beta(\omega^*)z-j\left.\frac{d\beta}{d\omega}\right|_{\omega=\omega^*}(\omega-\omega^*)z}e^{j\omega t}d\omega\,dz'\right]=$$
$$=\frac{q}{4\pi\Pi_1(\omega^*)}$$
$$\mathrm{Re}\left[\underline{e}_1^+(\omega^*)\int_z^L e_{z1}\left(\omega^*,\underline{r}(z')\big|_{\substack{particle\\trajectory}}\right)e^{-j\left.\frac{d\beta}{d\omega}\right|_{\omega=\omega^*}\omega^*(z'-z)-j\beta(\omega^*)z}\int_0^\infty e^{j\omega\left(t-\left.\frac{d\beta}{d\omega}\right|_{\omega=\omega^*}(z-z')\right)}d\omega\,dz'\right]$$

(3.A4.2)

[82] $\omega^*/c=\beta(\omega^*)$.

Considering the integral in dω limited between ω^*-Δω/2 and ω^*+Δω/2 one obtain:

$$\int_{\omega^*-\frac{\Delta\omega}{2}}^{\omega^*+\frac{\Delta\omega}{2}} e^{j\omega\left(t-\left.\frac{d\beta}{d\omega}\right|_{\omega=\omega^*}(z-z')\right)} d\omega = e^{j\omega^*\left(t-\left.\frac{d\beta}{d\omega}\right|_{\omega=\omega^*}(z-z')\right)} \Delta\omega \mathrm{sinc}\left[\left(t-\frac{z-z'}{v_g}\right)\frac{\Delta\omega}{2}\right]$$

(4.A4.2)

where sinc(x)=sin(x)/x.

Appendix A4.3: Intuitive approach for the wake field calculation in a tw RF deflector

Considering the resonant field configuration of eq. (4.1) with a local excitation proportional to the leading charge displacement, the energy per unit length stored in the section corresponding to the abscissa z after the charge passage is given by:

$$U = \frac{1}{2}V(z)q = \frac{1}{2}\frac{E}{2}kr(z)q$$

(1.A4.3)

where -½V(z) is the voltage seen by the charge q ([83]), r(z) is the q displacement with respect to the axis and E/2 is the field amplitude.
Remembering the definition (4.12) of the R/Q and that:

$$U = \frac{\Pi(\omega^*)}{v_g}$$

(2.A4.3)

one simply obtains that the amplitude of the excited field at the abscissa z is given by:

$$\frac{E}{2} = \frac{1}{2}k\omega^*\frac{R}{Q}r(z)q$$

(3.A4.3)

Since $v_g << v_{ph}$ it is reasonable to suppose that the E field generated by the particle passage has the rigid amplitude profile given by (3.A4.3), a phase velocity equal to c and a negative group velocity v_g obtaining the equation (4.13).

[83] The factor ½ comes out from the beam loading theorem.

Appendix A4.4: Phase velocity and kick deviation as a function of a cell frequency error

Since $v_{ph}=\omega/\beta$ it follows that:

$$\frac{\Delta v_{ph}}{c}=\frac{1}{c}\Delta\left(\frac{\omega}{\beta}\right)=\frac{1}{\beta c}\Delta\omega-\frac{\omega}{c\beta^2}\underbrace{\frac{\Delta\beta}{\Delta\omega}}_{1/v_g}\Delta\omega \overset{\substack{\beta c=\omega \\ |v_g|<<c}}{\cong} \frac{c}{|v_g|}\frac{d\omega}{\omega} \tag{1.A4.4}$$

The integrated transverse force along the structure for a particle with a velocity equal to c is given by:

$$\int_0^L F_\perp dz=\int_0^L F_{\perp 0}\cos(\omega t-\beta z+\Delta\varphi)dz \underset{t=\frac{z}{c}}{=} F_{\perp 0}\int_0^L \cos\left[\left(\frac{\omega}{c}-\beta\right)z+\Delta\varphi\right]dz=$$

$$=F_{\perp 0}\frac{1}{\frac{\omega}{c}-\beta}\sin\left[\left(\frac{\omega}{c}-\beta\right)z+\Delta\varphi\right]\Bigg|_0^L=F_{\perp 0}L\frac{\sin\left[\omega\left(\frac{1}{c}-\frac{1}{v_{ph}}\right)L+\Delta\varphi\right]-\sin(\Delta\varphi)}{\omega\left(\frac{1}{c}-\frac{1}{v_{ph}}\right)L} \tag{2.A4.4}$$

the initial phase $\Delta\varphi$ of the travelling wave can be chosen in order to maximize the integrated transverse force:

$$\frac{d\left\{F_{\perp 0}L\frac{\sin\left[\omega\left(\frac{1}{c}-\frac{1}{v_{ph}}\right)L+\Delta\varphi\right]-\sin(\Delta\varphi)}{\omega\left(\frac{1}{c}-\frac{1}{v_{ph}}\right)L}\right\}}{d\Delta\varphi}=0\Rightarrow\Delta\varphi_{opt}=-\omega\left(\frac{1}{c}-\frac{1}{v_{ph}}\right)\frac{L}{2} \tag{3.A4.4}$$

and the maximum integrated force becomes:

$$\int_0^L F_\perp dz\Big|_{\max}=F_{\perp 0}L\,\mathrm{sinc}\left[\underbrace{\omega\left(\frac{1}{c}-\frac{1}{v_{ph}}\right)}_{\cong\frac{\Delta v_{ph}}{c^2}}\frac{L}{2}\right]\cong F_{\perp 0}L\,\mathrm{sinc}\left[\frac{L}{2}\frac{\Delta\omega}{|v_g|}\right] \tag{4.A4.4}$$

Since $\int_0^L F_{\perp nom}dz=F_{\perp 0}L$ it follows directly the eq. (4.23).

Chapter 5

Resonant bunch length-position monitor for ultra short bunches

The measure of the bunch length and transverse position of the beam inside the vacuum chamber is a very important issue in both circular and linear accelerators.
It allows tuning the machine parameters in order to obtain the better performances in terms, for example, of luminosity or beam power extraction as in the CTF3 case.
A large number of bunch length monitors exists both in the time domain and in the frequency domain. In particular, the devices that use the microwave spectroscopy [113-115] are based on the analysis of the beam characteristics in the frequency domain. By this analysis it is possible to obtain the bunch parameters in the time domain such as a bunch length or a position inside the vacuum chamber.
Different techniques have been proposed to couple the field radiated by the bunch in a transmission line leading the signal to the detection system.
In this chapter the design of a bunch length-position monitor is discussed and the microwave measurement results made on a prototype are illustrated.
In the first paragraph the theoretical analysis of the device is presented. In the second paragraph the simulations results obtained by HFSS and MAFIA are reported and in the last paragraph the theoretical results are compared with the measurements made on a prototype.

5.1 Analytical approach

Bunch length monitor

The monitor consists of a small coaxial cavity coupled to the beam pipe trough four slots (Fig. 5.1 and Table 5.1). If the length of the cavity is properly chosen, the beam power spectrum lines excite the resonant TEM modes in the cavity. Probing the field by a small antenna it is possible to measure the amplitude of two beam power spectrum lines [116-118].
More precisely, as illustrated in the par. 1.3.3, the Fourier components of an infinite train of gaussian non-oscillating bunch are given by the equation (1.83).

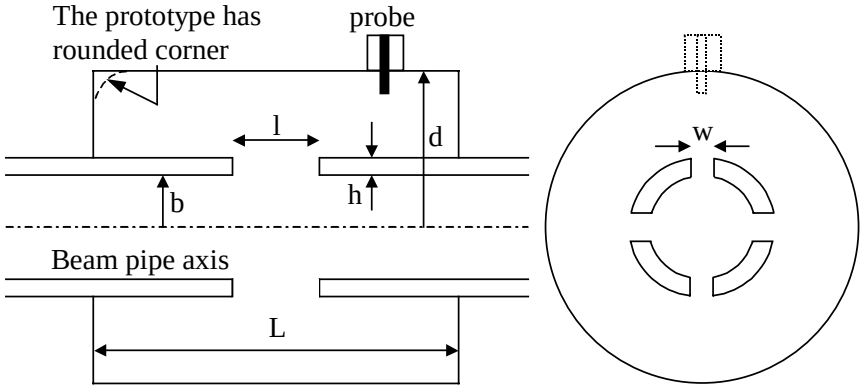

Fig. 5.1: sketch of the microwave monitor.

Table 5.1: monitor dimensions

d	30 mm
b	10 mm
L	52 mm
w	2 mm
l	5 mm
h	1 mm

Knowing the ratio between the n^{th} harmonics component of the beam and the average powers extracted by a probe coupled with the field in the cavity at two different harmonics:

$$\underline{P}_{E1,2}(\omega_{1,2}) = P_{E1,2}(\omega_{1,2}) / \left|\tilde{I}_{1,2}\right|^2 \tag{5.1}$$

the bunch length can be determined with the formula:

$$\sigma_z = c\sqrt{\frac{1}{\omega_1^2 - \omega_2^2} \ln\left(\frac{\underline{P}_{E1}}{\underline{P}_{E2}} \frac{P_{E2}}{P_{E1}}\right)} \tag{5.2}$$

where $P_{E1,2}$ are the average powers extracted by the probe at the frequencies $\omega_{1,2}$.
The ratios (5.1) can be obtained in three different ways:

a) by an analytical treatment of the e.m. problem;
b) by the results of an e.m. simulation code;
c) by a calibration of the monitor with bench RF measurements.

The first approach allows determining the main key parameters that gives the extracted power as a function of the monitor dimensions.
The second approach allows validating the theoretical results choosing more in detail the probe dimensions in order to obtain a certain coupling factor between the field in the cavity and the antenna.
The third way can be considered, finally, as the final step that allows determining the calibration coefficients for the constructed devices.
Analytically, the amplitude of the resonant e.m. field in the cavity as a function of the beam current can be obtained by the modified Bethe's theory [119,120].
This theory has been already applied for the study of similar problems [121] and it is well described in literature.
The basic idea is to find the equivalent electric and magnetic dipole momenta of the 4 holes as a function of the beam current and hole dimensions. This dipoles momenta with intensities proportional to the electric and magnetic field of the primary field radiated by the beam with a correction factor that takes into account the excited field in the cavity itself, allows finding the amplitude of the resonant field in the cavity and, therefore, the ratios (5.1).
Following the calculations reported in [116] the ratio between the average powers dissipated in the cavity $\underline{P}_{1,2}$ ([84]) and the beam current spectrum lines are given by:

$$\underline{P}_1 = \frac{P_1}{\left|\tilde{I}_1\right|^2} = \frac{2\alpha_E^2 Q_1 \pi \ln(d/b) / \left\{\varepsilon\omega_1 L\left[4\alpha_E - b^2\pi L \ln(d/b)\right]^2\right\}}{1+\left\{\frac{\pi^3 b^2 Q_1 \ln(d/b)}{\mu\varepsilon\omega_1^2 L\left[4\alpha_E - b^2\pi L \ln(d/b)\right]} + 1 + Q_1\right\}^2}$$

$$\underline{P}_2 = \frac{P_2}{\left|\tilde{I}_2\right|^2} = \frac{2\alpha_M Q_2 / \left(\pi^2 L^2 \varepsilon\omega_2 b^4\right)}{\left[\frac{4Q_2\pi^2}{L^2\mu\varepsilon\omega_2^2} + \frac{(1+Q_2(1+4\alpha_M))}{\pi L b^2 \ln(d/b)}\right]^2 + 1} \tag{5.3}$$

where $\omega_{1,2}$ and $Q_{1,2}$ are the resonant angular frequencies and the quality factors of the two TEM modes, α_E, α_M are the electric and magnetic polarizabilities (see Appendix A5.1) and the other quantities are defined in Fig. 5.1.
The Q-factors of the resonant TEM modes and α_E, α_M can be determined knowing the monitor dimensions and the material conductivity.
As an example, with the dimensions of Table 5.1, the $\underline{P}_{1,2}$ values and the ratio $\underline{P}_1/\underline{P}_2$ are reported in Table 5.3 (first column).
The values of P_1 and P_2 as a function of the bunch length are reported in Fig. 5.2 assuming a 100 mA average beam current and a full coupling between the Fourier components of the beam and the resonant modes.

[84] The power dissipated in the cavity is proportional through the β coupling coefficient of the antenna to the power dissipated in the external load P_E (see eq. (2.18)).

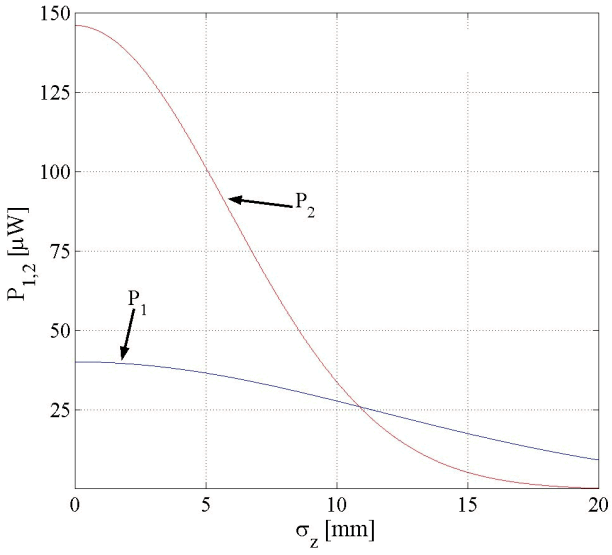

Fig. 5.2: values of P_1 and P_2 as a function of the bunch length assuming a 100 mA average beam current and a full coupling between the Fourier components of the beam and the resonant modes.

Beam position monitor

The monitor can be also used to determine the transverse position of the beam. In this case the amplitudes of the two first dipolar modes TE_{111} excited by the off-axis passage allow calculating the transverse displacement of the bunches.
The TE modes have to be properly tuned in order to resonate at one of the frequencies of the beam power spectrum lines.
In this case, the average power extracted by two probes coupled with the two dipolar modes ([85]) can be expressed as a function of the beam current and transverse displacement and can be written in the general form:

$$\begin{cases} P_{TE0}^{(E)} = \underline{P}_{TE0}^{(E)}(\omega_{TE}, r)\left|\tilde{I}(\omega_{TE})\right|^2 \cos(\phi)^2 \\ P_{TE\pi}^{(E)} = \underline{P}_{TE\pi}^{(E)}(\omega_{TE}, r)\left|\tilde{I}(\omega_{TE})\right|^2 \sin(\phi)^2 \end{cases} \tag{5.4}$$

where the $\tilde{I}(\omega_{TE})$ is the beam power spectrum line at the resonant frequency of the TE_{111} modes, r is the transverse displacement of the beam and ϕ is the angle between one of the two dipolar mode and the beam displacement.

[85] The two polarities ore 90° tilted.

Knowing by theory, simulations or measurements the calibration coefficient $\underline{P}^{(E)}_{TE0,\pi}$ and the beam power spectrum line, the eq. (5.4) allows to determine the values of r and |cos(ϕ)| by a measure of the powers $P^{(E)}_{TE0,\pi}$.

The analytical treatment based on the Bethe's theory follows steps similar to those done in the TEM modes calculation [122].

The normalized power dissipated in the cavity ($\underline{P}_{TE}$) can be expressed by the formula:

$$\underline{P}_{TE} = \omega_{TE} \frac{G}{Q_{TE}} r^2 \tag{5.5}$$

where Q_{TE} is the quality factor of the TE_{111} mode and the function G depends only by the cavity geometry (as reported in [122]).

As the general theory of dipolar modes states (par.1.1.3), the extracted power is proportional to the r^2. Considering the dimensions of Table 5.1, the value of $\underline{P}'_{TE}=\underline{P}_{TE}/r^2$ is 169 [W/m^2A^2]. The $\underline{P}_{TE}$ value is plotted in Fig. 5.3 as a function of the transverse displacement r.

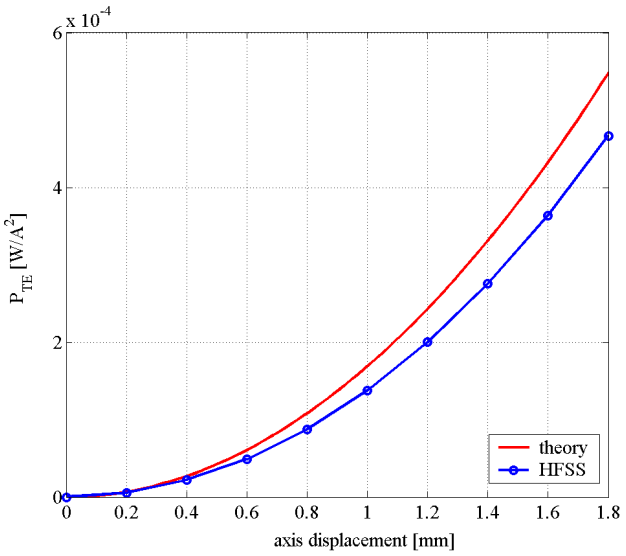

Fig. 5.3: values of $\underline{P}_{TE}$ as a function of the transverse displacement r assuming ϕ=0: theory and simulations (HFSS).

5.2 Simulations results

Bunch length monitor

To compare the analytical results with the simulations it has been considered an impedance model for the beam-cavity interaction. Knowing the R/Q of the resonant modes $TEM_{1,2}$, the ratios (5.1) are simply given by:

$$\underline{P}_{1,2} = \frac{P_{1,2}}{\left|\tilde{I}_{1,2}\right|^2} = \frac{1}{2}\frac{R}{Q}\bigg|_{1,2} Q_{1,2} \tag{5.6}$$

The R/Qs, the Q factors and the resonant frequencies of the resonant modes can be determined simulating the structure with the eigenmode solver of HFSS and MAFIA and are reported in Table 5.2 considering the dimensions of Table 5.1.

Table 5.2: R/Qs, resonant frequencies and the Q factors obtained by HFSS and MAFIA

		HFSS	**MAFIA**
TEM1	**R/Q**	1.17e-6 Ω	8.67e-7 Ω
	Q	6300	6300
	f	2.883 [GHz]	2.883 [GHz]
TEM2	**R/Q**	6.94e-6 Ω	4.71-6 Ω
	Q	8790	8950
	f	5.762 [GHz]	5.762 [GHz]

The HFSS simulated structure with the E field lines of the TEM_1 mode is shown in Fig. 5.4a. Because of the symmetries just one eighth of the structure has been simulated with the proper boundary conditions.
The longitudinal electric field obtained by HFSS and calculated at the center of the beam pipe is reported in Fig. 5.4b.
Considering the dimensions of the prototype, the obtained average normalized dissipated power $\underline{P}_{1,2}$ and the normalized ratio $\underline{P}_1/\underline{P}_2$ are reported in Table 5.3 (second column) and compared with the analytical and measurement results.

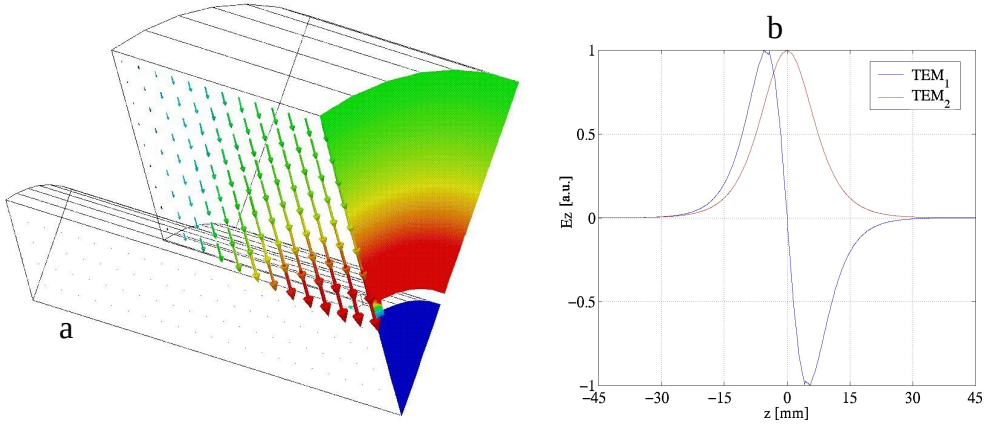

Fig. 5.4: (a) HFSS simulated structure with the E filed lines; (b) longitudinal electric fields obtained by HFSS and calculated at the center of the beam pipe.

Beam position monitor

As done for the TEM modes an impedance model for the beam cavity interaction can be adopted also in this case.
According to the theory, for small displacements from the beam pipe axis the power dissipated in the cavity can be expressed as:

$$P_{TE} = \underline{P}_{TE}\left|\tilde{I}\right|^2 = \underbrace{\frac{1}{2}\frac{R'_{TE}}{Q_{TE}}Q_{TE}}_{\underline{P}'_{TE}} r^2 \left|\tilde{I}\right|^2 \tag{5.7}$$

the R'_{TE}/Q_{TE} can be determined simulating the structure by HFSS or MAFIA.
In this case it is necessary to simulate one quarter of the structure because of the cos(ϕ) dependence of the field with the proper boundary conditions.
The HFSS simulated structure with the E field lines is shown in Fig. 5.5a while the longitudinal electric field for different axis displacements is reported in Fig. 5.5b.
The plot of $\underline{P}_{TE}$ as a function of r is reported in Fig. 5.3 and compared with the analytical result. The resonant frequency given by HFSS is 3.744 GHz while the Q factor equal to ~9000 .

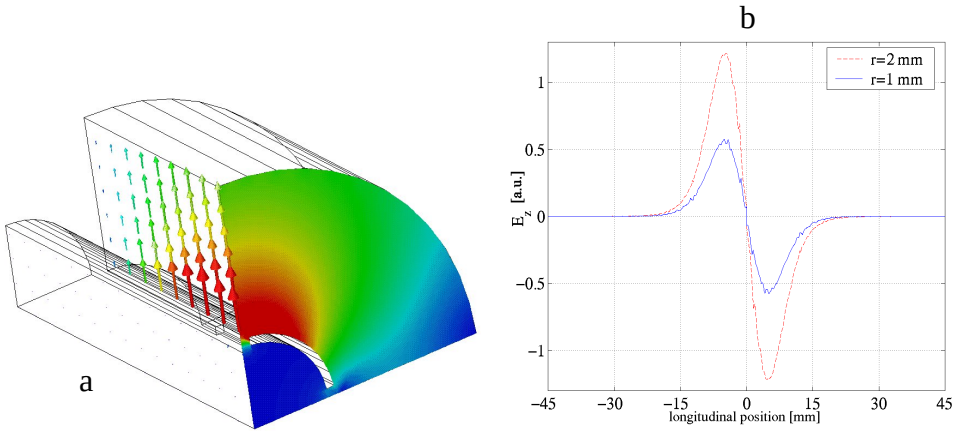

Fig. 5.5: (a) HFSS simulated structure with the E field lines; (b) longitudinal electric fields obtained by HFSS and calculated for different axis displacements

5.3 Prototype measurements

Considering a small probe coupled to the cavity modes, the normalized total average dissipated powers in the load+cavity are related to the average dissipated powers in the load connected to the probe by the simple formula (see par. 2.1.2):

$$\underline{P}_{1,2,TE} = \frac{\left(1+\beta_{1,2,TE}\right)}{\beta_{1,2,TE}} \frac{P^{(E)}_{1,2,TE}}{\left|\tilde{I}_{1,2,TE}\right|^2} \tag{5.8}$$

where $\beta_{1,2,TE}$ is the coupling coefficients between the probe and the cavity modes $TEM_{1,2}$ and TE_{111} respectively, $P^{(E)}_{1,2,TE}$ is the dissipated power in the external load in the three cases and $\left|\tilde{I}_{1,2,TE}\right|$ is the absolute value of the beam Fourier component corresponding to the three resonant mode frequencies.
Following this general consideration it is possible to correctly compare the measurement with the theoretical results.

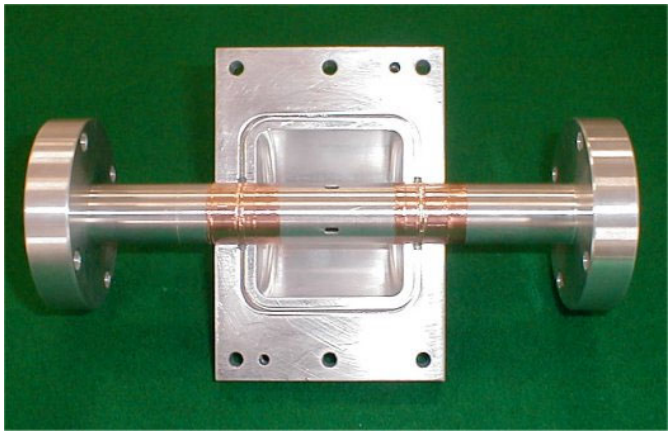

Fig. 5.6: bunch length-position monitor aluminum prototype.

Bunch length monitor

Wire measurements have been made on the aluminum prototype shown on Fig. 5.6.
The prototype dimensions are those of Table 5.1 referred to Fig. 5.1. A small antenna coupled to the E field has been inserted to probe the signal on the cavity.
As illustrated in par. 2.43, in the wire measurement the beam current is substituted with the current flowing on a wire (in this case of radius r=1.5 mm).
The measurements setup is shown Fig. 5.7a and schematically represented in Fig 5.7b (the equivalent circuit is equal to those discussed in the par. 2.4.3).
In order to avoids reflections at the input ports 1 and 2 two tapered sections of length L_{tap}=20 cm have been inserted in order to match the 50 Ω impedance of the Network Analyzer with the impedance of the coaxial waveguide made by the inner wire and the beam pipe ($Z_c \cong 114\ \Omega$). The measured transmission coefficients $|S_{21}|$ and $|S_{31}|$ are shown in Fig. 5.8.
Since the $|S_{21}|$ is almost equal to 1 the networks A and B (tapered section) realized a perfect matching and is, therefore, possible to use the formula (2.38) for the transfer impedance calculation. The total average dissipated powers in the external load are simply given by:

$$\underline{P}_{E1,2} = \frac{1}{2} Z_c \frac{\left|S_{31mes}\right|^2_{1,2}}{S_{21mes1,2}} \tag{5.9}$$

The results obtained by measurements must be considered as calibration coefficients that allow calculating the normalized average dissipated power in the load, and, therefore, the σ_z when the bunch length monitor is inserted in the accelerator (eq. (5.2)).

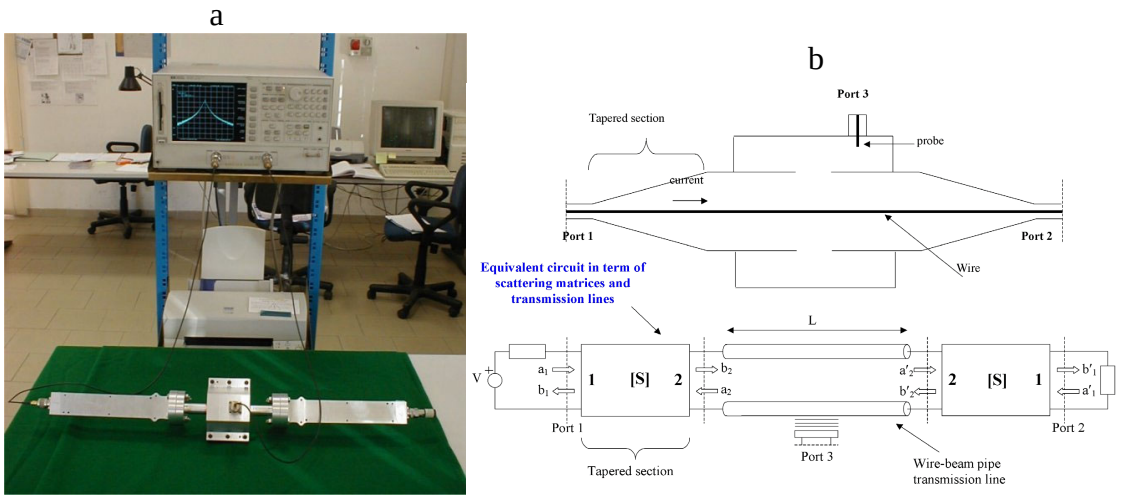

Fig. 5.7: (a) measurements setup; (b) schematic representation of the measurement and equivalent circuit.

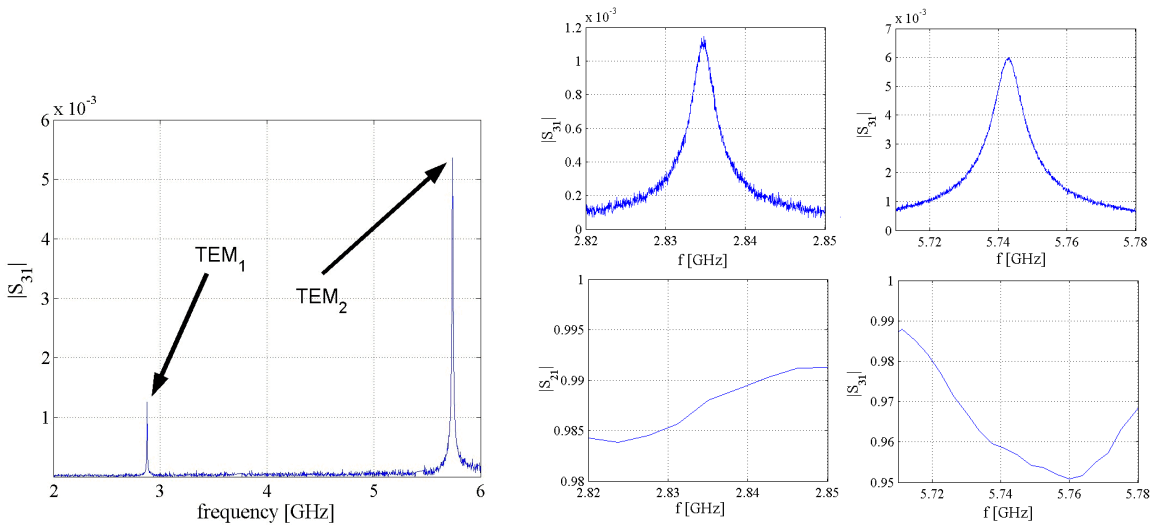

Fig. 5.8: (a) measured transmission coefficients S_{31} in the range 2-6 GHz; (b) measured transmission coefficients S_{31} and S_{21} near the TEM resonances.

The total average dissipated powers in the cavity+external load are given by:

$$\underline{P}_{1,2} = \frac{1}{2} Z_c \frac{\left|S_{31mes}\right|_{1,2}^2}{S_{21mes1,2}} \frac{\left(1+\beta_{1,2}\right)}{\beta_{1,2}} \tag{5.10}$$

In order to compare the measurement results with the theoretical calculations the powers given by eq. (5.10) have to been properly normalized to the theoretical Q factors. In fact, since in the prototype there are additional losses due to RF contact in the final assembly, the Q factors (also unloaded) are very low compare to the theoretical one ($Q_{M1}\approx1400$, $Q_{M2}\approx1600$).

Following the formula (5.6) one has to do the following normalization:

$$\underline{P}'_{1,2} = \underline{P}_{1,2} \frac{Q_{1,2}}{Q_{M1,2}} \tag{5.11}$$

The $\underline{P}'_{1,2}$ powers and the ratios $\underline{P}'_1/\underline{P}'_2$ obtained after this further normalization are plotted in Table 5.3 with the theoretical and numerical results.
As pointed out previously, in the wire measurements the beam current is substituted with the current flowing on a wire. This procedure induces some "intrinsic" errors in the evaluation of the calibration coefficients (5.1) as discussed in the par. 2.4. These errors can be, in principle, controlled (or evaluated) performing different measurements with a reduced wire radius. Unfortunately, doing this, the length of the tapers has to be increased in order to guarantee the correct matching. Measuring, anyway, the resonant frequency and Q factors by the $|S_{33}|$ at the antenna port with and without the wire inside the beam pipe, one notes that the perturbation induced by the wire, in this two quantities, is completely negligible.
The possible measurements uncertainty can be, instead, summarized as follows:

a) since the matching of the impedances with the tapered section is not perfect, the reflected wave at the port 2 introduces a perturbation in the cavity field and, consequently, an error in the evaluation of the transfer function between the beam current and the cavity field.
   Considering the measured scattering parameters and the calculations developed in the par. 2.4.3, it is possible to estimate the introduced uncertainty in the evaluation of the transfer function and, therefore, in the $\underline{P}_{1,2}$ calculations. This is of the order of ~±0.2% for $\underline{P}_1$ and ~±1% for $\underline{P}_2$.

b) The wire inside the beam pipe can be slightly of axis. Also this induced error can be evaluated performing different measurements in different prototype positions and as evaluated to give a negligible effect.

The differences between the theory, the simulations and the measurements can be explained considering that:

a) the theory has some "intrinsic" limitations in the evaluation of the coefficient α_E, α_M due to the finite depth of the slots [120] and due to the approximation $l<<\lambda$;
b) in the simulations the mesh near the axis of the beam pipe has to be heavily increased in order to correctly evaluate the R/Q because the E field on the beam pipe axis has an amplitude much smaller than in the cavity. This can give some numerical noises even if the solution converges in few adaptive passes.

c) the prototype has some non-negligible differences with respect to the structure considered in the theory and simulations: two screws that are used as tuners of the TEM modes, the antenna and the rounded corners (Fig. 5.1). Moreover, due to the non-perfect RF contacts there are more losses than can give a certain perturbation of the field in the cavity.

Table 5.3: Comparison between the normalized dissipated powers.

	THEORY	**HFSS**	**MAFIA**	**MEAS**
$\underline{\mathbf{P}}_1$	2.01e-3	0.74e-2	0.55e-2	1.58e-2
$\underline{\mathbf{P}}_2$	0.73e-2	0.61e-1	0.42e-1	0.89e-1
$\underline{\mathbf{P}}_1/\underline{\mathbf{P}}_2$	1.38e-1	0.60e-1	0.65e-1	0.88e-1

Beam position monitor

To excite the dipolar modes the wire inside the beam pipe has to be properly displaced from the axis of the beam pipe. To do this, a thin nylon wire has been connected to the central wire in order to displace it from the beam pipe axis in a controlled way [122] and exciting one of the two polarities (ϕ=0 in the general formula (5.4)). The measurements set-up, except this, is the same as that discussed in the previous section. The $|S_{31}|$ is reported in Fig. 5.9 as a function of frequency for few mm wire displacement. The values of the two peaks corresponding to the TEM modes do not depend on the axis displacement. On the contrary the value of the peak corresponding to the TE_{111} mode is very sensitive with respect the displacement itself and the $|S_{31}|$ grows linearly with the axis displacement (Fig. 5.10).
Also in this case the formula (5.9) allows to determine the calibration coefficients of eq. (5.4) and, since the considered axis displacements are much less than the beam pipe radius, the characteristic impedance Z_c can be considered constant and equal to ~114 Ω. The corresponding $P_{TE}^{(E)}$ grows, therefore, quadratically with the axis displacement.
To correctly compare the measurement and theoretical results and the theoretical one has to make the normalizations (5.10)-(5.11). In the range 0-1 mm the three results give a quadratic behavior of the average dissipated power of the form:

$$P_{TE} = \underline{P}'_{TE}\, r^2 \left|\tilde{I}\right|^2 \tag{5.12}$$

The obtained $\underline{P}_{TE}$ as a function of r is reported in Fig. 5.11 and compared with the theoretical and simulations results.
Similar comments to the previous section can be done for the measurement errors and theory approximations.

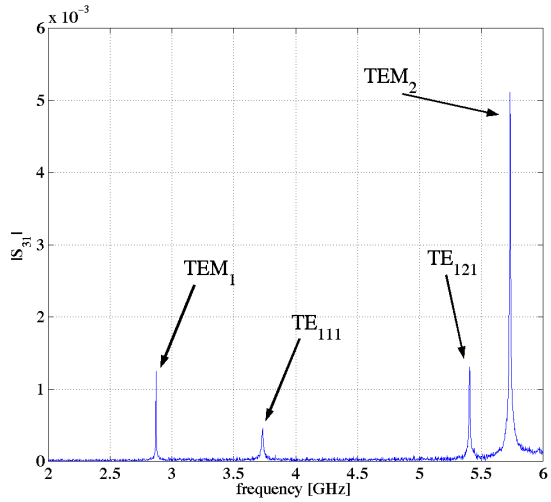

Fig. 5.9: $|S_{31}|$ as a function of frequency for few mm wire displacement.

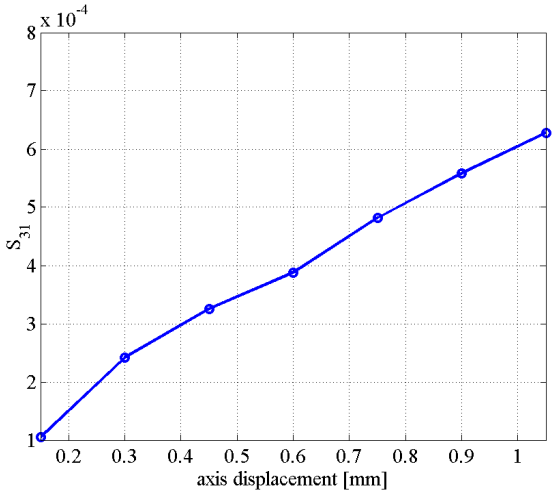

Fig. 5.10: $|S_{31}(\omega_T)|$ corresponding to the TE_{111} mode as a function of the axis displacement

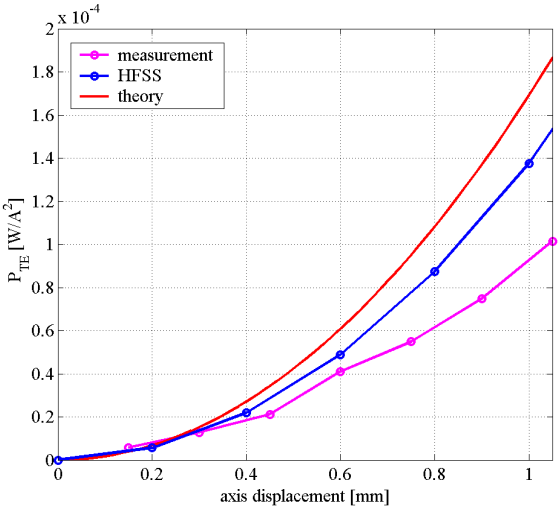

Fig. 5.11: values of $\underline{P}_{TE}$ as a function of the transverse displacement r assuming ϕ=0: theory, simulations (HFSS) and measurement.

Appendices to Chapter 5

Appendix A5.1: Expression of the Q factor and polarizabilities

The quality factor of the TEM modes is simply given by:

$$Q = \frac{2}{\delta} \frac{\ln\left(\frac{d}{b}\right)}{\frac{4}{L}\ln\left(\frac{d}{b}\right) + \frac{1}{b} + \frac{1}{d}} \tag{1.A5.1}$$

where the quantities are defined in Fig. 5.1 and the skin depth δ is given by:

$$\delta = \sqrt{\frac{2}{\omega\mu\sigma}} \tag{2.A5.1}$$

The electric and magnetic polarizabilities are given by:

$$\alpha_e = -\frac{\pi}{16} w^2 l \left[1 - 0.5663\frac{w}{l} + 0.1398\left(\frac{w}{l}\right)^2\right] e^{-\pi h\sqrt{\frac{1}{w^2}+\frac{1}{l^2}}}$$

$$\alpha_m = \frac{\pi}{16} w^2 l \left[1 + 0.3577\frac{w}{l} - 0.0356\left(\frac{w}{l}\right)^2\right] e^{-\pi h\frac{1}{w}} \tag{3.A5.1}$$

Conclusions

The aim of this work has been to illustrate the study of three different microwave devices for the control and the manipulation of particle beam in accelerators.
The study has included both the analysis of the beam dynamics effects induced by the devices and the e.m. design of the devices themselves. The first purpose has been achieved by using analytical theories or numerical tracking codes, while the design of the components has been done using e.m. simulation codes (MAFIA and HFSS) or e.m. theories (as in the case of the bunch length-position monitor).
Each device has been, then, completely characterized with microwave measurements and the experimental results have been compared with the theoretical ones.

Control of bunch length with a high harmonic cavity in DAΦNE

The study and the design of a high harmonic RF system for the accelerator DAΦNE has been mainly motivated by the demand of lifetime improvement and by the increasing of the natural Landau damping mechanism. The beam dynamics in the accelerator DAΦNE with a harmonic system has been analysed both using analytical theories and simulation codes. In particular the problem of the gap in the bunch filling pattern has been carefully analysed and the final bunch distribution and Touschek lifetime have been calculated.
The use of a passive harmonic cavity in the lengthening regime can improve the beam lifetime of the DAΦNE beam by a factor equal to ~80% if compared with the present operation condition. Nevertheless, the presence of a gap in the bunch filling pattern produces a spread in the Touschek lifetime and bunch distribution.
The analysis of the cavity parked option has shown the possibility to recover approximately the operating conditions before the harmonic cavity installation.
The design procedure has been described and the obtained results have been compared with measurements. The HOM damping realized with ferrite rings shows that all the higher order modes in the cavity are well damped.

RF Deflectors for CTF3

The beam dynamics in the Combiner Ring of CTF3 has been studied by modelling the wake fields in the RF deflectors. Different approximated formulae have been considered and discussed. A multi-particle multi-bunch tracking code has been written in order to study the multi-passage multi-bunch transverse beam dynamics.
The code has been developed considering both the case of bunches without finite bunch length than the case of a finite length.
The obtained results have shown that the emittance growth due to the wake fields in the deflectors is a small fraction of the bunch design emittance if the trains are

injected perfectly on axis. Some injection errors and ring phase advances can, however, increase the transverse emittance of a factor more than 10.
The design of the devices, realised by HFSS and MAFIA, has been discussed. The final RF deflectors measurements have been shown and compared with the theoretical results showing a very good agreement. The recombination with the contructed RF deflectors have been also successfully tested in the CTF3 Preliminary Phase [123] at low current.

Resonant bunch length-position monitor for ultra short bunches

The study of a bunch length-position monitor has been done using both the Bethe's theory and the simulations codes HFSS and MAFIA.
The monitor consists of a small coaxial cavity coupled to the beam pipe through four slots. Probing the resonant fields by a small antenna, it is possible to determine the bunch length and the position of bunches inside the beam pipe.
The wire measurements made on a prototype in the longitudinal and transverse cases have been discussed and compared with the theoretical results.
The obtained theoretical and experimental results confirm the potential application of this device as a bunch-length position monitor. The very low coupling impedance of the device and the possibility of a calibration by simply wire measurements make the device hopefully usable in the accelerators machines.

Bibliography

[1] L. Palumbo, et al., *"Wake Field and Impedance"*, CERN 95-06, Vol. I, Geneve 1995.

[2] *"Computer Codes for Particle Accelerator Design and Analysis: a Compendium"*, LA-UR-90-1776, 1990.

[3] V.G. Vaccaro, CERN ISR-RF/66-35, 1966.

[4] W. K. H. Panofsky and W. A. Wenzel, *"Transverse Deflection of Charged particles in Radio Frequency Fields"*, Rev. Sci. Instr., Vol 27, 1956.

[5] A. W. Chao, *"Physics of Collective Beam Instabilities in High Energy Accelerators"*, John Wiley & Sons, 1993.

[6] A. W. Chao, *"Coherent instabilities of a relativistic bunched beam"*, SLAC PUB-2946, 1982.

[7] T. Weiland, *"On the Computation of Resonant Modes in Cylindrical Symmetric Cavities"*, Nucl. Instr. and Meth. in Phys Res.,Vol. 216, pp. 329-349, 1983.

[8] T. Weiland and R. Wanzemberg, *"Wake Fields and Impedances"*, DESY M-91-06, 1991.

[9] T. Weiland, *"Transverse Beam Cavity Interaction"*, Nucl. Instr. and Meth. in Phys. Res., Vol. 212, p. 13, 1983.

[10] A. Hofmann and B. Zotter, *"Improved Impedance Models for High Energy Accelerators and Storage rings"*, CERN-LEP/TH-88-51, 1988.

[11] S. Heifets, *"Broad Band Impedance of B-Factory"*, SLAC AP-93, 1992.

[12] K. Bane, *"The Calculated Longitudinal Impedance of the SLC Damping Ring"*, SLAC PUB-4618, 1988.

[13] K. Bane, *"Bunch Lengthening in the SLC Damping Rings"*, SLAC PUB-5177, 1990.

[14] M. Migliorati, et al., *"Bunch Lengthening in DAΦNE Main Ring"*, DAΦNE Technical Note G-22, LNF Frascati 1993.

[15] P. B. Wilson, *"High-Energy Electron Linacs: applications to storage ring RF Systems and Linear Collider"*, SLAC PUB-2884, 1982.

[16] J. D. Jackson, *"Classical Electrodynamics"*, Wiley NY, 1975.

[17] M. Migliorati, *"Progetto DAΦNE (Double Annular Ring for Φ Nice Experiment) - INFN Frascati: Studio e Simulazione della Dinamica Longitudinale dei Fasci di Particelle"*, Tesi di Laurea A.A. 1990-91, University of Rome "La Sapienza", 1991.

[18] M. Sands, *"The Physics of electron Storage Rings. An Introduction"*, SLAC-121, UC-28 (ACC), 1919.

[19] H. Goldstein, *"Classical Mechanics"*, Addison-Wesley, 1973.

[20] J. Le Duff, *"Longitudinal Beam Dynamics in Circular Accelerators"*, CERN 94-01, Vol. I, Geneve 1994.

[21] C. Bernardini and B. Touschek, *"On the Quantum Losses in an Electron Synchrotron"*, LNF Internal Note n. 34, LNF Frascati 1960.

[22] M. Migliorati, *"Effetti Collettivi nella Dinamica dei Fasci in una Macchina Acceleratrice Circolare con Applicazioni al Progetto DAΦNE"*, PhD Thesis, Roma, University of Rome "La Sapienza",1996.

[23] R. H. Helm, et al., *"Evaluation of Synchrotron Radiation Integrals"*, IEEE Trans. on Nucl. Sci. NS-20, p. 900, 1973.

[24] J. Haissinski, *"Exact Longitudinal Equilibrium Distribution of Stored Electrons in the Presence of Self-Fields"*, Il Nuovo Cimento, Vol. 18 B, N 1, p. 72, 1973.

[25] S. Petracca, *"Efficient Analytical and Numerical Solutions of Haissinki Equation"*, Particle Accelerators, Vol. 42, 1, p. 45, 1993.

[26] F. Sacherer, *"Methods for Computing Bunched-Beam Instabilities"*, CERN/SI-BR/72-5, 1972; F. Sacherer, *"A Longitudinal Stability Criterion for Bunched Beams"*, IEEE Trans. on Nucl. Sci. NS-20, 825, 1973; F. Sacherer, *"Bunch Lengthening and Microwave Instability "*, (Part 1, Part 2) CERN/PS/BR/77-5, 77-6, 1977.

[27] For example: A. Chao, op. cit.; B. Zotter, *"Longitudinal Stability of Bunched Beams"*, (Part 1, Part 2, Part 3), CERN-SPS/81-18, 81-19, 81-20, (DI), 1981; J. L. Laclare, *"Bunched Beam Coherent Instabilities"*, CERN 87-03, Vol I, p. 264, Geneve 1987.

[28] J. M. Wang and C. Pellegrini, *"On the Condition for a Single Bunch High Frequency Fast Blow-up"*, Proc. of the High Energy Accelerator Conference, CERN, 1990.

[29] K. Oide, *"A Mechanism of Longitudinal Single Bunch Instability in Storage Rings"*, Particle Accelerators, Vol. 51, pp. 43-52, 1995.

[30] M Zobov, et al., *"Bunch Lengthening and Microwave Instability in the DAΦNE Positron ring"*, DAΦNE Technical Note BM-3, LNF Frascati 1998.

[31] A. Chao, et al., *"A Weak Microwave Instability with Potential Well Distortion and Radial Mode Coupling"*, Proc of the 1995 Particle Acc. Conf., Dallas 1995.

[32] D. Boussard, *"Observation of Microwave Longitudinal Instabilities in the CPS"*, CERN-LABII/RF/INT/75-2, 1975.

[33] M Migliorati, et al., *"Bunch Lengthening in DAΦNE main ring"*, DAΦNE Technical Note G-22, LNF Frascati 1993.

[34] K. L. F. Bane and K. Oide, *"Simulations of the Longitudinal Instability in the SLC Damping Rings"*, Proc of the 1993 Particle Acc. Conf., Washington, pp. 3339-3341, 1993.

[35] R. Siemann, *"Computer Simulation of Bunch Lengthening in SPEAR"*, Nucl. Instr. and Meth. in Phys. Res., Vol. 203, p. 57, 1982.

[36] T. Weiland, *"On the Qualitative Prediction of Bunch Lengthening in High Energy Electron Storage Rings"*, DESY 81-088, 1981.

[37] M. Zobov, et al., *"Collective Effects and Impedance Study for the DAΦNE-Φ Factory"*, LNF 95/041, 1995.

[38] I. S. Gradshteyn and I. M. Ryshik, *"Table of Integrals, Series, and Products"*, Accademic Press Inc., 1990.

[39] A. Hofmann, *"Beam Instabilities"*, CERN 95-06, Vol. I, Geneve 1995.

[40] D. Boussard, *"Beam Loading"*, CERN 95-06, Vol. I, Geneve, 1995.

[41] M. Bassetti, et al., *"A time Domain Simulation Code of the Longitudinal Multibunch Instabilities"*, DAΦNE Technical note G-19, LNF Frascati 1993.

[42] M. Bassetti, *"Finite Difference Equations Calculations of Beam-Cavity Coupling Instability"*, LNF Internal Note 67/45, LNF Frascati 1967.

[43] S. Bartalucci, et al., *"Analysis of Methods for Controlling Multibunch Instabilities in DAΦNE"*, Particle Accelerator, Vol. 48, p. 213, 1995.

[44] M. Bassetti, et al., *"DAΦNE Longitudinal Feedback"*, Proc. Of the 1992 European Particle Acc. Conf., Berlin 1992.

[45] For example: *"An Asymmetric B-Factory"*, LBL PUB-5303, 1991.

[46] F. Marcellini, *"Progetto DAΦNE: Caratteristiche Teoriche e Sperimentali della Cavità Acceleratrice e Sviluppo di un Sistema di Soppressione dei Modi Superiori"*, Tesi di Laurea A.A. 1991-92, University of Rome "La Sapienza", 1992.

[47] P. Marchand, *"Damping of the Parasitic Modes in the 500 MHz RF Cavities for the Storage Ring of the B-Meson Factory Proposed at PSI"*, PSI TM-12-89-06, 1989.

[48] P. Arcioni and G. Conciauro, *"Feasibility of HOM-Free Accelerating Resonators: Basic Ideas and Impedance Calculations"*, Particle Accelerators, Vol. 36, p. 177, 1991.

[49] S. De Santis, *"Progetto DAΦNE: Sviluppo di un Sistema di Soppressione dei Modi di Ordine Superiore della Cavità a Radiofrequenza Mediante Accoppiamento con Guide d'Onda Adattate"*, Tesi di Laurea A.A. 1992-93, University of Rome "La Sapienza", 1993.

[50] R. Boni, et al., *"Kirchoff's Approximation for Evaluating the Coupling of DAΦNE RF Cavity with Waveguide Dampers"*, DAΦNE Technical note RF-15, LNF Frascati 1994.

[51] D. Alesini, et al., *"DAΦNE injection kicker: electromagnetic analysis of trapped modes and damping antenna design"*, Proc. of International Workshop on Performance Improvement of Electron-Positron Collider Particle Factories: e+e- Factories '99, KEK Tsukuba (Japan), 1999.

[52] A. Ghigo, D. Alesini, et al., *"Hom damping in the DAΦNE injection kickers"*, EPAC, Vienna 2000.

[53] D. Alesini, *"Studio Teorico e Sperimentale di un'antenna per l'Assorbimento dei Modi in una Struttura Risonante con Applicazione al Kicker si Iniezione*

dell'Acceleratore DAΦNE", Tesi di Laurea A:A 1997-98, University of Rome "La Sapienza", 1999.

[54] H. G. Hereward, *"The Elementary Theory of Landau Damping"*, CERN PS 65-20, 1965.

[55] M Migliorati, et al., *"Landau Damping of Longitudinal Multi-Bunch Instabilities in DAΦNE"*, DAΦNE Technical Note G-21, LNF Frascati 1993.

[56] M Migliorati, et al., *"Bunch Length Control in DAΦNE by a Higher Harmonic Cavity"*, Nucl. Instr. and Meth. in Phys. Res., Vol. 354, pp. 215-223, 1995.

[57] A. Wrulich, *"Single Beam Lifetime"*, CERN 94-01, Vol. I, Geneve 1994.

[58] W. Scandale, *"Dynamic Aperture"*, CERN 95-06, Vol. I, Geneve 1995.

[59] S. Guiducci, *"Beam Lifetime in DAΦNE"*, DAΦNE Technical Note L-12, LNF Frascati 1993

[60] C. Bernardini, B. Touschek, et al., *"Lifetime and Beam Size in Storage Ring"*, Phys. Rev. Lett., Vol. 10, 1963.

[61] H. Bruck, *"Accélérateurs Circulaires de Particles"*, Presses Universitaires de France, Paris 1966.

[62] G. Dôme, *"RF Theory"*, CERN 92-03, Vol. I, Geneve 1992.

[63] S. Ramo, et al., *"Field and Waves in Communication Electronics"*, John Wiley & Sons, 1965.

[64] T. Wangler, *"RF Linear Accelerators"*, John Wiley & Sons, NY, 1998.

[65] R.E. Collin, *"Foundation for Microwave Engineering"*, McGraw Hill, 1992.

[66] M. Lapostolle and A. L. Septier, *"Linear Accelerators"*, North-Holland Publishing Company, Amsterdam, 1970.

[67] The MAFIA collaboration, *"User's Guide MAFIA Version 4"*, CST GmbH, Lauteschlagerstr. 38, D-64289, Darmstad; www.cst.de.

[68] T. Weiland, AEÜ Int. Journ. of Electronic and Communications, Vol. 31, p. 116, 1977.

[69] T. Weiland, AEÜ Int. Journ. of Electronic and Communications, Vol. 31, p. 308, 1977.

[70] T. Weiland, Particle Accelerators, Vol. 15, p. 245, 1984.

[71] T. Weiland, Particle Accelerators, Vol. 17, p. 277, 1985.

[72] www.ansoft.com.

[73] Y. Garault, *"Etude d´une classe d´ondes électromagnétiques guidées : les ondes EH; application aux structures déflectrices pour les séparateurs à onde progressive de particules relativists"*, CERN 64-43, 1964.

[74] A. Falten, et al., Proc. 8th International Conference on High Energy Accelerators, p 338, 1971.

[75] M. Sands and J. Rees, *"A Bench Measurement of the Energy Loss of a Stored Beam to a Cavity"*, SLAC report PEP-95, 1974.

[76] H. Hahn and F. Pedersen, *"On Coaxial Wire Measurements of the Longitudinal Coupling Impedance"*, BNL 50870, Particle Accelerators and High Voltage MachinesTID-4500, 1978.

[77] M. G. Billing, et al., Proc. of the 1979 Particle Acc. Conf., p. 3583, 1979.

[78] A. Argan, et. al., *"On the Sands and Rees Measurement Method of Longitudinal Coupling Impedance"*, Proc. of the 1999 Particle Acc. Conf, New York, 1999.

[79] A. Argan, *"L'impedenza Longitudinale negli Acceleratori di Particelle"*, Tesi di Laurea, A. A. 1996-97, University of Naple "Federico II", 1997.

[80] F. Caspers, *"Beam Impedance Measurement Using the Coaxial Wire Method"*, CERN PS/88-59,1988.

[81] F. Marcellini, D. Alesini, et al., *"Beam coupling impendance measurements of the DAΦNE vacuum chamber components"*, Proc. of International Workshop on Performance Improvement of Electron-Positron Collider Particle Factories: e+e- Factories '99, KEK Tsukuba (Japan), 1999.

[82] L. S. Walling et al., *"Transmission-line impedance measurements for an advanced hadron facility"*, Nucl. Instr. and Meth. in Phys. Res. A, Vol. 281, p. 433, 1989.

[83] L. C. Maier, J. C. Slater, J. App. Phys., Vol. 23, No. 1, p. 68, 1952.

[84] E. L. Ginzton, *"Microwave Measuremnts"*, McGraw-Hill, Ch. 10, 1957.

[85] L. H. Chang, et al. *"Effects of the Landau Cavity on the Electron Beam"*, PAC, 1997.

[86] M. Boscolo, et al., *"Simulations and Measurements of the Touschek Background at DAΦNE"*, EPAC, Paris 2002.

[87] M. Zobov, D. Alesini et al., *"Luminosity performace at DAΦNE"*, Proc. Of the 2002 European Part. Acc. Conf., Paris, 2002.

[88] A. Gallo, D. Alesini, et al., *"Design status of a high harmonic RF system for DAΦNE"*, Proc. Of the 2000 European Part. Acc. Conf., Vienna, 2000.

[89] A. Ghigo, D. Alesini, et al.,*"DAΦNE Broadband Impedance"*, Proc. Of the 2002 European Part. Acc. Conf., Paris, 2002.

[90] J. Le Duff, *"High Luminosity"*, CERN 95-06, Vol. I, Geneve 1995.

[91] M. A. Furman, "Hourglass Effects for Asymmetric Colliders", PAC, p. 422. San Francisco 1991.

[92] A. Gallo, *"A RF Feedback for DAΦNE"*, DAΦNE Technical Note RF-6, LNF Frascati 1992.

[93] A. Poncet, *"Ion Trapping and Clearing"*, CERN 95-06, Vol. II, Geneve 1995.

[94] J. M. Byrd, et al., *"Transient beam loading effects in harmonic RF system for ligth sources"*, Phys. Rev. Spec. Top., Vol. 5, 2002.

[95] A. Gallo private communications.

[96] S. Guiducci, *"Beam Lifetime Studies in DAΦNE"*, Proc. Of the 2002 European Part. Acc. Conf., Paris 2002.

[97] A. Gallo, D. Alesini et al., *"The DAΦNE 3rd Harminic Cavity"*, Proc. Of the 2001 Part. Acc. Conf., Chicago, 2001.

[98] T. Tajima, *"Development of High-Order-Mode (HOM) absorbers for KEKB superconducting cavities"*, KEK Report 2000-10, 2000.

[99] W. Hartung, et al., *"Measurement of the Microwave Propertirs of Some Absorbing Materials"*, Proc. Of the Workshop on Microwave-Absorbing Materials for Accelerators, Virginia 1993.

[100] M. Zobov private communications.

[101] J. Delahaye, et al., *"CLIC, a 0.5 to 5 TeV e+/e- Compact Linear Collider"*,.EPAC, Stockholm 1998.

[102] H. Braun, et al., *"The CLIC RF Power Source: a Novel Scheme of Two-Beam Acceleration for Electron-Positron Linear Colliders "*, CERN 99-06, Geneve 1999.

[103] H. Braun, *"A new Mwthod of RF Power Generation for Two-Beam Linear Colliders"*, CERN/PS/98-14 (LP), Geneve 1998.

[104] *"CTF3 Design Report"*, CERN PS 2002-008 (RF), Geneve 2002.

[105] C. Milardi, D. Alesini, et al., *"CTF3 Compression System"*, EPAC, Paris 2002.

[106] D. Alesini, et al., *"The RF Deflectors for CTF3"*, CTFF3 Technical Note, INFN-LNF Accelerator Division, LNF Frascati 2001.

[107] D. Alesini, *"The theory of beam loading in RF deflectors for CTF3"*, CTFF3 Technical Note, INFN-LNF, LNF Frascati 2002.

[108] P. Bernard, et al., *"On the design of disc-loaded waveguides for RF separators"*, CERN 68-30, 1968.

[109] P. Bernard, et al., *"New disk-loaded waveguides for the CERN RF separator"*, CERN 70-26, 1970.

[110] J. Rossbach and P. Schmüser, *"Basic Course on Accelerator Optics"*, CERN 94-01, Vol. I, Geneve 1994.

[111] J. Buon, *"Beam Phase Space and Emittance"*, CERN 94-01, Vol. I, Geneve, 1994.

[112] D. Alesini, et al.,*"RF Beam Deflectors for CTF3 Combiner Ring"*, Proc. Of the 2002 European Part. Acc. Conf., Paris, 2002.

[113] M. Di Giosa, *"Studio di un Dispositivo per la Misura della Lunghezza dei Pacchetti di Particelle Ultra-Corti negli Acceleratori di Particelle"*, Tesi di Laurea A.A. 1999-2000, University of Rome "La Sapienza", 2000.

[114] C. Martinez, *"Determination of Longitudinal Electron Bunch Lenghts on Picosecond Time Scales"*, PhD Thesis, Univeritat Politècnica De Catalunya, 1999.

[115] J. C. Swartz, et al., *"Nondestructive diagnostics for relativistic picosecond bunched electron beams"*, Phys. Rev. E, vol. 52 n. 5, pp 5416-5424, 1995.

[116] B. Gagliardo, *"Studio Sperimentale di un Dispositivo per la Misura della Lunghezza dei Pacchetti negli Acceleratori di Particelle"*, Tesi di Laurea A.A. 2000-2001, University of Rome "La Sapienza", 2001.

[117] L. Palumbo, D. Alesini et al., *"Conceptual Study of an Ultra-Short Bunch Length Monitor"*, Proc. Of the 2001 Part. Acc. Conf., Chicago 2001.

[118] D. Alesini, et al., *"Electromagnetic simulations and RF Mesurements Results of an ultra-short Bunch length monitor"*, Proc. Of the 2002 European Part. Acc. Conf., Paris 2002.

[119] H. A. Bethe, *"Theory of diffraction by small holes"*, Phys. Rev., vol. 66, 1944.

[120] R. E. Collin, *"Field Theory of Guided Waves"*, IEEE Press, New York, 1991.

[121] S. De Sanctis, et al., *"Coupling Impedance of a Hole in a Coaxial Beam Pipe"*, Phys. Rev. E., vol. 54, pp. 800-805, 1996.

[122] C. D'Alessio, *"Studio Teorico e Sperimentale di un Dispositivo Elettromagnetico per la Misura della Posizione dei Pacchetti di Particelle negli Acceleratori"*, Tesi di Laurea A.A. 2000-2001, University of Rome "La Sapienza".

[123] G. Geschonke (ed.), et al., "CTF3 Design Report-Preliminary phase", CERN/PS 2001-072, 2001.

Acknowledgements

First of all, I would like to express my deepest gratitude to the prof. L. Palumbo who gave me the opportunity to work on the accelerators research. He is for me a constant and fundamental guide. Thank you.
I would like also to thank A. Gallo and F. Marcellini. They have helped and guided me from my first steps in the accelerator research. I have worked with them and I have always esteemed their broad knowledge in physics and their friendship.
Also M. Migliorati deserves a special thank for his teachings and his fundamental support.
I would like to express my deepest gratitude to the researchers of the Accelerator Division of the LNF-INFN, where I have worked during these years: to R. Boni responsible of the RF Group, to A. Ghigo responsible of the CTF3 collaboration, to G. Vignola, S. Bertolucci (now director of the LNF) and P. Raimondi responsible of the Accelerator Division, to M. Zobov for his useful suggestions and his support and to B. Spataro for his help and attention to my future. Thank you.
I would like to thank also A. Mostacci that supported me especially in the last part of the work and B. Gagliardo and C. D'Alessio (ex)students of the University of Rome "La Sapienza".